

NANO-SCALE PHASE SEPARATION AND GLASS FORMING ABILITY OF
IRON-BORON BASED METALLIC GLASSES

A THESIS SUBMITTED TO
THE GRADUATE SCHOOL OF NATURAL AND APPLIED SCIENCES
OF
MIDDLE EAST TECHNICAL UNIVERSITY

BY

MURATAHAN AYKOL

IN PARTIAL FULFILLMENT OF THE REQUIREMENTS
FOR
THE DEGREE OF MASTER OF SCIENCE
IN
METALLURGICAL AND MATERIALS ENGINEERING

SEPTEMBER 2008

Approval of the thesis:

**NANO-SCALE PHASE SEPARATION AND GLASS FORMING ABILITY
OF IRON-BORON BASED METALLIC GLASSES**

submitted by **MURATAHAN AYKOL** in partial fulfillment of the requirements
for the degree of **Master of Science in Metallurgical and Materials Engineering**
Department, Middle East Technical University by,

Prof. Dr. Canan Özgen _____
Dean, Graduate School of **Natural and Applied Sciences**

Prof. Dr. Tayfur Öztürk _____
Head of Department, **Metallurgical and Materials Engineering**

Prof. Dr. M. Vedat Akdeniz _____
Supervisor, **Metallurgical and Materials Engineering Dept., METU**

Prof. Dr. Amdulla O. Mekhrabov _____
Co-Supervisor, **Metallurgical and Materials Engineering Dept., METU**

Examining Committee Members:

Prof. Dr. Tayfur Öztürk _____
Metallurgical and Materials Engineering Dept., METU

Prof. Dr. M. Vedat Akdeniz _____
Metallurgical and Materials Engineering Dept., METU

Prof. Dr. Amdulla O. Mekhrabov _____
Metallurgical and Materials Engineering Dept., METU

Prof. Dr. C. Hakan Gür _____
Metallurgical and Materials Engineering Dept., METU

Erk İnger _____
General Manager, BOREN

Date: 04.08.2008

I hereby declare that all information in this document has been obtained and presented in accordance with the academic rules and ethical conduct. I also declare that, as required by these rules and conduct, I have fully cited and referenced all material and results that are not original to this work.

Name, Last name : Muratahan Aykol

Signature :

ABSTRACT

NANO-SCALE PHASE SEPARATION AND GLASS FORMING ABILITY OF IRON-BORON BASED METALLIC GLASSES

Aykol, Muratahan

M.Sc., Department of Metallurgical and Materials Engineering

Supervisor : Prof. Dr. M. Vedat Akdeniz

Co-Supervisor: Prof. Dr. Amdulla O. Mekhrabov

September 2008, 164 pages

This study is pertinent to setting a connection between glass forming ability (GFA) and topology of Fe-B based metallic glasses by combining intimate investigations on spatial atomic arrangements conducted via solid computer simulations with experimentations on high GFA bulk metallic glasses. In order to construct a theoretical framework, the nano-scale phase separation encountered in metallic glasses is investigated for amorphous Fe₈₀B₂₀ and Fe₈₃B₁₇ alloys via Monte Carlo equilibration and reverse Monte Carlo simulation. The phenomenon is identified regarding three topological aspects: 1) Pure Fe-clusters as large as ~0.9 nm and Fe-contours with ~0.72 nm thickness, 2) Fe-rich highly deformed body centered cubic regions, 3) B-centered prismatic units with polytetrahedral order forming distinct regions of high and low coordinations are found. All topological aspects are compiled into a new model called Two-Dimensional Projection Model for predicting contributions to short and medium range order (MRO) and corresponding spacing relations. The outcome geometrically involves proportions approximating golden ratio. After successfully producing soft magnetic Fe-Co-Nb-B-Si based bulk metallic glass and bulk nanocrystalline alloys with a totally conventional route, influences of alloying elements on structural units and crystallization modes are

identified by the developed model and radial distributions. While Co atoms substitute for Fe atoms, Nb and Si atoms deform trigonal prismatic units to provide local compactions at the outset of MRO. Cu atoms alter the type of MRO which resembles crystalline counterparts and accompanying nanocrystals that precipitate. The GFA can be described by a new parameter quantifying the MRO compaction, cited as Φ .

Keywords: Metallic Glasses, Phase Separation, Monte Carlo Simulations, Glass Forming Ability, Nanocrystallization

ÖZ

DEMİR-BOR TABANLI METALİK CAMLARDA NANO-ÖLÇEKLİ FAZ AYRIŞMASI VE CAM OLUŞTURMA YETENEĞİ

Aykol, Muratahan

Y. Lisans, Metalurji ve Malzeme Mühendisliği Bölümü

Tez Yöneticisi : Prof. Dr. M. Vedat Akdeniz

Ortak Tez Yöneticisi: Prof. Dr. Amdulla O. Mekhrabov

Eylül 2008, 164 sayfa

Bu çalışma, bilgisayar destekli simülasyon çalışmaları ile incelenen uzaysal atomik düzenlenmeleri ve yüksek cam oluşturma yeteneği (COY) sahibi iri hacimli metalik camlar üzerine yapılan deneyleri bir araya getirerek, Fe-B tabanlı metalik camlarda COY ve topoloji arasında bir bağlantı kurmayı amaçlamaktadır. Teorik bir altyapı oluşturmak için, metalik camlarda karşılaşılan nano-düzeyde faz ayrışması, $Fe_{80}B_{20}$ ve $Fe_{83}B_{17}$ amorf alaşımlarında, Monte Carlo benzetimi ve tersine Monte Carlo yöntemi ile incelenmiştir. Bahsedilen olgu üç topolojik gözlem ile açıklanmıştır: 1) ~ 0.9 nm boyutlarına varabilen saf Fe kümelerin ve ~ 0.72 nm kalınlığında Fe kontürlerin, 2) Ağırlıklı olarak Fe içeren oldukça deforme olmuş hacim merkezli kübik yapıda bölgelerin, 3) Az ve çok koordinasyonlu olarak ayrılmış, politetrahedral düzen sahibi B-merkezli prizmatik birim bölgelerinin varlığı bulunmuştur. Bütün yapısal bulgular değerlendirilerek İki-Boyutlu İzdüşüm Modeli olarak adlandırılan, kısa ve orta mesafeli düzenlenmeleri (OMD) ve ilgili mesafe ilişkilerini öngören yeni bir model geliştirilmiştir. Model geometriksel bağlamda altın oran sabitine yaklaşan oranlar ihtiva etmektedir. Fe-Co-Nb-B-Si tabanlı iri hacimli metalik cam ve nanokristal alaşımların konvansiyonel yöntemlerle başarıyla üretilmesinin ardından, alaşım elementlerinin yapısal birimlere ve kristalizasyon

modlarına olası etkileri mevcut model ve radyal dađılımlar vasıtasıyla tartıřılmıştır. Co atomları Fe atomları ile benzer davranırken, Nb ve Si atomları trigonal prizmatik birimleri deforme ederek, OMD'nin bařlangıç bölgesinde lokal bir sıkıřtırma etkisi gstermektedirler. Cu atomları kristal eřlenikleri andıran OMD tipini ve iliřkili nanokristal kelteleri deđiřtirmektedir. OMD sıkıřmaları ile COY'da yařanan artıř, Φ olarak adlandırılan yeni bir parametre ile nitelendirilebilmektedir.

Anahtar Szckler: Metalik Camlar, Faz Ayrıřması, Monte Carlo Benzetimi, Cam Oluřturma Ynelimi, Nanokristalizasyon

*To my beloved parents;
Fethiye and Hüseyin Ulvi Aykol*

ACKNOWLEDGEMENTS

I would like to express my gratitude to my supervisors Prof. Dr. M. Vedat Akdeniz and Prof. Dr. Amdulla O. Mekhrabov for their supervision, guidance, support and encouragement during this study. They trusted in me, gave me the chance of doing independent research and helped me get over every obstacle on the way.

I must thank all of my labmates; Cem Topbaşı for his encouraging discussions, endless motivation and clever hints, Mehmet Yıldırım for never hesitating to express his experiences and always being so benevolent in difficult times, Nagehan Duman for her kind suggestions and being supportive all the time, Ozan Özkan for always being more than a friend, a cousin or a colleague and always being so supportive, Sıla Süer for her sympathy and kindness, Sultan Aybar, for always being ready to pass her years of experience.

I would like to thank Nihat Ali Işıtman, for always guiding me with his deep and never ending knowledge through fruitful discussions, like those in undergraduate years. I am definitely indebted to Serhat Ün for his dedicated friendship and stimulating support, which I will never forget. Especially, I would also like to thank my fiancé for her patience and taking good care of me.

This study was financially supported through The Scientific and Technological Research Council of Turkey; TÜBİTAK with the project BOREN-TÜBİTAK No.105M354 which I gratefully acknowledge.

TABLE OF CONTENTS

ABSTRACT	iv
ÖZ	vi
DEDICATION	viii
ACKNOWLEDGEMENTS	ix
TABLE OF CONTENTS	x
LIST OF TABLES	xiii
LIST OF FIGURES	xiv
LIST OF SYMBOLS AND ABBREVIATIONS	xxii
CHAPTER	
1. INTRODUCTION	1
2. THEORY OF METALLIC GLASSES	4
2.1. The “Glass Transition” Phenomenon	4
2.2. Thermodynamics and Kinetics of Glass Formation	4
2.3. Semi-empirical Criteria of Glass Forming Ability	12
2.4. Structural Models of Metallic Glasses	14
3. TOPOLOGY OF METALLIC GLASSES	16
3.1. Background	16
3.2. Simulation Methods	20
3.2.1. Isothermal-Isobaric Monte Carlo Simulation Method	20
3.2.2. Reverse Monte Carlo Method	21
3.2.3. Generation of Random Numbers	22
3.2.4. Removing the Surface Effect and Employing Cut-off Radius	22
3.2.5. Neighbor Lists	23

3.2.6.	Validating the Algorithms in One Component Systems	25
3.3.	Structural Correlation Tools	28
3.3.1.	Radial Distribution Function	28
3.3.2.	Bond Angle Distribution Function	29
3.3.3.	Bond Length-Angle Hypersurface Analysis.....	29
3.3.4.	Voronoi Analysis.....	30
3.3.5.	Short Range Order Parameters	30
3.3.6.	Cluster-Size Distribution Analysis	31
3.4.	Simulation Procedures.....	31
3.5.	Calculating an Interaction Field from Pseudopotential Theory	32
3.6.	Results and Discussion	33
3.6.1.	Comparison of Interaction Fields in Fe-B system.....	33
3.6.2.	Structural Refinement.....	39
3.6.3.	Voronoi Analysis.....	44
3.6.4.	Bond Angle and Length-Angle Hypersurface Analyses	45
3.6.5.	Pure Fe-Cluster Size Distribution.....	49
3.6.6.	Connection Mechanisms	51
3.6.7.	Icosahedron-bcc Deformations.....	51
3.6.8.	Ordering of B-centered TPs.....	53
3.6.9.	Cluster-wise Decompositions of RDFs	57
3.6.10.	Two-Dimensional Projection Model	59
3.6.11.	Pseudo-Eutectic Mixture and Nanoscale Phase Separation	63
3.6.12.	Pre-crystallization of Amorphous Fe-B.....	64
4.	PRODUCTION, DEVELOPMENT AND PROPERTIES OF IRON-BORON BASED BULK METALLIC GLASSES.....	66
4.1.	Introduction	66
4.2.	Background.....	67
4.2.1.	Glass Forming Ability of Current BMG Alloys.....	67
4.2.2.	Bulk Amorphous Soft Magnets	69
4.2.3.	Nanocrystalline Alloys from Amorphous Precursors.....	71

4.3.	Alloy Design.....	74
4.4.	Experimental Methods.....	75
4.4.1.	Preparation of the Alloys.....	77
4.4.2.	Characterization of the Alloys.....	81
4.5.	Results and Discussion.....	82
4.5.1.	Fe-Y-B System.....	82
4.5.2.	Fe-Nb-B-Si System.....	86
4.5.3.	Thermal Analysis.....	93
4.5.4.	Nanocrystallization from BMG Precursors.....	108
4.5.5.	Magnetic Measurements.....	112
5.	BULK METALLIC GLASS FORMING ABILITY FROM TWO DIMENSIONAL PROJECTION MODEL.....	122
5.1.	Introduction.....	122
5.2.	Method of Calculating RDF from X-Ray Diffraction.....	122
5.3.	Results and Discussion.....	125
5.3.1.	Origins of Bulk GFA.....	125
5.3.2.	Effect of Precipitation of Fe ₂₃ B ₆ -type Phase on RDF of BMG.....	128
5.3.3.	Effect of Cu on RDF of BMG.....	130
5.3.4.	Radial Investigation of Nanocrystallization of FeCo.....	130
5.3.5.	Investigations on Φ Values.....	131
6.	CONCLUSIONS.....	136
	REFERENCES.....	139
	APPENDICES	
	A. PHASE DIAGRAMS.....	149
	B. C++ SOURCE CODES.....	150
	C. EDS ANALYSES.....	163

LIST OF TABLES

Table 3.1 Parameters of truncated Morse-type potential [92].	35
Table 3.2 Partial coordination numbers of Fe-Fe, B-Fe (Fe around B), and Fe-B (B around Fe) pairs are listed respectively. The calculated interatomic spacings and order parameters are also listed. Standard deviations for calculated partial coordination numbers and interatomic spacings are ± 0.03 and ± 0.01 respectively for all pairs.	44
Table 4.1 Purity grades of alloying elements used for alloy preparation. All elements are supplied from Alfa Aesar.	77
Table 4.2 Transition temperatures and GFA parameters of BMG alloys produced, measured by DSC analysis at a rate of 40 K/min for $(\text{Fe}_{36}\text{Co}_{36}\text{B}_{19.2}\text{Si}_{4.8}\text{Nb}_4)_{100-x}\text{Cu}_x$ bulk glassy alloys. All parameters are in Kelvin except for T_{rg} which is unitless.	101
Table 4.3 Magnetic properties of $(\text{Fe}_{36}\text{Co}_{36}\text{B}_{19.2}\text{Si}_{4.8}\text{Nb}_4)_{100-x}\text{Cu}_x$ as-quenched bulk glassy alloys and annealed bulk nanocrystalline alloys measured at room temperature.	118
Table 5.1 The r_2/r_1 ratios (Φ values) of several metallic glasses reported. If Alloy 2 is present, it refers to the alloy with higher GFA and compositions of the alloys are given in the order of Alloy 1 and Alloy 2. If Φ ratio was not readily calculable from provisions of the authors of corresponding reference, it was reproduced from RDFs they provided.	134

LIST OF FIGURES

Figure 2.1 Variation of a state-variable, e.g. volume, with temperature during cooling of a liquid melt.....	7
Figure 2.2 Variation of entropy difference between liquid and crystalline phases with temperature.	7
Figure 2.3 A typical sketch of change in viscosity during cooling of a liquid, resulting in either crystallization or glass formation.	8
Figure 3.1 Pair correlation function for Al at 650 °C from the simulation of Smolander [68].	18
Figure 3.2 Reduced radial distribution functions of Ni-Ni and Ni-B pairs [30].	19
Figure 3.3 A 2-dimensional sketch of periodic boundary conditions with minimum image convention. The filled-circles represent atoms, the dotted-circle indicated by the shorter vector is cut-off sphere and dotted-circle indicated by the longer vector is the minimum image sphere of atom marked as “a”.....	24
Figure 3.4 The effects of different MC cooling rates on accompanying phase transitions are shown by variation of volume with temperature.	26
Figure 3.5 The structures attained at 100 K and corresponding radial distribution functions after applying different cooling rates.....	27
Figure 3.6 Left and right images are snapshots of simulation cells taken after equilibrium at 100 K after 0.1 and 0.025 K/MC-s cooling rates respectively. Left structure is amorphous whereas the right one is an FCC crystal.....	27
Figure 3.7 Calculated interatomic pair potentials versus distance in Fe-B system. .	35
Figure 3.8 Interaction field reported by Hausleitner and Hafner [52] for Fe-B binary system.	36

Figure 3.9 Morse-type interaction field for Fe-B binary system reported by Fujiwara et al. [92].....	37
Figure 3.10 Change of volume by MC-steps for all applied pair potentials. Plots are shifted arbitrarily for clarity.	38
Figure 3.11 RDFs of Fe-Fe pairs, reproduced by different types of pair potentials and compared to experimental Fe-Fe RDF of Nold et al [46]......	38
Figure 3.12 Reduced RDFs, $G(r)$'s, of $\text{Fe}_{80}\text{B}_{20}$, (a) being the Fe-B pairs and (b) the Fe-Fe pairs. Solid lines represent the reproduced experimental results of Nold et al. [46] mentioned as Neutron, dotted lines represent results of MC simulations and black dots represent results of RMC simulations. Insets show RMC fittings to corresponding experimental partial structure factors.	41
Figure 3.13 Voronoi diagrams of B centered polyhedra in (a) $\text{Fe}_{80}\text{B}_{20}$ and (b) $\text{Fe}_{83}\text{B}_{17}$. Full bars and thin crossed bars represent results of MC and RMC simulations respectively.	42
Figure 3.14 Voronoi diagrams of Fe centered polyhedra in (a) $\text{Fe}_{80}\text{B}_{20}$ and (b) $\text{Fe}_{83}\text{B}_{17}$. Full bars and thin crossed bars represent results of MC and RMC simulations respectively.	43
Figure 3.15 BAD functions for Fe-Fe-Fe (dashed line), Fe-B-Fe (dotted line) and B-B-B (solid line) triplets in $\text{Fe}_{80}\text{B}_{20}$. At the bottom, cp denotes central pentagonal, i; icosahedral, b; bcc and p; pentagonal angles.....	47
Figure 3.16 BLAH as a function of angle and distance are given. First row comprises of bulk Fe NN, intra-cluster Fe NN and Fe NN CZ BLAHs. Second row comprises of corresponding normalized surfaces. The surfaces are smoothed by a negative exponential function with sampling proportion of 0.01 and 50 intervals. .	48
Figure 3.17 (a) Number of purely Fe clusters N_c vs. cluster size, D . Total number of such Fe-clusters in $\text{Fe}_{83}\text{B}_{17}$ is twice of that in $\text{Fe}_{80}\text{B}_{20}$. (b) The Fe-contours are	

illustrated for $\text{Fe}_{83}\text{B}_{17}$ with depth cueing; depth increases with brightness. (c) Schematic form of the Fe-contour, perturbing Fe-cluster and B-rich domains.....	50
Figure 3.18 A 0.92 nm Fe-cluster (large atoms) of $\text{Fe}_{83}\text{B}_{17}$ with surrounding B atoms (small atoms) of TPs over triangular sites are shown in (a). Five-fold symmetry is marked with a solid circle. The Voronoi indices diffracted by atoms embedded in the cluster are noted. In (b) a typical triangular facet sharing (marked with <i>s</i>) of an Fe-cluster/contour with a TP is sketched. In (c), cross-section of a stellated Fe-contour directly from the simulation is given. Solid circle represents a 5-fold symmetrical plane and straight lines represent stellation directions. In (d) an atom deficient small-triambic icosahedron is sketched.....	54
Figure 3.19 Distorted structures arising due to simultaneously progressing incomplete Mackay and Bain transformations of icosahedral clusters. The frontal pentagon is formed by four atoms marked as <i>p</i> and the <i>A</i> atom, and <i>c</i> denotes the capping atom.	55
Figure 3.20 Bcc (111) plane extending through several atoms, formed in a $\langle 0,3,6,4 \rangle$ aggregate. Dark spheres and white spheres are Fe and B atoms respectively.....	55
Figure 3.21 Left image is a snapshot of simulation cell where all points indicate B-centered prisms, largest spheres connected with lines are prisms having more than 10 neighbor prisms, coordination decreases with decreasing sphere size (CN = 9 for intermediate white spheres and $\text{CN} \leq 8$ for small gray spheres). Central image shows several polytetrahedral aggregates of B-prisms. Right sketch denotes an ico-like pentagonal lining of NN B-prisms and their connection modes (only Fe-Fe bonds are drawn for clarity).....	56
Figure 3.22 Cluster-wise decomposition of (a) Fe-Fe and (b) Fe-B RDFs. In (a) intra-cluster means Fe atoms bounded to the same B atom and inter-cluster means non-NN Fe atoms of two neighboring B-prisms. In (b) Inter-cluster Fe' denotes vector originating from a B atom, pointing NN Fe atoms of CZ Fe atoms whereas Fe'' pointing non-NN Fe atoms of CZ Fe atoms. The separations predicted by 2D-projection model are scattered on total RDFs.	58

Figure 3.23 Nearly co-planar 5 Fe atoms and nearly co-planar 4 Fe atoms (spheres at corners) in a schematic B-centered (dark spheres) TP unit with three capping atoms ($\langle 0,3,6,0 \rangle$), forming a pentagonal ring and a square ring respectively are marked with dashed lines. Numbers of rings can vary depending on TP type. P-P, P [^] P, P-S and P [^] S modes are sketched. All spheres at the corners are Fe atoms. Spheres marked as “C” are Fe or B atoms above or below idealized planes.	61
Figure 3.24 An arbitrary sketch of near eutectic region of Fe-B binary phase diagram. The solid lines, dashed lines, α' , e_{mix} and “a” represent, equilibrium cooling, non-equilibrium cooling, primary α -Fe, eutectic mixture and amorphous phase respectively. The crossed and zigzagged regions represent room temperature structures resembling hypo-eutectic and eutectic regions after rapid solidification (metallic glass formation).....	62
Figure 3.25 Variation of BAD in crystalline bcc-Fe from 10 K to melting.	65
Figure 3.26 Variation of RDF in crystalline bcc-Fe from 10 K to melting.	65
Figure 4.1 Relationship among the critical cooling rate, R_c , for glass formation, maximum thickness and reduced glass transition temperature [96].....	68
Figure 4.2 Preparation route of the bulk amorphous alloys produced in NOVALAB.	76
Figure 4.3 The copper tray and chamber of the Arc-Melting device is cleaned and polished prior to every melting. Zirconium metal standing solely in a small reservoir next to the -to be prepared- alloy is melted in advance to justify the removal of any trace amount of oxygen.	80
Figure 4.4 The photographs of centrifugal cast (a) Fe-Y-B, (b) Fe-Nb-B-Si, (c) Fe-Co-Nb-B-Si, (d) Fe-Co-Nb-B-Si with 0.5at.% Cu , (e) Fe-Co-Nb-B-Si with 0.75at.% Cu and (f) Fe-Co-Nb-B-Si with 1.0 at.% Cu alloys.	84
Figure 4.5 X-ray diffraction pattern of $\text{Fe}_{72}\text{Y}_6\text{B}_{22}$ alloy after centrifugal casting. ...	85

Figure 4.6 SEM images of $\text{Fe}_{72}\text{Y}_6\text{B}_{22}$ alloy taken from (a) thin sections and (b) middle sections.	85
Figure 4.7 X-Ray diffractogrammes of centrifugal cast (a) partially amorphous $\text{Fe}_{72}\text{B}_{14.4}\text{Si}_{9.6}\text{Nb}_4$ and (b) bulk amorphous $\text{Fe}_{36}\text{Co}_{36}\text{B}_{19.2}\text{Si}_{4.8}\text{Nb}_4$ alloys	87
Figure 4.8 Secondary electron image (left) and back scattered electron image (right) of $\text{Fe}_{36}\text{Co}_{36}\text{B}_{19.2}\text{Si}_{4.8}\text{Nb}_4$ bulk amorphous alloy.....	90
Figure 4.9 Secondary electron image of fracture surface of $\text{Fe}_{36}\text{Co}_{36}\text{B}_{19.2}\text{Si}_{4.8}\text{Nb}_4$ bulk amorphous alloy.	90
Figure 4.10 Photographs show the shiny luster of the 3 mm thick regions of the wedge shaped bulk amorphous $\text{Fe}_{36}\text{Co}_{36}\text{B}_{19.2}\text{Si}_{4.8}\text{Nb}_4$ (upper image) and $(\text{Fe}_{36}\text{Co}_{36}\text{B}_{14.4}\text{Si}_{9.6}\text{Nb}_4)_{99.25}\text{Cu}_{0.75}$ (lower image) alloys.....	91
Figure 4.11 X-Ray diffractogrammes of centrifugal cast bulk metallic glass $(\text{Fe}_{36}\text{Co}_{36}\text{B}_{19.2}\text{Si}_{4.8}\text{Nb}_4)_{100-X}\text{Cu}_X$ alloys where X ranges between 0 and 1.	92
Figure 4.12 Sequential thermal analyses of $\text{Fe}_{36}\text{Co}_{36}\text{B}_{19.2}\text{Si}_{4.8}\text{Nb}_4$ bulk glassy alloy, in which 1 st path is plotted in red and 2 nd path in blue. Heating and cooling paths are marked with arrows pointing right and left respectively.....	96
Figure 4.13 Sequential thermal analyses of $(\text{Fe}_{36}\text{Co}_{36}\text{B}_{19.2}\text{Si}_{4.8}\text{Nb}_4)_{99.5}\text{Cu}_{0.5}$ bulk glassy alloy, in which 1 st path is plotted in red and 2 nd path in blue. Heating and cooling paths are marked with arrows pointing right and left respectively.....	97
Figure 4.14 Sequential thermal analyses of $(\text{Fe}_{36}\text{Co}_{36}\text{B}_{19.2}\text{Si}_{4.8}\text{Nb}_4)_{99.25}\text{Cu}_{0.75}$ bulk glassy alloy, in which 1 st path is plotted in red and 2 nd path in blue. Heating and cooling paths are marked with arrows pointing right and left respectively.....	98
Figure 4.15 Sequential thermal analyses of $(\text{Fe}_{36}\text{Co}_{36}\text{B}_{19.2}\text{Si}_{4.8}\text{Nb}_4)_{99}\text{Cu}_1$ bulk glassy alloy, in which 1 st path is plotted in red and 2 nd path in blue. Heating and cooling paths are marked with arrows pointing right and left respectively.....	99
Figure 4.16 Glass transition region and crystallization of $\text{Fe}_{36}\text{Co}_{36}\text{B}_{19.2}\text{Si}_{4.8}\text{Nb}_4$ bulk amorphous alloy. Heating rate is 40 K/min.....	101

Figure 4.17 Comparison of low temperature regions of 1 st heating paths of $(\text{Fe}_{36}\text{Co}_{36}\text{B}_{19.2}\text{Si}_{4.8}\text{Nb}_4)_{100-X}\text{Cu}_X$ bulk glassy alloys where X ranges between 0 and 1, showing the glass transition and crystallization regions.	104
Figure 4.18 Comparison of high temperature regions of 1 st heating paths of $(\text{Fe}_{36}\text{Co}_{36}\text{B}_{19.2}\text{Si}_{4.8}\text{Nb}_4)_{100-X}\text{Cu}_X$ bulk glassy alloys where X ranges between 0 and 1, showing the melting behaviors of as-crystallized alloys.	105
Figure 4.19 Comparison of 2 nd heating paths of $(\text{Fe}_{36}\text{Co}_{36}\text{B}_{19.2}\text{Si}_{4.8}\text{Nb}_4)_{100-X}\text{Cu}_X$ bulk glassy alloys where X ranges between 0 and 1, showing the melting behaviors following the 1 st solidification.	106
Figure 4.20 Comparison of 2 nd cooling paths of $(\text{Fe}_{36}\text{Co}_{36}\text{B}_{19.2}\text{Si}_{4.8}\text{Nb}_4)_{100-X}\text{Cu}_X$ bulk glassy alloys where X ranges between 0 and 1, showing the solidification behaviors following the 2 nd melting.	107
Figure 4.21 X-Ray diffractogrammes of as-quenched (as-q) and annealed $\text{Fe}_{36}\text{Co}_{36}\text{B}_{19.2}\text{Si}_{4.8}\text{Nb}_4$ alloys.	110
Figure 4.22 X-Ray diffractogrammes of $(\text{Fe}_{36}\text{Co}_{36}\text{B}_{19.2}\text{Si}_{4.8}\text{Nb}_4)_{100-X}\text{Cu}_X$ alloys annealed at 873 K for 300 s, where X ranges between 0 and 1. The XRD peaks are marked with the corresponding BCC plane indices.	111
Figure 4.23 Hysteresis loop of bulk glassy $\text{Fe}_{36}\text{Co}_{36}\text{B}_{19.2}\text{Si}_{4.8}\text{Nb}_4$ alloy. Inset shows the region around zero field strength.	113
Figure 4.24 Hysteresis loops of amorphous $\text{Fe}_{36}\text{Co}_{36}\text{B}_{19.2}\text{Si}_{4.8}\text{Nb}_4$ alloy at RT (room temperature, 423, 523, 773 and 873 K. Upper inset shows the region around zero field strength at 873 K. Lower inset shows the application of power law for estimation of T_c	114
Figure 4.25 Hysteresis loops of as-quenched $(\text{Fe}_{36}\text{Co}_{36}\text{B}_{19.2}\text{Si}_{4.8}\text{Nb}_4)_{100-X}\text{Cu}_X$ bulk glassy alloys.	116

Figure 4.26 Hysteresis loops of soft magnetic $(\text{Fe}_{36}\text{Co}_{36}\text{B}_{19.2}\text{Si}_{4.8}\text{Nb}_4)_{100-X}\text{Cu}_X$ bulk nanocrystalline alloys obtained by annealing the corresponding BMG alloys at 873.K for 300 s.	117
Figure 4.27 Variation of saturation induction (B_s) and coercivity (H_c) for as-cast; BMG and annealed; BNCA $(\text{Fe}_{36}\text{Co}_{36}\text{B}_{19.2}\text{Si}_{4.8}\text{Nb}_4)_{100-X}\text{Cu}_X$ alloys with Cu content.	119
Figure 4.28 Hysteresis loops of as-quenched $(\text{Fe}_{36}\text{Co}_{36}\text{B}_{19.2}\text{Si}_{4.8}\text{Nb}_4)_{100-X}\text{Cu}_X$ bulk glassy alloys obtained without annealing, showing unexpectedly excellent magnetic behaviors.....	120
Figure 5.1 Total experimental reduced scattering factor for amorphous Fe-Co-Nb-B-Si alloy.....	124
Figure 5.2 The Fourier-transformed $\sum_{uc} K_j 4\pi r^2 \rho_j(r)$ curve from which $g(r)$ can be extracted.....	125
Figure 5.3 Total experimental RDFs of amorphous $\text{Fe}_{80}\text{B}_{20}$ and $\text{Fe}_{36}\text{Co}_{36}\text{B}_{19.2}\text{Si}_{4.8}\text{Nb}_4$ alloys and their radial difference $\Delta g(r)$	128
Figure 5.4 Reduced RDFs, i.e. $G(r)$'s of as quenched and annealed $\text{Fe}_{36}\text{Co}_{36}\text{B}_{19.2}\text{Si}_{4.8}\text{Nb}_4$ base alloy.....	129
Figure 5.5 Reduced RDFs, i.e. $G(r)$'s of bulk amorphous alloys of $(\text{Fe}_{36}\text{Co}_{36}\text{B}_{19.2}\text{Si}_{4.8}\text{Nb}_4)_{100-X}\text{Cu}_X$, where X ranges between 0 and 1.....	132
Figure 5.6 Reduced RDFs, i.e. $G(r)$'s of bulk nanocrystalline alloys of $(\text{Fe}_{36}\text{Co}_{36}\text{B}_{19.2}\text{Si}_{4.8}\text{Nb}_4)_{100-X}\text{Cu}_X$, where X is 0.75 and 1.00, are compared to $G(r)$'s their corresponding bulk glassy precursors. The lowest graph is a sample BCC $G(r)$ adjusted to a lattice parameter that would yield a first separation distance equal to first peak of given RDFs.....	133
Figure 5.7 Φ versus pressure plots of (a) Pd-Ni and (b) Cu-Ag calculated after studies [137] and [138] respectively.....	135

Figure A. 1 Fe-B Binary phase diagram [139].....	149
Figure C. 1 Composition of dendritic phase in centrifugal cast Fe-Y-B alloy by EDS analysis.	163
Figure C. 2 Composition of inter-dendritic phase in centrifugal cast Fe-Y-B alloy by EDS analysis.....	164
Figure C. 3 Composition of amorphous phase in centrifugal cast Fe-Co-Nb-B-Si alloy by EDS analysis.....	164

LIST OF SYMBOLS AND ABBREVIATIONS

ΔG_{l-s}	Free energy difference between solid and liquid
ΔH_f	Enthalpy change of freezing
ΔS_f	Entropy change of freezing
C_p	Specific heat capacity at constant pressure
T	Temperature
P	Pressure
V	Volume
S	Entropy
T_g	Glass transition temperature
T_x	Temperature of onset of crystallization
$V(r)$	Interatomic interaction potential function
$g(r)$	Radial distribution function
$G(r)$	Reduced radial distribution function
B_s	Saturation induction
μ_e	Magnetic permeability
H_c	Coercivity
T_c	Curie temperature
ΔT_x	Supercooled liquid region
T_{rg}	Reduced glass transition temperature
T_l	Liquidus temperature
T_e	Temperature of eutectic reaction
T_m	Temperature of onset of melting
ΔH_x	Enthalpy of crystallization
Φ	r_2/r_1 ratio of RDF approaching golden ratio or golden ratio itself
GFA	Glass forming ability
BMG	Bulk metallic glass
BNCA	Bulk nanocrystalline alloy

BCC	Body centered cubic
FCC	Face centered cubic
BCT	Body centered tetragonal
D-BCC	Deformed body center cubic
ICO	Icosahedron or icosahedral
TM-M	Transition metal – metalloid
BAD	Bond angle distribution
BLAH	Bond length-angle hypersurface
TP	Trigonal prism or trigonal prismatic
SRO	Short range order
MRO	Medium range order
RDF	Radial or reduced radial distribution function
CN	Coordination number
CS	Coordination sphere
CZ	Connection zone
NN	Nearest neighbor

CHAPTER 1

INTRODUCTION

Many aspects of materials science dealt mostly with crystalline materials and achieved almost a complete understanding of such materials; especially of their physics and chemistry. The symmetrical nature of crystalline materials allowed infinitely many assumptions to be made and made calculations and predictions less challenging. The nature of amorphous materials, lacking a complete description even today, has become a more active field than ever before and appears to demand a more painstaking research due to the inadequacy of established physics and chemistry theories of crystals when applied to amorphicity. Although covalently bonded glasses are known since the ancient times, the glass formation phenomenon and a lack of long range order turned out to be unclear since the introduction of glasses comprising solely of metallic elements in 1960 by Klement et al. [1], having a dominating metallic bonding nature.

In materials production, rapid solidification can have different aims such as grain refinement, extending solid solubility limits, forming non-equilibrium crystalline phases and retaining the structure of melt in a supercooled state [2]. After the pioneering alloy of Klement et al., Au - 25 at.% Si exploiting accidentally that last aim, many methods such as splat cooling, melt spinning, ion implementation etc. are developed and improved to obtain metallic glasses. The most established and industrially applied technique has definitely been the melt spinning technique introduced by Pond and Maddin [3]. It is basically the pouring of the liquid melt on to a rolling wheel that dissipates heat fast, a copper or a steel wheel, and getting a thin sheet of material cooled rapidly. The ribbons produced typically have dimensions of 1-3 mm width and 20-60 μ m thickness. Cooling rates between 10^4

and 10^7 K/s can be achieved with this method [4]. When $\text{Fe}_{75}\text{P}_{15}\text{C}_{10}$ alloy was quenched into an amorphous structure, ferromagnetic at room temperature with saturation magnetization of 0.7 T, it was shown that these novel alloys can be produced from inexpensive materials contradicting the expensive alloys of Au, Pt and Pd [5]. This alloy also initiated a sudden rush into these formerly non-popular alloys due to the close-minded belief that ferromagnetism is peculiar to crystalline solids; long range ordered structures; although, previously Gubanov [6] showed that ferromagnetism is rather a short-range order dependent phenomenon and amorphous solids can also bear it. The close-minded belief actually originates from the fact that the glasses known up to that date were the oxide ones and lacked ferromagnetism. Later, many ferromagnetic glassy alloys were produced and some of them are commercialized like $\text{Fe}_{80}\text{B}_{20}$; namely, Metglas 2605. This alloy has become the mother alloy of ferromagnetic Fe-B based metallic glasses produced later such as Finemet, Nanoperm and Hitperm. Today, such metallic glasses are not confined to ribbons and they can be produced in bulk forms; i.e., as bulk metallic glasses (BMGs) and even as bulk nanocrystalline alloys (BNCAs) with the help of compositional tunings and annealings.

The theoretical part of the study aims at constructing a solid theoretical skeleton and providing a phenomenological combination with glass forming ability (GFA) of metallic glasses by specifically sampling the Fe-B based alloys. A complete map of nanoscale phase separated structure of TM-M metallic glasses is given in the theoretical part of the study by utilizing Monte Carlo and reverse Monte Carlo methods, involving several novel structural analysis tools and yielding a model called Two-Dimensional Projection Model which can estimate spatial arrangements of atoms.

In the experimental part of the study, Fe-Y-B and Fe-Nb-B-Si systems are investigated, and at least 3 mm thick, soft magnetic BMGs were achieved to be produced via a completely conventional route in the latter system, which are also

converted to BNCAs by compositional modifications and proper annealings. By sequential thermal analyses, X-ray diffractions and magnetic measurements, these developed alloys are completely characterized.

Lastly, the theoretical and experimental results are combined with the aid of the as-developed spatial model and calculated radial distributions to reveal the topological influences of alloying elements like Nb which promotes GFA, or like Cu, which alters the crystallization modes and provides precipitation of nanocrystals. In addition to investigating spatial atomic changes accompanying the nanocrystallization of BNCAs, the correlations of these primary crystallization products of BMGs and their medium range atomic order are made clear.

CHAPTER 2

THEORY OF METALLIC GLASSES

2.1. The “Glass Transition” Phenomenon

Glass used to be a term denoting the naturally existing or readily forming amorphous materials more commonly possessing silica and oxides of metals such as Al, Ca, Mg, K and Na having many applications in everyday use. Today, glass is a more general term that indicates a material that is solidified continuously from the melt and has gone through a phase transition named glass-transition. The term is not confined to silica based amorphous materials anymore. As indicated by Zallen, although “glass” and “amorphous solid” are synonyms and generally used to describe the same kind of material, conventionally to call a material a glass, it should exhibit a determinable glass transition temperature [7], otherwise it is named as an amorphous one. Consequently, description of glass forming ability requires a complete understanding of the so called “glass” transition in advance.

2.2. Thermodynamics and Kinetics of Glass Formation

There are a great many theories involving thermodynamics, kinetics, combination of both, structural models, empirical rules and etc., all trying to be descriptive in this case. The most fundamental theory is of course given via thermodynamics and it should be discussed before all the others. Obviously, thermodynamics deals with relative stabilities of phases and here, the relative stabilities of the supercooled melt and competing crystalline phases are of primary concern. The term “supercooled”

points the stability of the liquid phase below the melting temperature of the alloy. The free energy difference of liquid and solid phases given in Equation (2.1) should be small at a given temperature T below T_m for the liquid phase to be relatively more stable.

$$\Delta G_{l-s} = G_l - G_s \quad (2.1)$$

$$\Delta G_{l-s}(T) = \Delta H_f - \Delta S_f T - \int_T^{T_m} \Delta C_p^{l-s}(T) dT + T \int_T^{T_m} \frac{\Delta C_p^{l-s}(T)}{T} dT \quad (2.2)$$

From Equation (2.2), it can be depicted that ΔH_f should be smaller and ΔS_f should be larger for the liquid to be more stable. At first glance, a large ΔS_f signals the prominence of multicomponent alloys since entropy is related to the number of microscopic states.

Until now, the stability of the liquid phase relative to solid phase is discussed in a simplified manner. However, the considered phases are a liquid and a crystalline solid and the phase transition is melting, which is a first order one. No clue about a phase transition yielding a glassy phase is given. Glass transition phenomenon is not as clear as liquid-crystal or crystal-crystal phase transitions. A liquid to crystal phase transition is a first-order phase transition, possessing a discontinuity at the derivatives of Gibbs free energy with respect to state variables [8]; for example; $(\partial G / \partial T)_p = -S$ and $(\partial G / \partial P)_T = V$ as shown for the latter case in Figure 2.1. A second-order phase transition is continuous at these derivatives, S and V ; but discontinuous at the second derivatives like C_p . As shown in Figure 2.1 glass transition, behaving more like a second-order phase transition covers a range of temperature rather than occurring at a well defined temperature. Namely, T_g has actually a very small finite temperature range near itself. Due the supercooling of the liquid mentioned previously; some melts cooled rapid enough to bypass the first-order liquid to crystal phase transition can remain as an undercooled liquid. If

during this cooling period, no nucleation occurs, the undercooled melt can go under the second-order *like* transition, named glass transition and turn into a glassy solid state. The thermal expansion coefficient of glass is very close to that of a solid phase; attributed to crystals.

Whether glass transition is an equilibrium second-order transition or not is still under debate. There is some evidence regarding glass transition being an equilibrium transition shifted to higher temperatures due to kinetic effects. It is known that T_g is time dependent; it gets lower at relatively smaller cooling rates due to the presence of a longer relaxation times for liquid, but the degree of that is insignificant [7] to consider practically. The curiosity arises from the fact that the discontinuity of C_p at T_g is not perfect and occurs actually in a narrow range; which is first unveiled by Chen and Cohen [9] while discussing the existence of T_g for an amorphous metallic alloy. This is why glass transition is called a “second-order *like*” transition. The two best-known models reported dealing with glass transition are Turnbull-Cohen [10, 11] and Gibbs-DiMarzio [12] models. They both agree that glass transition features a subjacent equilibrium transition. As mentioned, T_g is time dependent and at sufficiently low cooling rates assuming no crystallization, it can be lowered. However, this undercooling cannot be proceeded down to $T = 0$ K, since at some finite temperature called “Kauzmann” temperature [13], the entropies of the liquid and crystal become equal as in Figure 2.2. A dilemma arises since an amorphous structure cannot have entropy equal to or lower than its crystal counterpart. As a result, a glass transition must occur at that temperature. This is of course only a semi-empirical approach since the existence of T_{Kauzmann} is proved only by extrapolating the $\Delta S = S_l - S_s$ to null. However, it is also the greatest evidence glass transition being a second-order equilibrium thermodynamic transition and the T_g values and accompanying transitions are kinetically modified ones. Consequently, although macroscopically understood, glass transition still remains as an unresolved thermodynamical phenomenon.

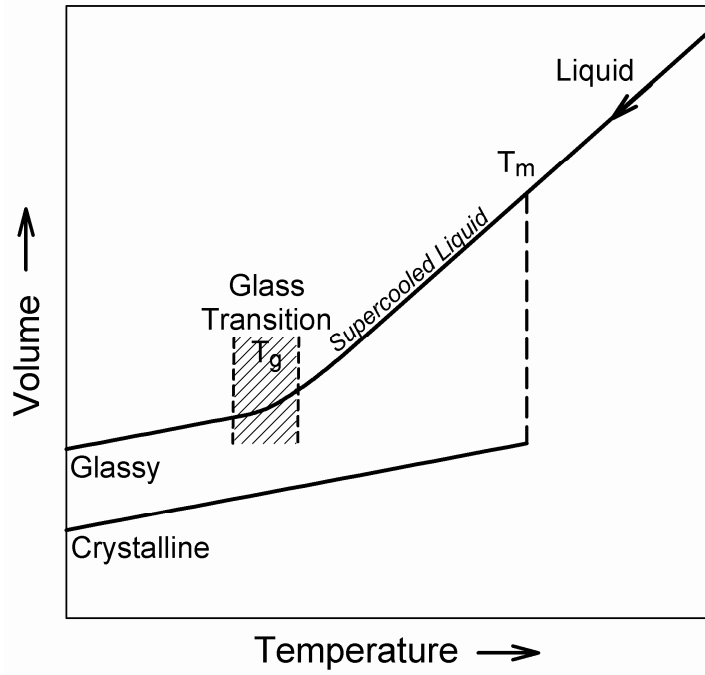


Figure 2.1 Variation of a state-variable, e.g. volume, with temperature during cooling of a liquid melt.

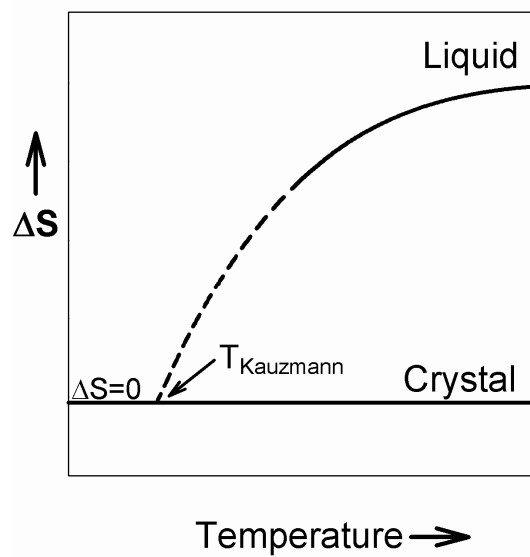


Figure 2.2 Variation of entropy difference between liquid and crystalline phases with temperature.

There have been indirect approaches based on thermodynamical facts mentioned to correlate glass-forming ability with alloys. Yan and co-workers [14] tried searching for low liquidus surfaces by compiling the thermodynamic data for binary and ternary systems to extract thermodynamic properties of multicomponent alloys. Their idea is based on the fact that low melting point compositions, like eutectic favor glass formation. Since a complete theory of glass formation is still lacking, thermodynamic approaches require such indirect predictions like searching for low liquidus surfaces. Another approach, for example, is that of Kim et al. [15], which initiates from again an indirect relation like retarding the nucleation process by searching for a local minimum of driving force of crystallization favors glass formation.

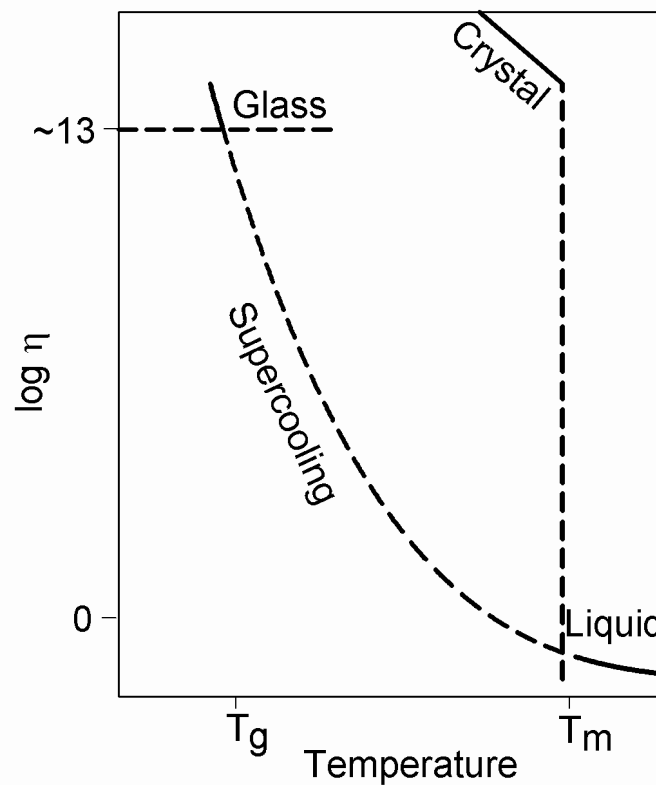


Figure 2.3 A typical sketch of change in viscosity during cooling of a liquid, resulting in either crystallization or glass formation.

The mobilities of atoms in a liquid are quite higher than in solids; as a result of which, altering any transformation originating from this liquid phase requires much severe cooling rate modifications than any solid-solid phase transformations. During the supercooling of a melt, shear viscosity (η), the degree of resistance to flow, increases continuously upon cooling of the melt as shown in Figure 2.3. During this increase in η , although the driving force for nucleation increases atomic mobility decreases. When η passes the conventionally determined 10^{13} poise, the melt is said to pass T_g and become frozen. As mentioned before, T_g is not a unique temperature and kinetic aspects of the thermal processes affect it to some extent.

Kinetics can be basically introduced accompanying the thermodynamics in case of nucleation phenomenon. In reference to clear description by Verhoeven [16], the required energy for the generation of new surfaces; to form stable nuclei in the melt can be related to the degree of undercooling of the alloy (or the supercooling). The free-energy barrier to be overcome to form stable spherical nuclei during homogenous nucleation at a given temperature T can simply be written as:

$$\Delta G^* = \frac{16\pi\gamma^3}{3(\Delta G_{l-s})^2} \quad (2.3)$$

The nucleation rate can be written involving ΔG^* :

$$I = K \exp\left(-\frac{\Delta G_A + \Delta G^*}{kT}\right) \quad (2.4)$$

The Equations (2.2)-(2.4) again indicate that ΔG_{l-s} should be small at any given temperature T below T_m ; that is, at an undercooling of $\Delta T = T_m - T$.

Since glass-transition is suppression of crystallization by means of kinetics, some quantitative descriptions involving the nucleation kinetics should be considered. Turnbull [17] derived the following equation for frequency of nucleation, I ;

$$I = \frac{K}{\eta(T)} \exp\left[-16\pi\alpha^3\beta / 3T_r\Delta T_r^2\right] \quad (2.5)$$

where K is a constant, $\eta(T)$ is the shear viscosity of liquid at T , T_r is T/T_1 and ΔT_r is $(T_1-T)/T_1$. Moreover, the dimensionless parameters α and β are described as;

$$\alpha = (NV^2)^{1/3} \sigma / \Delta H_f \quad (2.6)$$

$$\beta = \Delta S_f / R \quad (2.7)$$

where N is the Avogadro's number, σ is liquid-crystal interfacial energy and V is the molar volume of crystal phase. A higher magnitude of $\alpha\beta^{1/3}$ promotes glass formation by decreasing I . For most of the metallic melts it was observed that $\alpha\beta^{1/3} \approx 0.5$. ΔT_r increases with decreasing temperature and increases nucleation rate since driving force increases. This is also accompanied by decreasing T_r as temperature is lowered which imposes a lowering effect on I due to decreasing mobility. The combination of these effects results in a C-shaped TTT (time-temperature-transformation) diagrams that are well-known. However, shear viscosity which increases rapidly as temperature is decreased, overwhelms ΔT_r and lowers I .

Considering the crystallization morphologies of alloys, β defined in Equation (2.7) is the dimensionless entropy which is convenient criterion for predicting the crystallization behavior [18] and indicates the relative complexity of the born crystalline phases. From Equation (2.5), it can be confirmed that higher the β , lower the cooling rate for crystallization; thus, better the glass forming ability.

Consequently, melts which would crystallize into faceted morphologies like polymers and specifically for metallic systems; intermetallic compounds would be better glass formers since β is higher for them.

Davies et al. derived an equation [19, 20] exploiting Johnson-Mehl-Avrami transformation kinetics by deriving equations for crystal growth velocity and nucleation rate. They were first to calculate critical cooling rates for some metallic glasses by the following complex equation:

$$t \approx \frac{9.3\eta a_0^2 X}{k_B T f^3 \bar{N}_v} \left[\frac{\{\exp(1.07 / \Delta T_r^2 T_r^3)\}}{\{1 - \exp(-\Delta H_f \Delta T_r / RT)\}^3} \right]^{1/4} \quad (2.8)$$

where a_0 is the mean atomic diameter, X is a small fraction of crystal, f is the fraction of sites at crystal surfaces that attachment can occur, \bar{N}_v is average volume concentration of atoms.

$$R_c = (T_l - T_n) / t \quad (2.9)$$

By taking X as 10^{-6} to represent a detectable amount of crystal in melt, critical cooling rate (where T_n is temperature of the nose of TTT diagram) for metallic glasses can be calculated by Equation (2.9). Takeuchi and Inoue further extended the concept in a new way to involve a mismatch entropy term and, regular solution model; mixing enthalpy and entropy rather than freezing enthalpy and entropy [21]. Their model was rather empirical since it originated from the empirical rules proposed earlier and is compiled into:

$$R_c = Z \frac{k_B T_m^2}{a_0^3 \eta(T_m)} \exp \left[0.75 \left(\frac{\Delta H^M - T_m \Delta S^{ideal}}{300R} \right) - 1.2 \left(\frac{T_m S_\sigma}{300R} \right) \right] \quad (2.10)$$

Here, Z is a constant (2×10^{-6}) and S_{σ} is the mismatch entropy term described in [21]. Once enthalpy of mixing, ΔH^M and viscosity at melting temperature, $\eta(T_m)$ are known for an alloy critical cooling rate for glass formation can be estimated with Equation (2.10). Davies et al. [19] (using Equations (2.8) and (2.9)) and, Takeuchi and Inoue [21] (using Equation (2.10)) calculated the R_c for $\text{Fe}_{83}\text{B}_{17}$ metallic glass as 10^6 and 2.5×10^5 (K/s) respectively.

2.3. Semi-empirical Criteria of Glass Forming Ability

Today the mostly referred bulk glass forming criterion is that of Inoue's [22], derived by extensive experimental research. It discloses that, a high glass forming ability alloy should be; (i) a multicomponent system consisting of more than three elements, should have (ii) significant difference in atomic size ratios above about 12% the main constituent elements and (iii) negative heats of mixing among their elements. Actually, Inoue summarized the findings and experiences gained by both his group and other researchers until that day. All of these three empirical rules were previously dictated by many researchers part by part. The first rule is an outcome of the thermodynamics; more specifically, the role of entropy discussed previously in this text. The second rule is an outcome of structural models and theories reported like [23, 24] which would also briefly sustain crystallization due to competing phases. Egami and Waseda [25] were first to indicate the importance of size mismatch between constituting elements of the alloy for better glass formation. The third rule is again a thermodynamics fact which guarantees the presence of a more stable liquid without any crystalline phase nucleating in the melt at lower temperatures. In other words, it indicates a more stable supercooled liquid which can bypass crystallization more readily. In addition to these rules, there are many reported parameters supposed to define the degree of GFA. Here, the most widely referred three of them are discussed; reduced glass transition, undercooled liquid region and refined parameter.

Turnbull was first to propose a parameter named reduced glass transition temperature (T_{rg}) to compare the glass forming abilities of undercooled melts [17]. Higher the T_{rg} , better the GFA. He defined the parameter as:

$$T_{rg} = \frac{T_g}{T_l} \quad (2.11)$$

At first glance, the parameter indicates that if T_g is relatively higher and T_l is relatively lower, the melt must by-pass a smaller temperature range to freeze into a glassy state. If T_{rg} of an alloy is high, the $\eta(T)$ of the melt will rise much more rapidly as temperature is lowered (Figure 2.3) and suppress nucleation much better according to Equation (2.5). This is the kinetics behind the –famous- parameter of Turnbull; T_{rg} . Some comprehensive kinetic descriptions are also made in the Section 2.2. The parameter also emphasizes the effect of alloying additions since most of the times T_g increases and T_l decreases with increasing number and kind of solute atoms. In time, this parameter is given in almost all of the experimental papers concerning and introducing metallic glasses. Since then, this parameter remains the most widely used and valued parameter ever reported to indicate GFA. The drawback of T_{rg} arose from interchangeably calculating it as $T_{rg} = T_g / T_l$ and $T_{rg} = T_g / T_m$, denominators being either liquidus or solidus temperatures. Lu et al. mentioned that the former definition; that is the original T_{rg} definition of Turnbull which takes T_l into account is more effective in describing GFA [26, 27].

Another parameter defined as undercooled liquid region, the largeness of which actually reflects the resistance of liquid to crystallization, is also widely used in literature [28, 29]. It can be written as:

$$\Delta T_x = T_x - T_g \quad (2.12)$$

Later on, Lu and Liu proposed a refined parameter, γ [30], which is empirically derived by analyzing time-temperature-transformation (TTT) diagrams relating the T_x with the position of the curve on time axis and T_g+T_l with that on temperature axis. They defined the parameter as;

$$\gamma = \frac{T_x}{T_g + T_l} \quad (2.13)$$

This refined parameter can fairly indicate the critical cooling rate, R_c , from the regression analysis of several R_c values of metallic glass alloys with an R^2 of 0.9. When investigated carefully, it can be seen that even with that value of R^2 , any γ value calculated for an alloy has precision limits of approximately $\pm 10^4$ K/s in predicting the R_c value. The maximum attainable thickness predicting power of γ is even worse. Consequently, this parameter is not as powerful as the authors adduced. So the parameters T_{rg} and ΔT_x still remain the most respectable indicators of high GFA and will be the only ones employed in the experimental part of this study.

2.4. Structural Models of Metallic Glasses

Many theories are introduced involving structural approaches like; formulizing the topological instability of crystals, the stability of glassy state, glass transition and structural relaxation [31-37]. With a similar approach Egami theoretically derived that for better glass formation, the atomic size ratios should be high, multicomponent systems are required, small and large atoms should have strong interactions and small atoms should repel each other [34]. Lee et al. [35] employed many-body MD simulations and found that an atomic size ratio between 0.95 and 0.75 favors glass formation whereas higher ratios promote crystallization and lower ones promote phase separation. Giessen and Wagner [36] reported that the increasing complexity of stoichiometric crystalline compounds with high coordination numbers and several different lattice positions favors glass formation.

Polk and Geissen pointed out that stable intermetallics can promote the glass forming abilities of some near compositions a little far in the phase diagram [37]. All of these conditions prove one more time that the metal-metalloid systems like Fe-B, Ni-P, Pd-Si etc. are good glass formers. In TM-M alloys, metalloids forcefully lower the melting point of the alloy allowing a much rapid cooling of the liquid that could by-pass the T_g more easily. However, these metalloid atoms, donating electrons to the d-band, modify the electronic structure and affect the mechanical, electrical and magnetic properties of the alloy to a great extent which cannot be predicted via aforementioned theories.

CHAPTER 3

TOPOLOGY OF METALLIC GLASSES

3.1. Background

With the cooperative interest of industry and academia, many amorphous metal alloys have been developed since the introduction of the pioneering Au-Si system in 1960 [1]. Although laboratory experiments progressed rapidly, there still exist unresolved phenomena regarding their formation and structure. There have been several proposals to describe the form and spatial arrangement of structural units in stereochemical metallic glasses by models [38-45] and a great number of diffraction analyses yielding pair correlations [46-50]. Simultaneously, calling on the computational developments, exploration of atomic order via simulations have been encouraged as in transition metal - metalloid (TM-M) metallic glasses [51-55] and subsequently as the present study regarding amorphous Fe-B alloys.

The achieved progress stimulated research on another phenomenon called “nano-scale phase separation” in TM-M glasses [56-61] which has become tangible but lacks the concrete explanation. The mechanism behind is still unclear and structural units proposed to make up the phase separation in literature are open to debate at least in terms of polyhedral constituents and their orderings. Description of supercooling of liquids by Frank [62] initiated the investigations on aperiodic icosahedral and polytetrahedral atomic clusters in metallic melts [55, 63-65] embraced by the metallic glass formation phenomenon, and have recently been extended even to spatial arrangement of clusters [54] in TM-M amorphous alloys. The room temperature phase-separated structure substantiates the presence of that

five-fold symmetry and its compromise with local translational periodicity resembling crystalline counterparts; like bcc-Fe and Fe₃B in Fe-B system. A topological clarification of atomic aggregates, their propagation in space, connection mechanisms, contributions to radial pair correlations and bond orders is essential. In this chapter, regenerated by Monte Carlo (MC) equilibration, local structures and accompanying atomic medium range order (MRO) are revealed out in amorphous Fe₈₀B₂₀ and Fe₈₃B₁₇ alloys via identifying bond angle-length couplings, polyhedral distributions, radial distribution functions (RDFs) and their cluster-wise decompositions. A two-dimensional (2D) projection method exploiting found geometrical facts is proposed for estimating radial spacings of short to medium range coordinations.

In MC simulations, the scheme is applied to molecular systems to reveal configurational properties rather than dynamics of the systems. Although this might seem as a drawback with respect to molecular dynamics simulations, MC methods have several advantages relative to them. One advantage is that, the computational effort to solve the equations of motion are absent and another is that, thermodynamic properties are more readily calculable in MC simulations due to the fact that the simulations can be run over isothermal conditions which is not so applicable in molecular dynamics.

The basic idea behind MC simulations is that; first, a trial move is initiated for an atom or molecule, destroying the initial configuration of the system. For example, a randomly selected atom is moved by some small amount from its present position. Then the ratio of probabilities for the new and previous configurations is computed, and from this quantity a decision is made whether to accept or reject the trial move. If the trial is accepted, the new configuration is taken as the next state in the Markov chain; otherwise the original configuration is taken as the next state in the chain. Averages are collected over the many configurations generated; until the computer resources budgeted to the calculation expire.

There are quite a number of different kinds of MC ensembles and in this study the NpT [66] scheme (number of atoms, pressure and temperature are kept constant) will be identified which is more applicable to the case and also applied several times to formation of metallic glasses and amorphous systems in literature.

A pioneering work that introduced the application of Metropolis MC simulations to liquids was done by Abraham, observing the melting of liquid of hard-spheres under isothermal-isobaric condition [67]. The work of Abraham was not specific to any element and all the parameters were in reduced units, expressing no idea about the real values. In 1985, Smolander simulated aluminum in liquid and amorphous states with the MC method and extracted data was in good conjunction with the laboratory experiments [68] as shown in Figure 3.1.

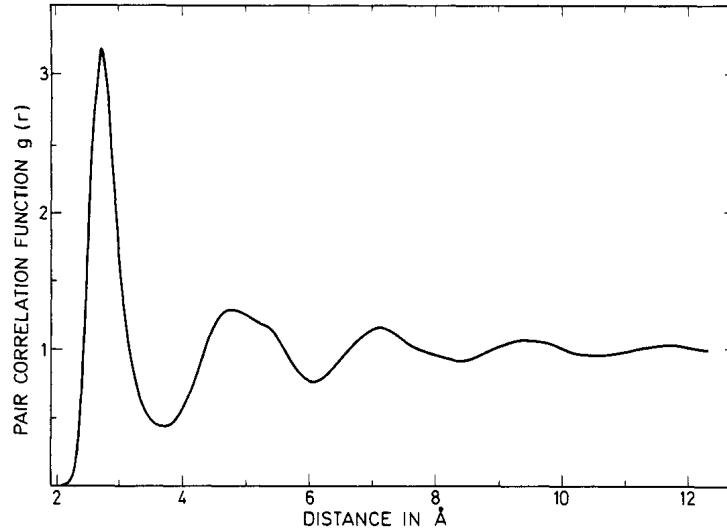


Figure 3.1 Pair correlation function for Al at 650 °C from the simulation of Smolander [68].

A more realistic simulation especially concerning the metal-metalloid binary systems was that of Bratkovsky and Smirnov [69] in which they showed that the possibility of connection of the metallic glasses simulations to real experiments. In their study, they applied the NpT scheme (See Section 3.2.1) to $\text{Fe}_{80}\text{B}_{20}$ and Ni_2B . They calculated radial distribution functions, short-range order parameters and also used the structural data coming from Monte Carlo simulations in another paper to reveal the amorphous magnetism in such alloys [70]. In Figure 3.2, their radial distribution functions and relative experimental data are shown for Ni-Ni and Ni-B pairs in the simulated Ni_2B system. Several recent computer simulations of binary liquids and amorphous solids are available in literature examining different systems and additional properties like bond angle distribution, diffusion constants, etc.[71-76].

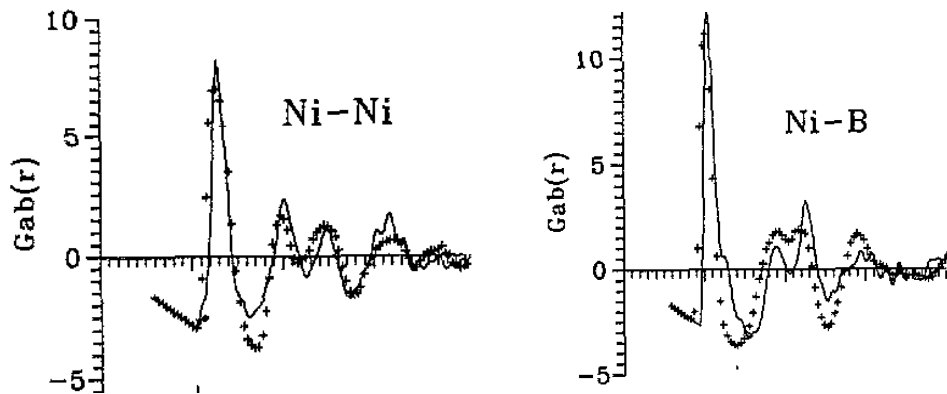


Figure 3.2 Reduced radial distribution functions of Ni-Ni and Ni-B pairs [30].

3.2. Simulation Methods

3.2.1. Isothermal-Isobaric Monte Carlo Simulation Method

This isothermal-isobaric (NpT) ensemble [66] is the most proper ensemble to study liquid-solid phase transitions since system is highly relevant to real-life conditions. In this study, ensemble is initiated in a cubic simulation cell. A randomly selected atom is shifted in a random direction with a random amount which would not exceed 1% of the edge length of the simulation cell (L). The change in the internal energy of the system, ΔU with this shift is calculated from the described pair-wise interactions. A shift resulting in a decrease in internal energy ($\Delta U < 0$) is directly accepted. However to avoid getting stuck in a local energy minimum, even if $\Delta U > 0$ the new configuration might be accepted with a pre-defined Boltzmann probability.

$$P = \exp(-\Delta U / k_B T) \quad (3.1)$$

If P defined in Equation (3.1) is greater than a random number selected in $[0,1]$ interval, the new condition is accepted. Otherwise, the atom is shifted back to the initial position. This is the so-called “Markov chain”. After a number of this atom shift trials (in our simulations this was set as two times the number of atoms), a volume changing trial is introduced which is not greater than 1% of the initial volume. After the volume change, the positions of the atoms are re-scaled relative to the origin of the cell. The change in the enthalpy of the system is calculated as;

$$\Delta H = \Delta U + P\Delta V + k_B NT \ln(V_2 / V_1) \quad (3.2)$$

The acceptance criterion is similar to the criterion for atomic shifts but now enthalpy is involved rather than sole internal energy. After this volumetric trial, a

single MC step is accomplished. This loop is repeated for a great number of times until the end of the simulation. For detailed information regarding the derivation of the NpT ensemble, the reader is referred to the study of McDonald [66]. The source code of NpT ensemble constructed is provided in Appendix B.

3.2.2. Reverse Monte Carlo Method

Since pair potentials can provide limited reproducibility of actual atomic arrangements, a further structural refinement can be conducted by Reverse Monte Carlo (RMC) method (as in [56-60]) which allows a very close fit to experimental structure factors (S(Q)'s); thus, to partial RDFs by;

$$G_{ij}(r) = 2/\pi \int_{Q_{\min}}^{Q_{\max}} S_{ij}(Q) \sin(Qr) dQ \quad (3.3)$$

The acceptance probability for multiple structure factors is defined as;

$$P \propto \exp(-(\chi_1^2 - \chi_0^2)/2) \quad (3.4)$$

where χ_1^2 and χ_0^2 are final (after an atom is moved) and initial (before that atom is moved) average squared errors between configurational and experimental structure factors, calculated as;

$$\chi_n^2 = \sum_i -\left(S_i^C(Q_i) - S_i^E(Q_i)\right)^2 / \sigma(Q_i)^2 \quad (3.5)$$

The RMC method exploits an inverse Metropolis algorithm for direct fitting to experimental findings which is quite similar to MC methods, has the same boundary conditions and has the same acceptance and rejection criteria when an atom is moved randomly. It reproduces three dimensional structural models from diffraction

data for disordered materials like metallic glasses. The equilibrium is considered to be reached when atomic configurations structure factors and experimental structure factors show a statistical difference (as an error) fluctuating around a certain average value.

3.2.3. Generation of Random Numbers

An important component of MC simulations is generation of high-quality random numbers because convergence of the system greatly depends on it. There is no practical way of computationally introducing a fully random sequence of numbers into computer simulations since computers operate on a deterministic logic. Consequently, MC simulations must be fed by pseudorandom number generators which produce unrelated integers by mathematical formulations. The periodicity of generated numbers is tested by means of statistical tests and they are out of the scope of this study. During MC simulations conducted in the present work, a Mersenne-Twister [77] type well-known pseudorandom number generator having an astronomic periodicity of $2^{19937}-1$ ($\approx 4.3 \times 10^{6001}$) was employed. This is quite a large periodicity for current study since a system of 12000 atoms requires approximately 10^{11} random numbers to be worked for 10^6 MC-steps in NpT ensemble. That algorithm was designed mainly for MC simulation purposes and satisfies the low computational effort demands. Every time the simulations are started, the generator is seeded by different numbers taken from work stations processor time.

3.2.4. Removing the Surface Effect and Employing Cut-off Radius

Although thousands of atoms are involved, the cubic simulation cell introduces six free surfaces which might greatly affect the outcome of simulations since surface-to-volume ratio is very high in any simulation that current computational

technology can handle. As a result, this surface effect must somehow be corrected and the system should imitate an infinitely continuous material. The remedy is introducing periodic boundary conditions and here the minimum image convention technique is employed. The technique is sketched in Figure 3.3 for a 2-D cross-section of 3-D simulation cell which is the centermost square surrounded by bold lines. Minimum image convention strictly prohibits the maximum range of atomic interactions to a sphere with radius equal to half the edge length of the simulation cell; $L/2$. Consequently, atom marked as “a” can only interact with atoms remaining in the large dotted-circle. An additional contraction in the interaction field is introduced by a cut-off radius (smaller dotted-circle) above which the calculations are omitted for computational efficiency. Accordingly, atom “a” interacts only with atoms marked from “b” to “f”. Now, the system can evolve free of any boundary. For details of the algorithm, see Appendix B.

3.2.5. Neighbor Lists

To increase the computational efficiency and avoid the unnecessary part of high-effort square root functions involved in separation calculations, neighbor lists are kept. They track a list of surrounding atoms up to a predefined range for every atom in the system. To remain on the safe-side, the tracking is adjusted to a radius between the cut-off radius (Figure 3.3) and $L/2$, and the lists are updated after several MC-steps. In the current study, neighbor lists tracked the atoms in a range 2.5 \AA larger than the cut-off radius and updated every 10 MC step. For details of the algorithm, see Appendix B.

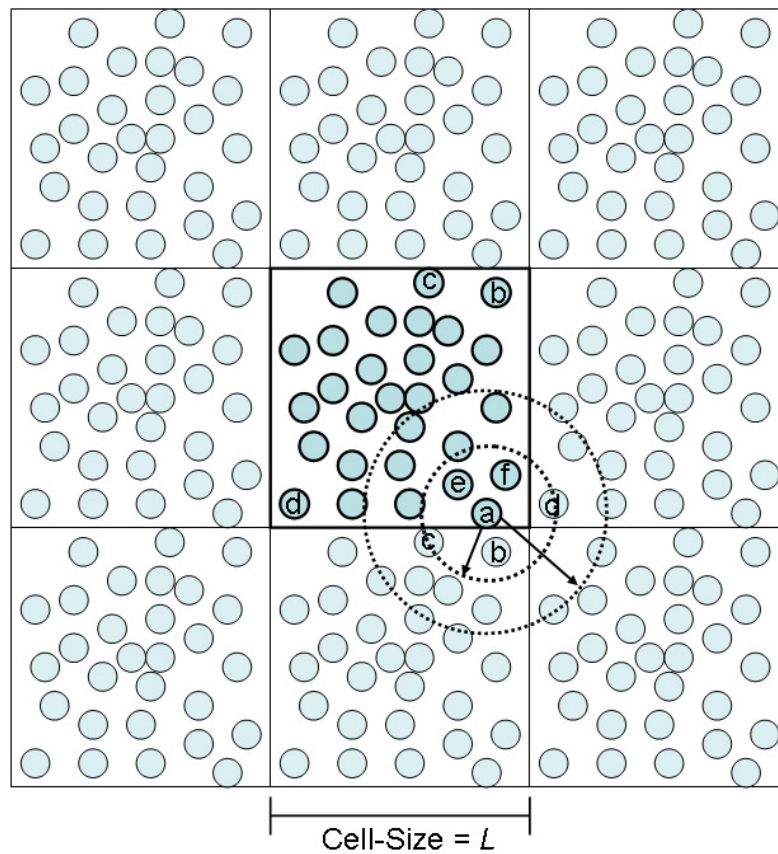


Figure 3.3 A 2-dimensional sketch of periodic boundary conditions with minimum image convention. The filled-circles represent atoms, the dotted-circle indicated by the shorter vector is cut-off sphere and dotted-circle indicated by the longer vector is the minimum image sphere of atom marked as “a”.

3.2.6. Validating the Algorithms in One Component Systems

It is of primary interest to verify all the developed software by sample experiments with small system sizes. The validation of the algorithm was conducted with a simple modified exponential potential (Equation (3.6)) rather than the binary pseudopotential interaction field (See Section 3.5), in a system comprising of 250 atoms initially in a simple cubic lattice. The potential parameters were set as $\varepsilon = 2500$ K, $\sigma = 250$ Å and $\beta = 0.0231$ Å⁻¹. The system was liquefied at 2200 K and cooled down to 100 K with 50 K intervals. The cooling rates were indirectly adjusted by varying the number of MC steps at each temperature. Accordingly, real equilibrium is only attained at the final temperature of 100 K and system might have evolved in non-equilibrium conditions upon cooling. Order of phase transitions (See Section 2.2) and transition temperatures are observed from Volume-Temperature plots in Figure 3.4 for cooling rates of 0.025 and 0.1 K/MC-s. Lower cooling rate resulted in crystallization around 950 K into an FCC structure. This was expected since exponential type non-oscillatory interactions can only crystallize into close-packed structures. Higher cooling rate yielded an amorphous structure, evident from the continuous contraction in volume (Figure 3.4) with decreasing temperature and attained radial distribution function at 100 K (Figure 3.5) which is typical of an amorphous system. The characteristic splitting in the second peak is observable. Sample snapshots of both structures are compared in Figure 3.6. According to these results, the algorithm works without flaws and it can be employed for larger systems which require run-times of several weeks.

$$V(r) = \varepsilon \left[\exp^2(-\beta(r - \sigma)) - 2 \exp(-\beta(r - \sigma)) \right] \quad (3.6)$$

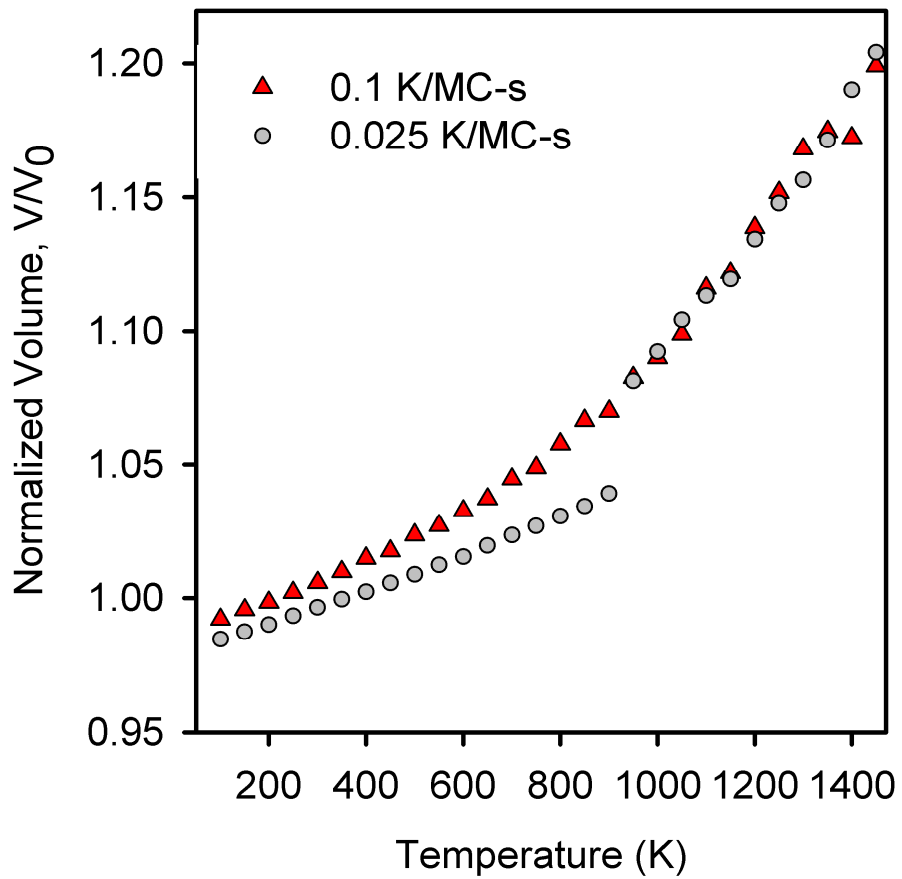


Figure 3.4 The effects of different MC cooling rates on accompanying phase transitions are shown by variation of volume with temperature.

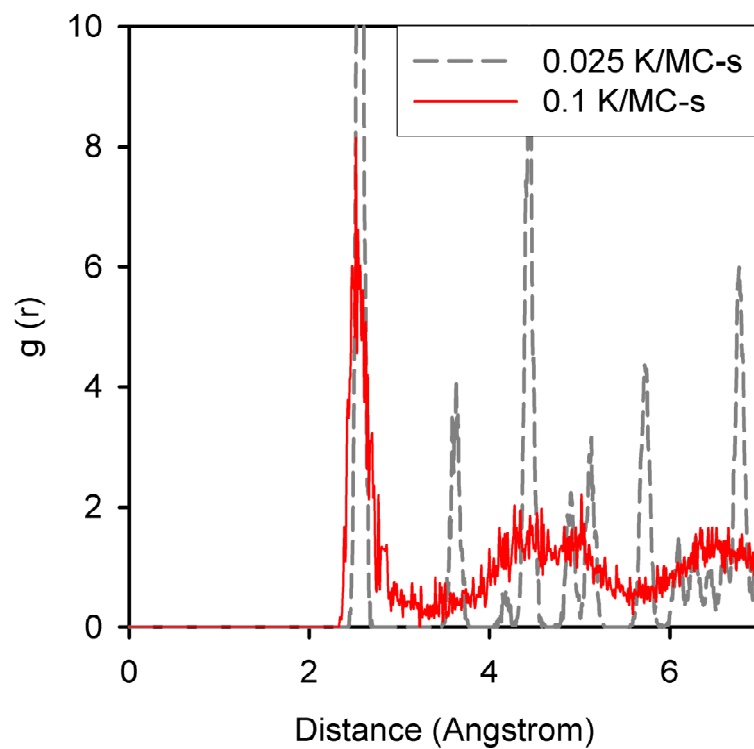


Figure 3.5 The structures attained at 100 K and corresponding radial distribution functions after applying different cooling rates.

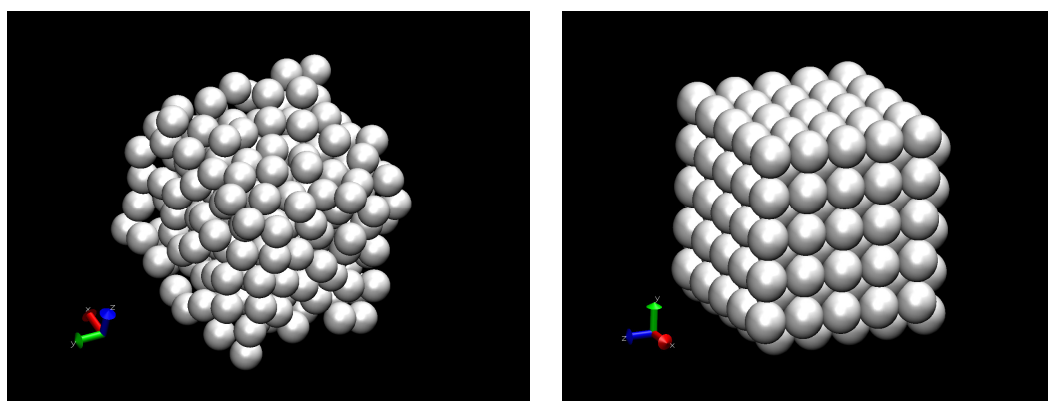


Figure 3.6 Left and right images are snapshots of simulation cells taken after equilibrium at 100 K after 0.1 and 0.025 K/MC-s cooling rates respectively. Left structure is amorphous whereas the right one is an FCC crystal.

3.3. Structural Correlation Tools

3.3.1. Radial Distribution Function

There is a need of a comprehensive structural correlation tool which can reflect the spatial atomic arrangements in “real” Euclidean 3-dimensional space. Radial distribution functions are the most applied pair-wise correlation tool in any kind of structural or dynamical simulation regarding amorphous structures. Radial distribution function defines the relative density of a certain kind of atom at a position r to an origin atom to a completely random distribution in bulk density as shown in equations below:

$$g(r) = \frac{\rho(r)}{\rho_0} \quad (3.7)$$

$$g(r_{i,j}) = \left\langle \frac{N_{i,j} / 4\pi r_i^2 dr}{3N / 4\pi r_i^3} \right\rangle_{i,j} \quad (3.8)$$

RDF can be calculated as an average over all j atoms in the system where $N_{i,j}$ is the number of particles at a distance of r_i and $r_i + dr$ to the origin atom j , and N is the total number of atoms. Coordination number defined by a minimum and maximum separation can be calculated as:

$$Z = \int_{r_{\min}}^{r_{\max}} 4\pi r^2 \rho_0 g(r) dr \quad (3.9)$$

Radial distribution function has a reduced form which can be written as:

$$G(r) = 4\pi r \rho_0 [g(r) - 1] \quad (3.10)$$

The algorithm of calculating RDF from atomic coordinate data is presented in Appendix B in C++ programming language.

3.3.2. Bond Angle Distribution Function

Bond angle distribution (BAD) function is a simple correlation tool indicating short-ranged structural tendencies. It is actually a simple triplet correlation tool proposed by Hafner [78] and is comprised of radial averages over triplet correlation functions. It can easily be calculated from coordinate data by measuring the angle formed by a central atom and its two nearest neighbors. The algorithm of calculating BAD from atomic coordinate data is provided in Appendix B in C++ programming language.

3.3.3. Bond Length-Angle Hypersurface Analysis

Analyzing the degree of participations of bonds with certain lengths in angle formations can be very descriptive. A trivial bond length-angle hypersurface (BLAH) is proposed in Equation (3.11). Its normalized counterpart is given in Equation (3.12). Here, N is the total number of atoms, $N_3^{i,1}(\theta, |\mathbf{r}|)$ is the total number of triplets that are formed by an origin atom i , an atom at a distance $|\mathbf{r}|$ to i in its first CS and remaining atoms in the first CS at an angle θ to the vector \mathbf{r} . Normalization is done by division to the total number of those triplets at all θ in $[0, \pi]$. By plotting these surfaces, angle accumulations to certain bonds and average angles that a bond with a certain length is involved can be identified.

$$B(\theta, |\mathbf{r}|) = \sum_{i=1}^N N_3^{i,1}(\theta, |\mathbf{r}|) \quad (3.11)$$

$$B_{\perp}(\theta, |\mathbf{r}|) = \frac{\sum_{i=1}^N N_3^{i,1}(\theta, |\mathbf{r}|)}{\sum_{i=1}^N N_3^{i,1}(|\mathbf{r}|)} \quad (3.12)$$

3.3.4. Voronoi Analysis

A convenient path of revealing the atomic structure is separating it into units of different scales and moving from smaller to larger ones, accumulating information in every step. An atom and its “touching” local environment make up the smallest structural unit that is dealt with. This sense can mathematically be formulated by division of Euclidean-space into convex polyhedra via Voronoi analysis. This yields a statistical distribution of polyhedra, each formed around a certain kind of atom by its neighbors and here, it is denoted by the common polygonal notation $\langle n_3, n_4, n_5, n_6, n_7, n_8, \dots \rangle$ where n_i is the number of facets having i vertices in the notated polyhedron. Voronoi polyhedron is the counterpart of Wigner-Seitz Cells of crystal lattices in amorphous structures. The extraction of Voronoi polyhedra coordinate data is rigorous and described in Appendix B.

3.3.5. Short Range Order Parameters

Order parameters indicate the tendencies for hetero-coordination and have several different kinds proposed in literature. Two different short range order (SRO) parameters; generalized-Warren (α) [79] and Cargill-Spaepen (η) [80] were adopted. The former is defined as;

$$\alpha = N_{CC}/N_W \quad (3.13)$$

where,

$$N_{CC} = x_i N_j + x_j N_i - N_{ij}/x_j \quad (3.14)$$

$$N_W = x_i N_j + x_j N_i \quad (3.15)$$

The latter is defined as:

$$\eta = N_{ij} N / x_j N_j N_i - 1 \quad (3.16)$$

The maximum possible values of α and η for a certain composition are defined as;

$$\alpha_{\max} = -\min(x_i, x_j) / \max(x_i, x_j) \quad (3.17)$$

$$\eta_{\max} = -\min(x_i N_i, x_j N_j) / \max(x_i N_i, x_j N_j) \quad (3.18)$$

In Equations (3.13)-(3.18), N is the average coordination number of the alloy, N_i (or N_j) is total coordination number of an i (or j) atom, N_{ij} is the number of j neighbors of an i atom and x_i (or x_j) denotes the atomic fraction.

3.3.6. Cluster-Size Distribution Analysis

The analysis was performed by measuring the distance from an atom (Fe atom) to the closest vertex of a TP unit; thus revealing the minimal-cluster-dimensions computational method of which is given in Appendix B.

3.4. Simulation Procedures

The interest of this study is the topology of the glassy state rather than its occurrence dynamics. A system containing thousands of atoms is required. Accordingly, a computationally cheaper method like MC equilibration is fulfilling

enough. Amorphous-Fe₈₀B₂₀ and -Fe₈₃B₁₇ alloys were first liquefied at 2000 K, then quenched to 300 K and equilibrated with isothermal-isobaric MC method [66] comprising of 12000 atoms in a cubic cell. Periodic boundary conditions; minimum image convention, neighbor lists, a Mersenne-Twister [77] type random number generator having an astronomic periodicity of $2^{19937}-1$ were employed. The cut-off radius was set as 10 Å. Each run of the simulation consisted of at least 10^6 MC steps, each of which involves two trajectory trials for every atom and a volume changing trial once. Averages are taken over 500 sample configurations after equilibrium is reached.

In RMC simulations, setting the atomic coordinates of MC simulations rather than a random configuration as input, RMCA program [81] was used and fitting was done to three partial structure factors provided in [46] for Fe₈₀B₂₀.

3.5. Calculating an Interaction Field from Pseudopotential Theory

First, to obtain a typical amorphous TM–M structure, a moderately satisfying interaction field shall be developed. An interaction field by using first principles pseudopotential theory was derived for amorphous Fe-B alloys. Such a computation in multi-component systems can be described by the electronic theory of alloys in the pseudopotential approximation and is discussed in detail, including several calculations and applications elsewhere [82-89]. The configuration dependent part of the internal energy in alloys consists of band structure energy E_{bs} and electrostatic energy E_{es} .

$$V_{\alpha\beta}(r_i) = \frac{\bar{\Omega}}{\pi^2} \int F_{\alpha\beta}(Q) \frac{\sin qr_i}{Qr_i} Q^2 dQ \quad (3.19)$$

where,

$$F_{\alpha\beta}(Q) = -\frac{\bar{\Omega}}{8\pi} |\omega_{\alpha}^{\circ}(Q) \omega_{\beta}^{\circ}(Q)| Q^2 \frac{\varepsilon(Q)-1}{\varepsilon^*(Q)} + \frac{2\pi}{\Omega Q^2} |Z_{\alpha}^* - Z_{\beta}^*| e^{-\frac{Q^2}{4\xi}} \quad (3.20)$$

Here, $\bar{\Omega}_0$ is the average atomic volume of the alloy, $\varepsilon(Q)$ is the dielectric constant in Hartree approximation, $\varepsilon^*(Q)$ is the modified dielectric constant which takes into account the correlation and exchange effects [90], $\omega_{\alpha}^{\circ}(Q)$ and $\omega_{\beta}^{\circ}(Q)$ are the form factors of an unscreened pseudopotential of α and β component ions respectively, $Z_{\alpha}^*(Z_{\beta}^*)$ is the effective valency of the $\alpha(\beta)$ component atoms and η is the Ewald parameter. Equations (3.19) and (3.20) enable one to calculate partial interatomic interaction energies as a function of interatomic distance, R , for any alloy provided that the form factor of unscreened pseudopotentials, $\omega^{\circ}(Q)$, and effective valences, Z^* , are known for the ions involved. Unlike simple metal alloys, the form factor of the pseudopotential for transition metals must contain terms responsible for the d-resonance effect. The model pseudopotential employed in our calculations in which the d-resonance effect is partly taken into account for transition metals is given by Animalu [91]. It is known that there exists no B-B nearest neighbors in amorphous Fe-B alloys; consequently, B-B interactions are modified accordingly with an r^{-12} type repulsion at distances smaller than the second coordination sphere. The calculated interatomic pair potentials are shown in Figure 3.7. The potentials possess an oscillatory behavior even at larger spacings, which is an expected behavior in metallic systems.

3.6. Results and Discussion

3.6.1. Comparison of Interaction Fields in Fe-B system

Although there are a great many variables like initial configuration, cell-size (number of atoms), simulation time, type of boundary conditions, quality of random numbers (in MC) etc., the most important variable in any kind of atomic simulation

is the description of the interaction field of atomic pairs and non of the remaining variables can have such a great influence on final atomic configuration. A comparison of available Fe-B binary interaction fields reported in literature and current field calculated from first-principle pseudopotential theory in this study shall be a concrete initial evaluation. In addition to as-calculated potential, two different and mostly referred pair potentials of Fe-B binary; namely, the one calculated by Hausleitner and Hafner [52] (reproduced and plotted in Figure 3.8), and the truncated Morse-type [92] (calculated by Equation (3.21) and plotted in Figure 3.9) are employed. Parameters of Morse-type potential are listed in Table 3.1 and truncation function φ can be found in [92]. All of the simulations have exactly the same initial configurations and initial parameters like temperature, pressure and atom number.

$$V(r) = \varepsilon_0 [\exp(-2\alpha(r/r_0 - 1)) - 2\exp(-\alpha(r/r_0 - 1))] \varphi(r/r_c) \quad (3.21)$$

To show that there is no detectable equilibration time (as an MC simulation variable) problem, volume versus MC-step (simulation time) plots for all three distinct simulations are given in Figure 3.10. The plots show that volumetric fluctuations are immediately stabilized around an average value in all simulations after certain number of MC-steps.

Results of different MC simulations with different pair potentials are given in Figure 3.11 for Fe-Fe RDF. Unfortunately non of these potentials were capable of reproducing the experimental RDF as the current pair potential involved in simulations, especially at MRO distances starting from second coordination sphere. Consequently, the current pair potential seems as the most reasonable among other potentials and further studies do not include these two other pair-potentials (available in literature).

Table 3.1 Parameters of truncated Morse-type potential [92].

Parameter	Fe-Fe	Fe-B	B-B
r_0 (Å)	2.67	2.24	3.67
ε_0 (eV)	0.51	0.54	0.024
α	4	5	8
r_c (Å)	5	5	5

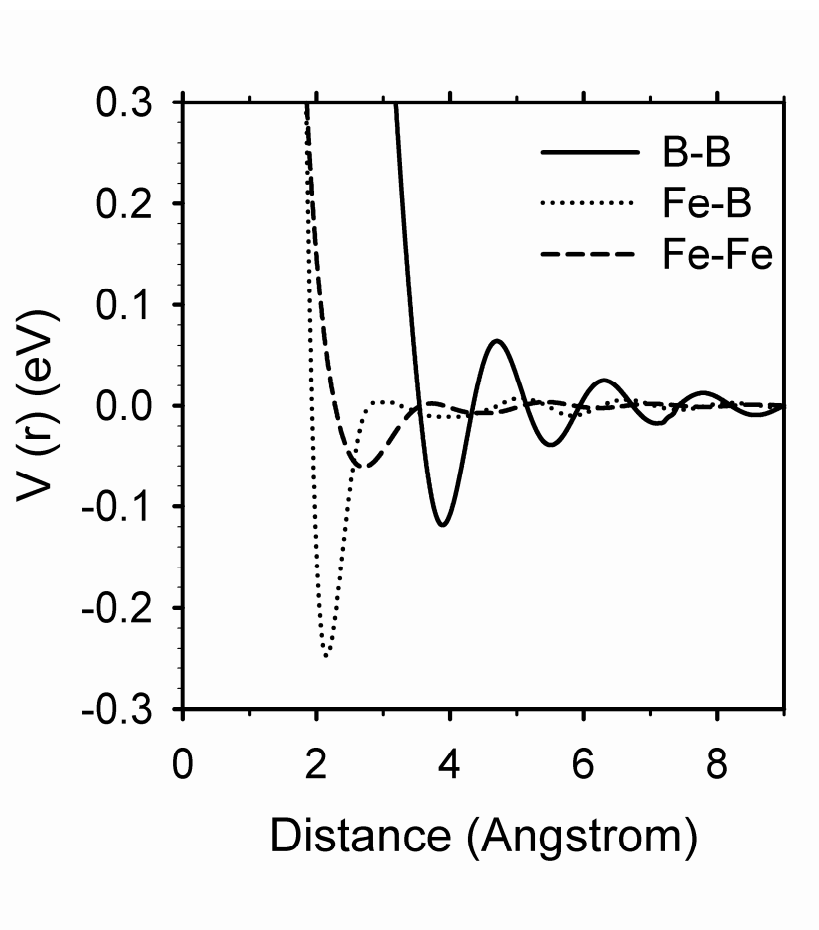


Figure 3.7 Calculated interatomic pair potentials versus distance in Fe-B system.

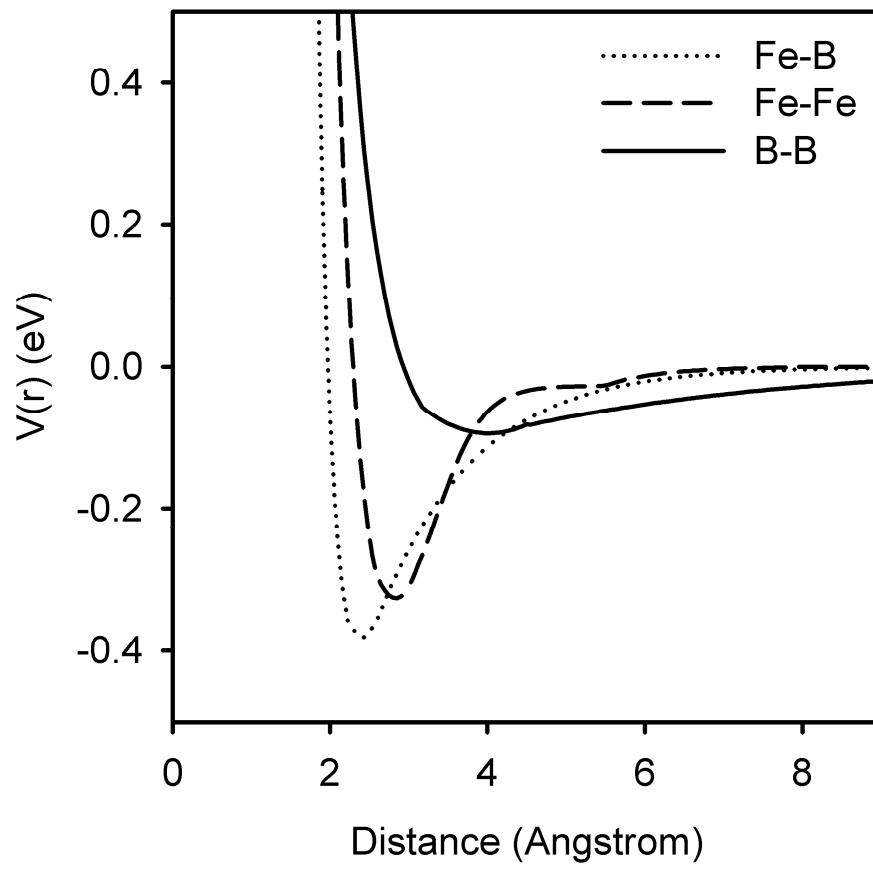


Figure 3.8 Interaction field reported by Hausleitner and Hafner [52] for Fe-B binary system.

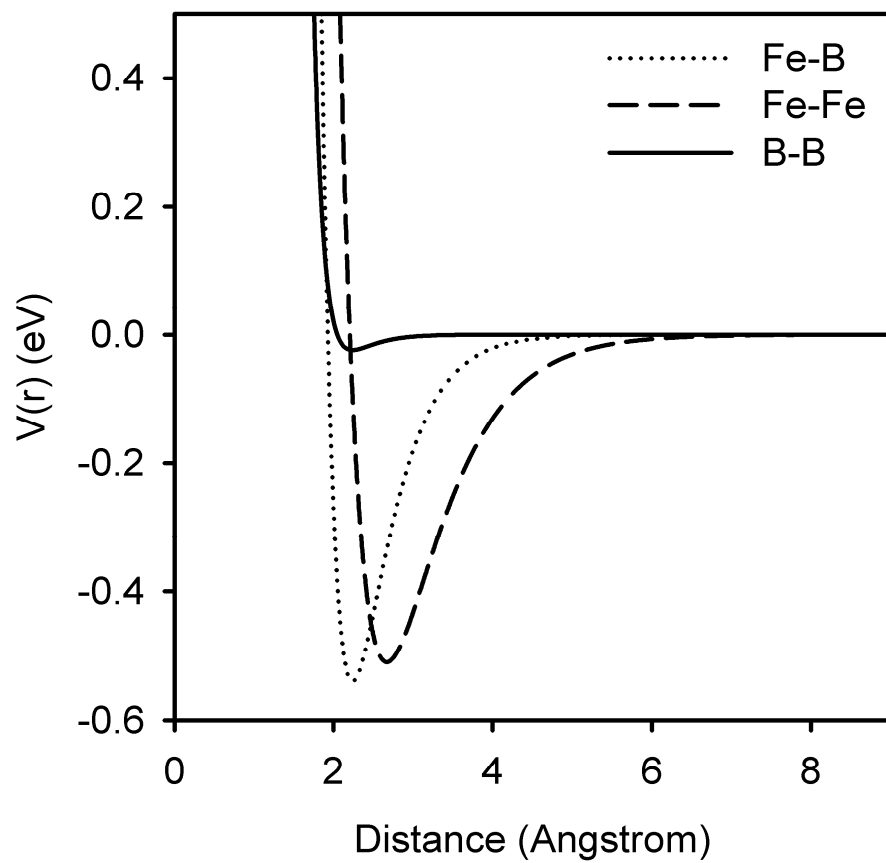


Figure 3.9 Morse-type interaction field for Fe-B binary system reported by Fujiwara et al. [92].

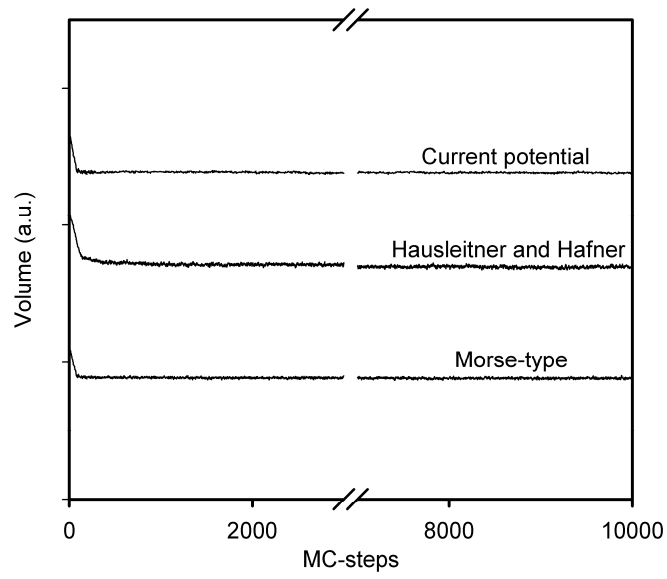


Figure 3.10 Change of volume by MC-steps for all applied pair potentials. Plots are shifted arbitrarily for clarity.

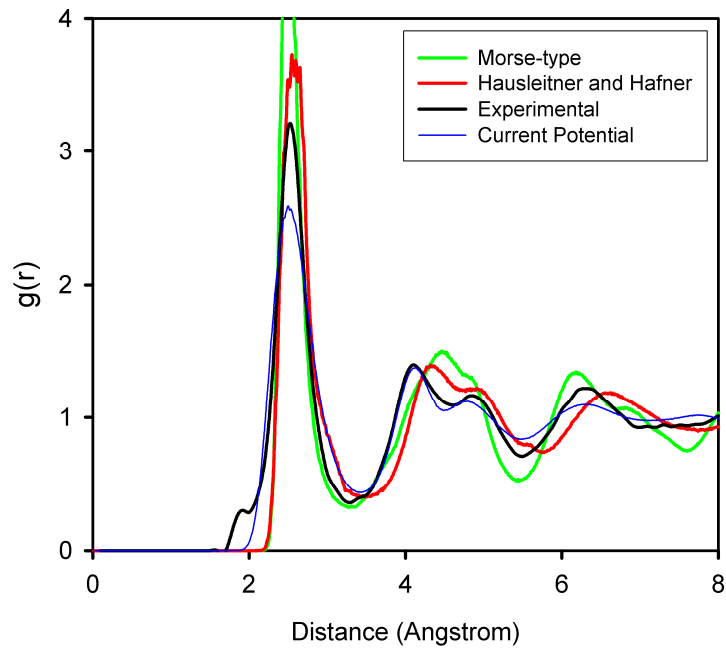


Figure 3.11 RDFs of Fe-Fe pairs, reproduced by different types of pair potentials and compared to experimental Fe-Fe RDF of Nold et al [46].

Pair-wise interaction potentials in Fe-B system calculated and used further in this study are given in Figure 3.7. Atomic bonding with completely metallic nature would be produced by a soft pair potential. Fe-Fe interactions are calculated with a shallow and smooth first well depth. When neutron diffraction results of Nold et al. [46] are examined, it can be found that Fe-B separation is closer to the sum of covalent radii of Fe and B atoms. Consequently, one might expect a covalent bonding tendency between Fe and B atoms, which would yield a strong interaction. As a result, Fe-B well depth turned out deep. B-B interaction in first coordination sphere was not observed in amorphous Fe-B alloys [46] and calculated potentials are capable to avoid this B-B neighboring. The potentials possess an oscillatory behavior even at larger spacings, which is an expected behavior in metallic systems to impose MRO.

3.6.2. Structural Refinement

Prior to gaining more insight into TM-M glasses, a set of typical and sufficiently representative structural data should be reproduced. Accordingly, the reduced partial RDFs of $\text{Fe}_{80}\text{B}_{20}$ acquired from the MC and RMC simulations were compared to the neutron diffraction experiment results of Nold et al. [46] in Figure 3.12. In RMC simulations, a perfect agreement with experiment is obtained. In MC simulations, carrying traces of all prevailing coordinations, a satisfyingly close fit was obtained for further investigations. However, origins and possible influences of deviations of partial RDFs from the experimental ones shall be clarified by comparing the MRO structures of MC and RMC simulations since structural units or clusters might be contingent upon those. Although peak positions are quite consistent for pair potential interacted MC, their amplitudes and widths show deviations from the experimental RDFs. These could directly be related to current descriptions of interaction fields of atomic pairs. Moreover, although a large number of atoms, periodic boundary conditions and cut off radii larger than MRO separations are employed, limited simulation cell size may also have contributed to

variations in RDFs. The amplitude and width differences may also have arisen from the limited attainment of large relaxation times of simulations because the integrated RDFs revealed coordination numbers (CNs) of first coordination spheres (CSs) in all of the Fe-Fe, Fe-B and B-Fe pairs consistent with previous reports (Table 3.2), integrated areas of higher CSs match with those of experimental RDFs and calculated density of the alloy has only -0.2 % deviation from experimental density of 7.3 g/cm³. Consequently, local relaxation differences are expected rather than fundamental topological differences in structural units or clusters making up the atomic order in short and medium ranges which is discussed in Section 3.6.3. In detail, there exists a slight common loss as mentioned in [52] of structure in the second (splitted) peak of MC simulated Fe-B in Figure 3.12a and a slight gain of structure in the third peak. The reason of the former lies beneath the Fe-Fe RDF in which the first peak turned out slightly wider, directly broadening the individual overlapping peaks that make up the splitted peak of Fe-B. This is the dependent-variable nature of getting further from merely the “touching” atom arguments, of which will be made use later in this context.

In addition to CNs, first neighbor interatomic distances ($d_{\text{Fe-B}}$ and $d_{\text{Fe-Fe}}$) of Fe₈₀B₂₀ and Fe₈₃B₁₇ are quite consistent with reported experiments [46, 57] as listed in Table 3.2. A negative α and a positive η (See Table 3.2) indicate presence of SRO. Fe₈₃B₁₇ has both α and η smaller in magnitude relative to Fe₈₀B₂₀ which shows an increasing clustering tendency with increasing Fe content. Parameters can be normalized by dividing them to their maximum possible values defined by Equations (3.17) and (3.18) to clarify the degree of ordering tendency. As listed in Table 3.2, the normalized order parameters α° and η° are equal for both compositions. The α° values turned out to be 0.49, which is very similar to the values calculated for TM-M glasses [79]. The η° values are equal to unity, indicating maximum possible local ordering has occurred. This is an expected outcome of the lack of B-B neighboring and $N_{\text{B-B}}$ being equal to zero.

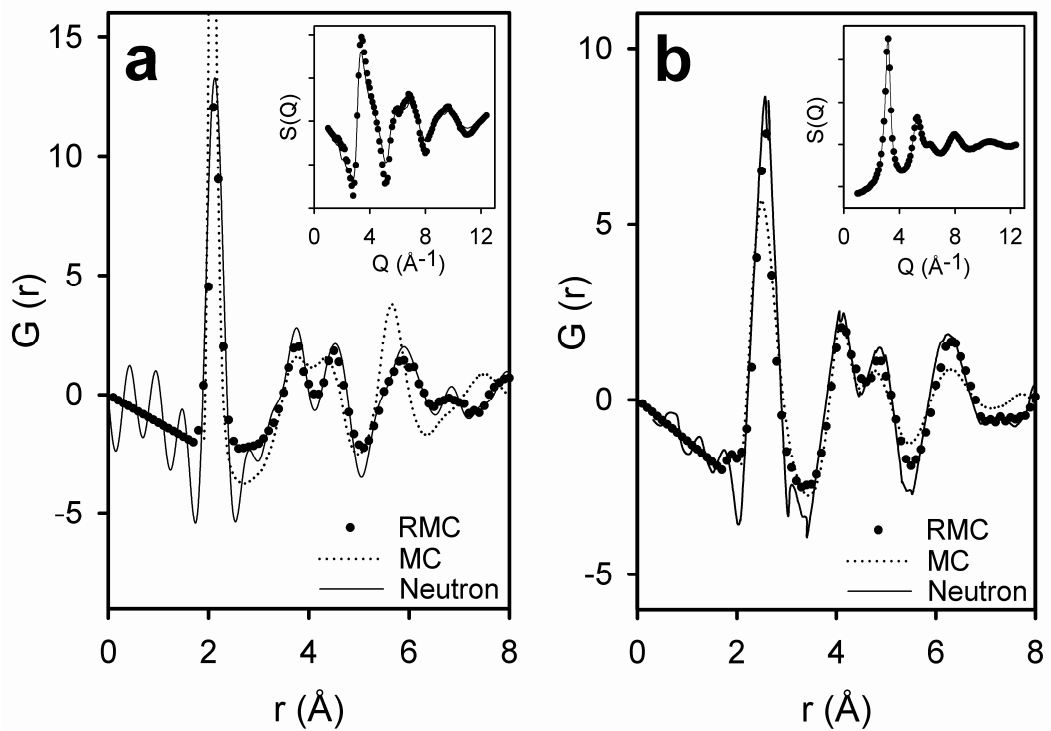


Figure 3.12 Reduced RDFs, $G(r)$'s, of $\text{Fe}_{80}\text{B}_{20}$, (a) being the Fe-B pairs and (b) the Fe-Fe pairs. Solid lines represent the reproduced experimental results of Nold et al. [46] mentioned as Neutron, dotted lines represent results of MC simulations and black dots represent results of RMC simulations. Insets show RMC fittings to corresponding experimental partial structure factors.

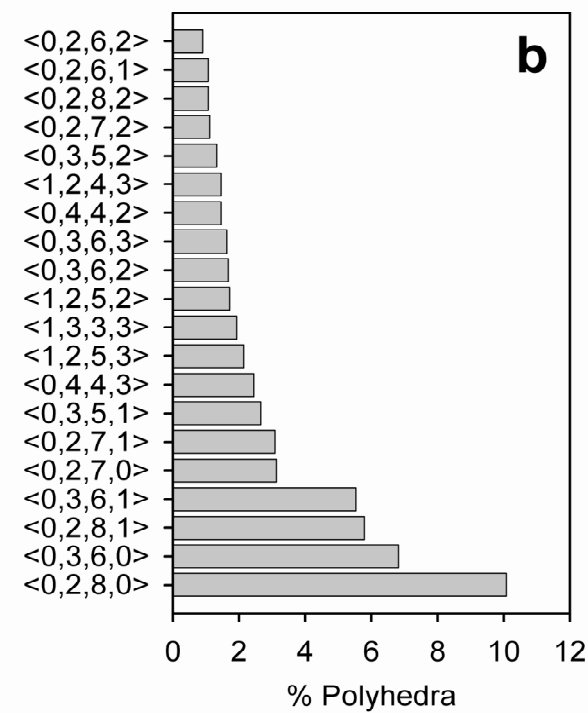
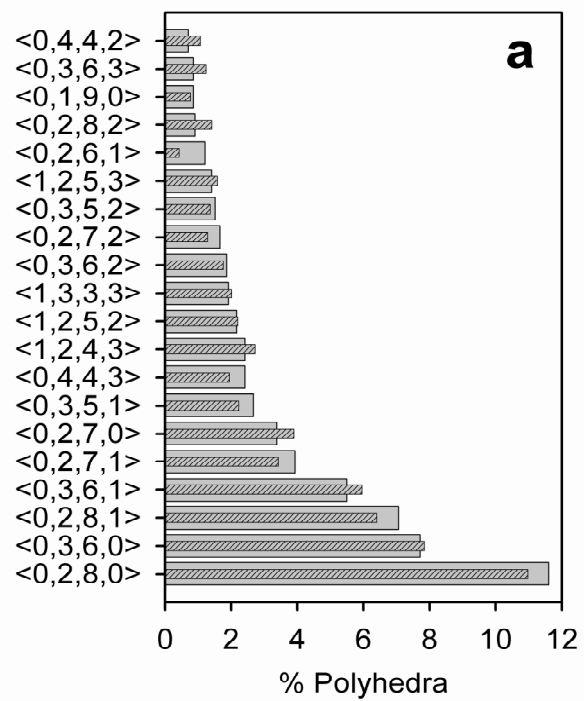


Figure 3.13 Voronoi diagrams of B centered polyhedra in (a) Fe₈₀B₂₀ and (b) Fe₈₃B₁₇. Full bars and thin crossed bars represent results of MC and RMC simulations respectively.

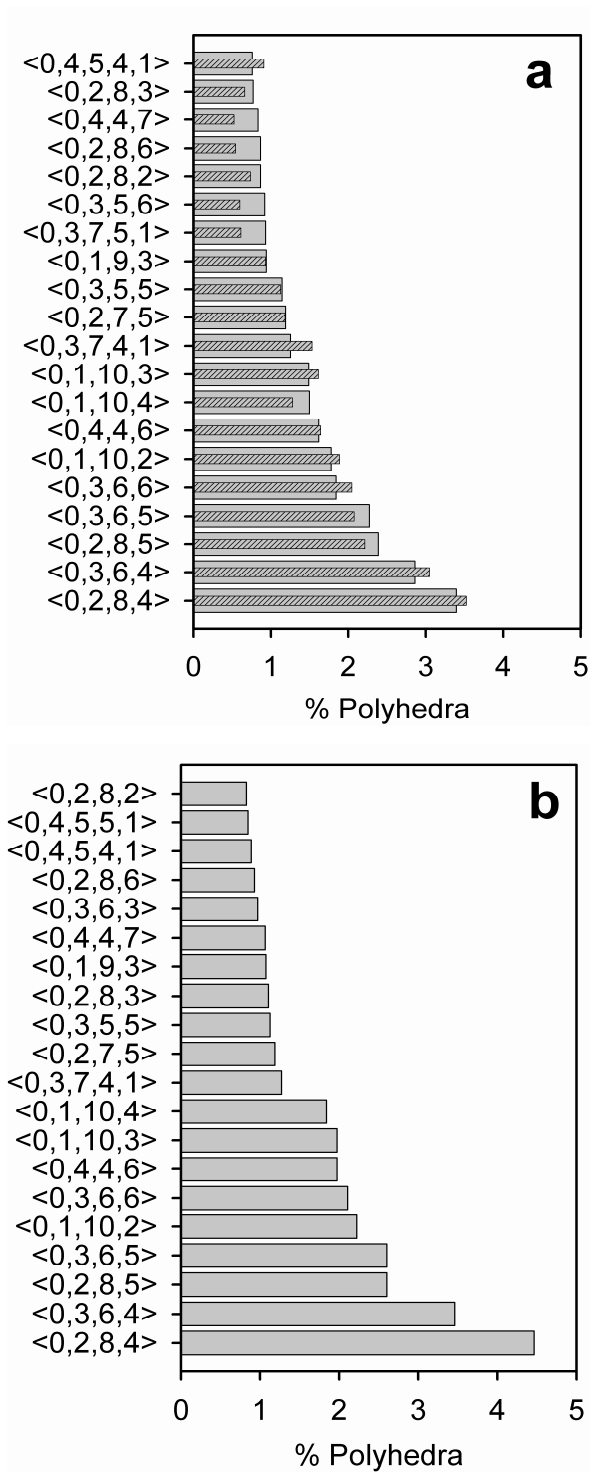


Figure 3.14 Voronoi diagrams of Fe centered polyhedra in (a) $\text{Fe}_{80}\text{B}_{20}$ and (b) $\text{Fe}_{83}\text{B}_{17}$. Full bars and thin crossed bars represent results of MC and RMC simulations respectively.

Table 3.2 Partial coordination numbers of Fe-Fe, B-Fe (Fe around B), and Fe-B (B around Fe) pairs are listed respectively. The calculated interatomic spacings and order parameters are also listed. Standard deviations for calculated partial coordination numbers and interatomic spacings are ± 0.03 and ± 0.01 respectively for all pairs.

	Fe ₈₀ B ₂₀	Fe ₈₃ B ₁₇	Fe ₈₀ B ₂₀ ^a	Fe ₈₀ B ₂₀ ^b	Fe ₈₃ B ₁₇ ^b
$N_{\text{Fe-Fe}}$	11.59	11.98	12.4	11.8	12.2
$N_{\text{B-Fe}}$	8.75	8.9	8.6	9.3	9.4
$N_{\text{Fe-B}}$	2.19	1.82	2.2	2.4	1.9
$d_{\text{Fe-B}} (\text{Å})$	2.16	2.18	2.14	2.06	2.1
$d_{\text{Fe-Fe}} (\text{Å})$	2.52	2.55	2.57	2.57	2.58
$\eta (\eta^\circ)$	0.16 (1.0)	0.13 (1.0)	0.148	0.18	0.14
$\alpha (\alpha^\circ)$	-0.12 (0.49)	-0.10 (0.49)			

^aNold et al. [46], ^bHirata et al. [57].

3.6.3. Voronoi Analysis

The reproducibility of MRO structures, units of which are identified directly by Voronoi analysis, should be investigated at first. It can be seen that although RDFs of MC simulations (Figure 3.12) show deviations from experimental RDFs, the MRO structures in Figure 3.13a and Figure 3.14a; i.e., the Voronoi polyhedra show no significant difference from perfectly fitted RMC results in terms of both types and frequencies which approves the dependability of depicted MRO structures of MC results. In Voronoi diagram of B centered polyhedra (Figure 3.13a and Figure 3.13b), high frequency $\langle 0,2,8,0 \rangle$ and $\langle 0,3,6,0 \rangle$ polyhedra correspond to 10 coordinated Archimedean Antiprism (AA) and 9 coordinated tri-capped trigonal prism (TTP) respectively, both being close to crystal structures of Fe₃B. AA is a

distorted form of TTP. Both will be referred as trigonal prisms (TPs). $\langle 0,2,8,x \rangle$ and $\langle 0,3,6,x \rangle$ dominate the structure with minor contributions from $\langle 0,2,7,x \rangle$, $\langle 0,3,5,x \rangle$ and $\langle 0,4,4,x \rangle$ (x between 0 and 3), all being the deformed types of corresponding basis polyhedra. Increasing B-Fe CN increased the fraction of these prismatic units in $\text{Fe}_{83}\text{B}_{17}$.

In Voronoi diagram of Fe (Figure 3.14a and Figure 3.14b), $\langle 0,2,8,4 \rangle$ and $\langle 0,3,6,4 \rangle$ appear in higher amounts followed by their derivatives ($\langle 0,2,8,5 \rangle$, $\langle 0,3,6,5 \rangle$ and $\langle 0,3,6,6 \rangle$), all corresponding to “so-called” deformed-bcc (d-bcc) polyhedra. Deformed icosahedra (d-ico) like $\langle 0,1,10,2 \rangle$ and $\langle 0,2,8,2 \rangle$ are also observed. Purely bcc $\langle 0,6,0,8 \rangle$ and purely icosahedron (ico) $\langle 0,0,12,0 \rangle$ structures are observed but with low frequencies (<1%). All the polyhedra have CNs of 13-14 except some low frequency 15 and 16 coordinated polyhedra. In $\text{Fe}_{83}\text{B}_{17}$ (Figure 3.14), an increase is observed in both $\langle 0,2,8,4 \rangle$ and $\langle 0,3,6,4 \rangle$ frequencies due to the increase in Fe-Fe CN. All of the polyhedra corresponding to Fe, even the d-bcc ones can be obtained by -72° and $+72^\circ$ disclinations imposed on a perfect ico. Throughout the alloy, Fe establishes neither a perfect bcc nor a perfect ico, and all the polyhedra are actually in-between; some closer to ico, some to bcc. Consequently, for clarity, the analyses pertinent to the nature of local arrangements shall be focused on.

3.6.4. Bond Angle and Length-Angle Hypersurface Analyses

No significant difference was observed between the bond angle distributions of $\text{Fe}_{80}\text{B}_{20}$ and $\text{Fe}_{83}\text{B}_{17}$ so only that of $\text{Fe}_{80}\text{B}_{20}$ are sketched in Figure 3.15. Fe-Fe-Fe triplet has peaks near 55° , 106° and 152° . These can be attributed to d-ico but not as much to highly occurring d-bcc. This anomaly will be clarified later. Fe-B-Fe triplet yields peaks corresponding to 67° and 135° . A pentagon has two distinct central angles; 72° and 144° . In a TP, a B atom is slightly displaced from the normals of pentagons (Figure 3.23) formed by nearly co-planar Fe atoms; as a consequence of

which, angles should be slightly narrower than central pentagonal angles as they turned out. B-B-B triplet BAD, imputed to MRO, demonstrates a pronounced cluster-ordering. All of the peaks agree on an icosahedral ordering with small distortions. But ico can reflect peaks at 63.4° , 116.4° and 180° from the center and in a broader sense peaks at 60° and 108° from vertices. None of these angles are unique to a fully ico structure and can be produced also by a polytetrahedral ordering. The peak around 90° supports this fact and indicates that some pentagonal prisms or close-packed orderings may also exist.

By plotting BLAH functions, angle accumulations to certain bonds and average angles that a bond with a certain length is involved can be unveiled in as given in Figure 3.16 for Fe-Fe doublets. It can be seen that as the bonds shorten, they prevail in higher angles in any case.

The BLAH considering all nearest neighbor (NN) Fe (Bulk Fe NN; Figure 3.16) atoms possesses three maxima having “teardrop” shapes, tails extending to wider bonds and lower angles. In normalized BLAH Bulk Fe, it can be seen that the three-maximum form of the surface does not alter; however, as the Fe-Fe bonds are stretched, acute angle peak and two wide angle peaks also shift to lower angles. During stretching, while acute angle peak gets narrower, the wide angle peak next to it broadens and loses intensity. Stretched bonds can adopt nearly right angles and angles smaller than 60° ; whereas, in the limit, short bonds pass slightly above 60° and 108° , and intensify near 180° .

The BLAH formed by NN Fe atoms of isolated TP units (Intra-cluster Fe NN; Figure 3.16) possess two maxima also having the characteristic teardrop shape. With this confinement, the wide angle peak near 152° disappeared, proving itself to be an inter-clusteral trait; *i.e.* a connection zone (CZ) argument. Remaining peaks reflect highest intensities at exact ico-shell angles 60° and 108° . In normalized BLAH of that, the wide angle peak ($\sim 108^\circ$) can shift to ranges even less than 90° and low angle peak ($\sim 60^\circ$) to around 45° at high stretchings, relative fraction of low

angles to wide angles increasing at the same time. This can be interpreted as; angular arrangement is strictly of the same shape for all NN Fe-Fe bond lengths in a TP; *i.e.* a bond order prevails, and compensations for local distortions shift the positions of maxima.

Fe atoms common to two neighboring TPs are regarded to make up a CZ. When NNs of the atoms in a CZ are considered (Fe NN CZ), the common three-maximum outline is observed in Figure 3.16. Accumulations around 60° confirm tetrahedral CZs, being not unique to any connection mode between TPs; vertex sharing (VS), edge sharing (ES) or face sharing (FS). Presence of the wide angle peak around $\cos^{-1}(0.3)$ (an internal TP angle) indicates ES and FS. Shorter bonds tend to participate in such angles more according to the normalized profile. Belonging solely to the CZ, the leftmost wide angle peak that disappeared previously reappeared with the highest intensity.

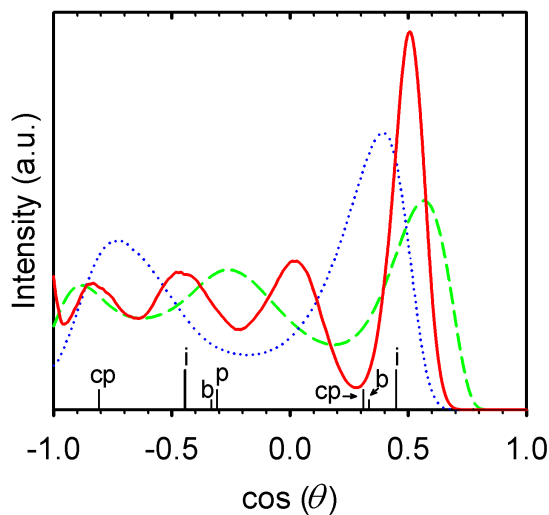


Figure 3.15 BAD functions for Fe-Fe-Fe (dashed line), Fe-B-Fe (dotted line) and B-B-B (solid line) triplets in $\text{Fe}_{80}\text{B}_{20}$. At the bottom, cp denotes central pentagonal, i; icosahedral, b; bcc and p; pentagonal angles.

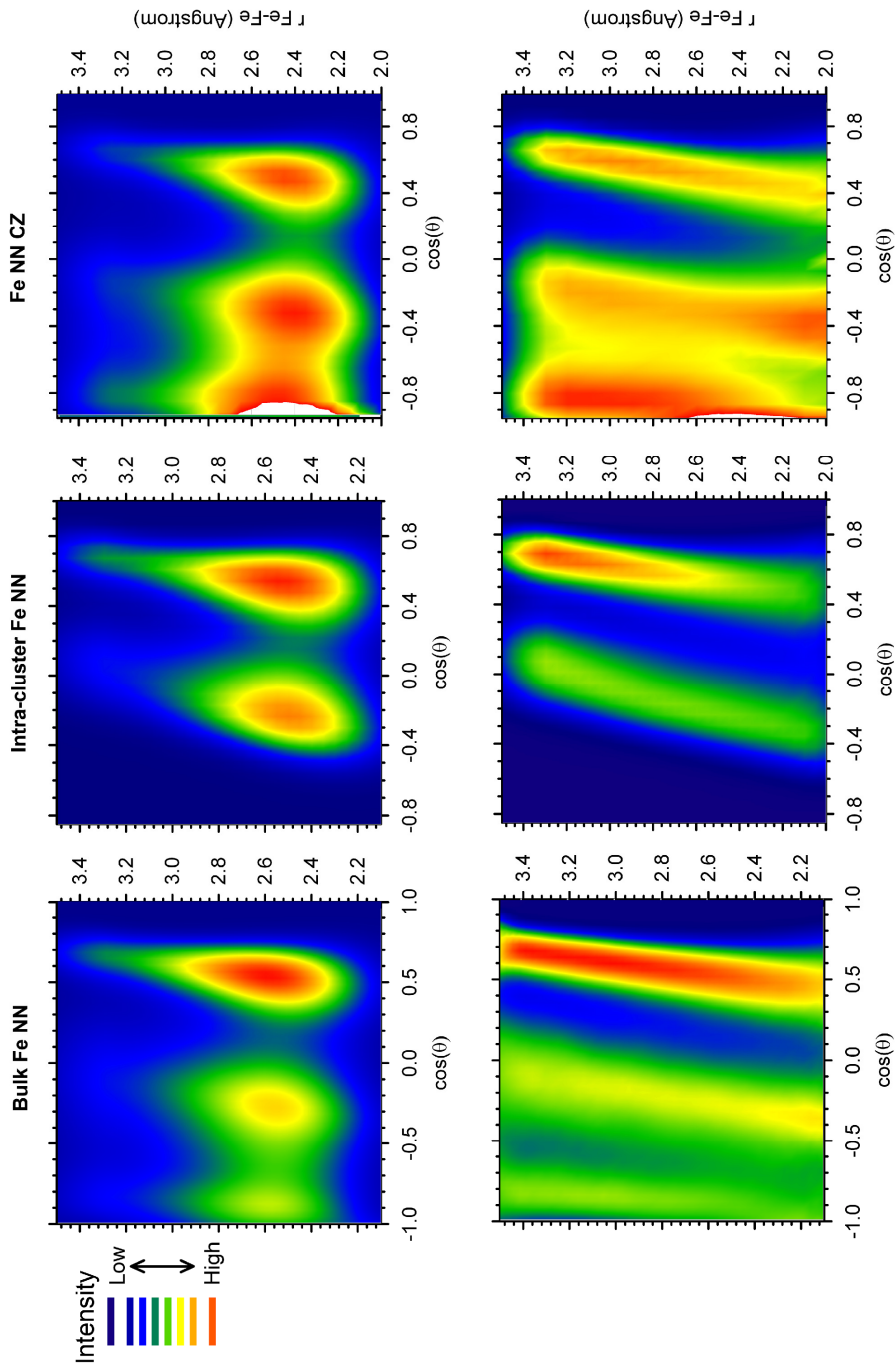


Figure 3.16 BLAH as a function of angle and distance are given. First row comprises of bulk Fe NN, intra-cluster Fe NN and Fe NN CZ BLAHs. Second row comprises of corresponding normalized surfaces. The surfaces are smoothed by a negative exponential function with sampling proportion of 0.01 and 50 intervals.

3.6.5. Pure Fe-Cluster Size Distribution

Presence of B-centered TP units resembling Fe_3B crystal symmetries combined with α° and η° alludes only an Fe-B compound forming tendency. There exists Fe-rich clusters, but presence of B in that case modifies their structure. The investigation of “nano-scale phase-separation” should be initiated by identifying pure Fe-clusters. What will be referred as an Fe-cluster is an aggregate formed solely by Fe atoms extending to several coordination shells, lacking any dissolved B. The resulting cluster dimension distribution is given in Figure 3.17a and displays very important structural features depending on composition. Two types of Fe-clusterings; thin Fe-contours (Figure 3.17b and Figure 3.17c) and Fe-clusters (Figure 3.17c) are found. First type of Fe aggregation is common to both $\text{Fe}_{83}\text{B}_{17}$ and $\text{Fe}_{80}\text{B}_{20}$, shapes of the distributions being same. The intensity difference is due to iron content. This type is a continuous contour formed by Fe atoms in the material with an average thickness of 0.72 ± 0.02 nm irrespective of composition, building boundaries between B-rich domains and illustrated in Figure 3.17b and Figure 3.18c. A second type of Fe-clustering evolved only in $\text{Fe}_{83}\text{B}_{17}$ above ~ 0.9 nm which perturbs form Fe-contours into B-rich domains (Figure 3.17c) and involves pure Fe aggregates of nearly spherical forms as shown in Figure 3.18a.

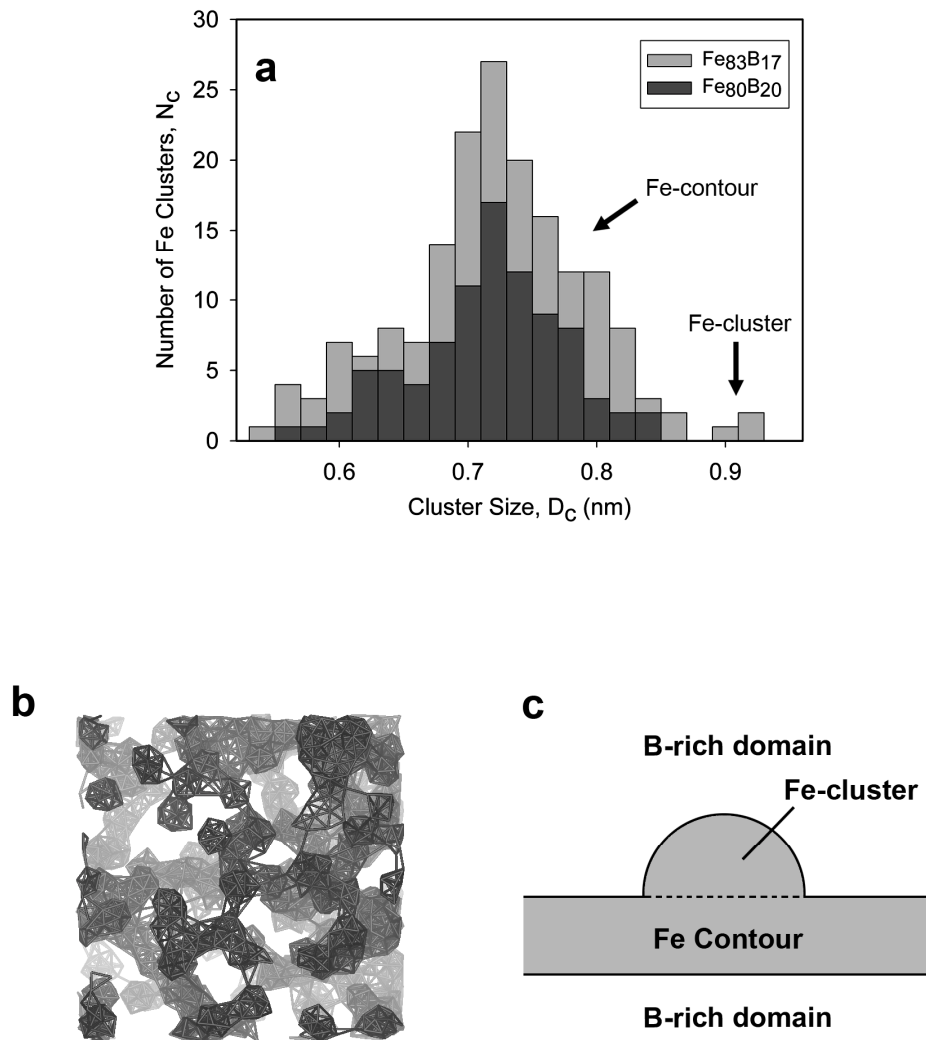


Figure 3.17 (a) Number of purely Fe clusters N_c vs. cluster size, D . Total number of such Fe-clusters in $\text{Fe}_{83}\text{B}_{17}$ is twice of that in $\text{Fe}_{80}\text{B}_{20}$. (b) The Fe-contours are illustrated for $\text{Fe}_{83}\text{B}_{17}$ with depth cueing; depth increases with brightness. (c) Schematic form of the Fe-contour, perturbing Fe-cluster and B-rich domains.

3.6.6. Connection Mechanisms

In a typical ~ 0.9 nm Fe-cluster surrounded partially by TPs in $\text{Fe}_{83}\text{B}_{17}$ is exhibited in Figure 3.18a. Presence of an icosahedral coordination in the Fe-cluster is clear. A central Fe-ico is surrounded by a second coordination shell, forming a dodecahedron-like cluster. As shown in Figure 3.18b the interconnections between Fe-clusters and TPs are established by face sharing. Icosahedra having triangular faces can interlock with surrounding B atoms. A dodecahedron also provides triangular faces but due to concavity of their arrangement, Fe atoms are disturbed to create triangular B-attachment sites. An additional mechanism unique to Fe-contours was observed in which ico gained several stellating atoms above 3-fold symmetry planes (Figure 3.18c) and turned partially into small triambic ico (Figure 3.18d). The formation reason of such stellations may be supplying 3 additional attachment planes for TPs by tetrahedron formation. Face-sharing of prismatic structures of TP with Fe-clusters or -contours averts interruption of non-crystallographic five-fold symmetrical arrangement through bulk of the material and promotes glassy structures.

3.6.7. Icosahedron-bcc Deformations

A perfect icosahedral cluster of smallest size has 13 atoms and addition or removal of several atoms distorts its shape. Purely Fe-clusters, having a maximum of ~ 1 nm size are expected to form d-ico clusters [93]. In such clusters, symmetries closer to ico (Figure 3.18a and Figure 3.18c) were also observed. Liquids of bcc-forming elements are reported to possess more icosahedral clustering upon supercooling and can supercool more prior to crystallization compared to fcc forming ones [55]. This can be elucidated by considering icosahedron-to-bcc/fcc transformations. An icosahedron can transform into an fcc structured cluster; *i.e.* cuboctahedron by a Mackay transformation [94]. In addition to this, fcc structure must be deformed that

the internal bct-Bain cell becomes bcc. Consequently, icosahedron-bcc transformation path may be more complex and allow more supercooling. Upon glass transition, entrapped polyhedra in supercooled melt cannot transform to bcc or remain as distorted ones in-between ico and bcc. Figure 3.19 illustrates a d-bcc structure encountered in a dominantly ico Fe-cluster in Figure 3.18a. The distortions bear traces of ico. Atoms marked as A and B above and below the cell are close to bcc-symmetry whereas the distortions of atoms marked as p resemble a 5-fold symmetrical plane of an ico, an atom being absent or not in exact position. $A \rightarrow A'$ and $B \rightarrow B'$ shifts construct parallel pentagons. By tracing back this route, the 5-fold symmetrical planes of an ico can be built up. The central Fe-atom in Figure 3.19 preserves a $\langle 0,4,4,2 \rangle$ coordination even after formation of pentagonal planes, until a nearly perfect ico of $\langle 0,0,12,0 \rangle$ is reached by capping these planes. The Wigner-Seitz cell of bcc; *i.e.* truncated dodecahedron is closely related to tetragonal dodecahedron ($\langle 0,4,4,0 \rangle$ and derivatives $\langle 0,3,6,1 \rangle$, $\langle 0,4,4,2 \rangle$, $\langle 0,4,4,1 \rangle$) especially under such ico-bcc deformations. Thus, these polyhedra being close to d-bcc structures are traces of incomplete Mackay and Bain transformations initiating from ico. It is concluded that these d-bcc polyhedra which are very resistant to altering their Voronoi indices, possess pentagonal symmetries. This can also explain why pentagonal angles dominate in BAD of Fe-Fe-Fe triplets (Figure 3.15).

Contributions to ico and bcc indices and Fe-Fe RDFs solely from pure Fe-clusters or contours are not much. Fe atoms belonging to the deformed TPs can also reflect bcc-like Voronoi indices, and contribute to bcc-like polyhedra intensities as well as ico intensities although they are considered to be bounded to B atoms. A distorted bcc-like arrangement can occur in CZs. In CZ, a capping atom, mostly shared by two or more prisms, turns into a central atom of bcc, creating a single bcc unit cell with surrounding Fe planes of neighboring borides. At the same time, both B and Fe atoms satisfy bcc translations of the central atom. These arrangements can extend over several bcc coordinations. More specifically, it was found that dominating d-bcc $\langle 0,3,6,4 \rangle$ and $\langle 0,2,8,4 \rangle$ are highly deviating from a statistical distribution of B

atoms. They are comprised of 91.9% and 91.3% Fe respectively. These can be treated as internally B-deficient zones; *i.e.* d-bcc-Fe (B) solid solutions, solubility limit of B being highly extended. A sample aggregate is given in Figure 3.20, and displays a bcc (111) plane arrangement. Here, since B atoms satisfy bcc translations, they behave more like substitutional solute atoms. It is not possible to identify all such zones accurately since they interpenetrate with other polyhedra around and have irregular shapes.

3.6.8. Ordering of B-centered TPs

In longer ranges disclosed as “simulation cell” in Figure 3.21, there exists no pattern followed by differently coordinated B-prisms. However, aggregations of highly coordinated ($CN \geq 9$) prisms in certain regions are observable. Therefore, there also exist certain regions with less dense packing of prismatic units. This fact brings about an inhomogeneity in distribution of CN of prisms in the ranges of MRO and becomes another evidence of phase separation tendency in nano-level. It has been shown in BAD and BLAH of CZ's (Figure 3.15 and Figure 3.16) that TP units can attain tetrahedral arrangements but they are not necessarily ico-type. Orderings of TPs are rather polytetrahedral, bearing ico-symmetries as well as pentagonal prism symmetries (Figure 3.21; polytetrahedra). Thus, NN prism orderings are invariably tetrahedral, forming occasionally pentagon forming alignments. Prisms are deformed in a way to promote cluster ordering. TPs attach each other in different ways; VS, ES and FS as also found in [54]. It was calculated for $Fe_{83}B_{17}$ that frequency of VS is 50.8 %, ES is 43.8% and FS is 5.4%. For $Fe_{80}B_{20}$ VS is 49.1%, ES is 44.1% and FS is 6.8%. In Figure 3.21; “cluster order” displays a local 5-fold symmetrical arrangement of TP units with corresponding connection modes. Atomic MRO in TM-M glasses can be predefined by SRO of TP units and these can be exploited to build a model in Section 3.6.10.

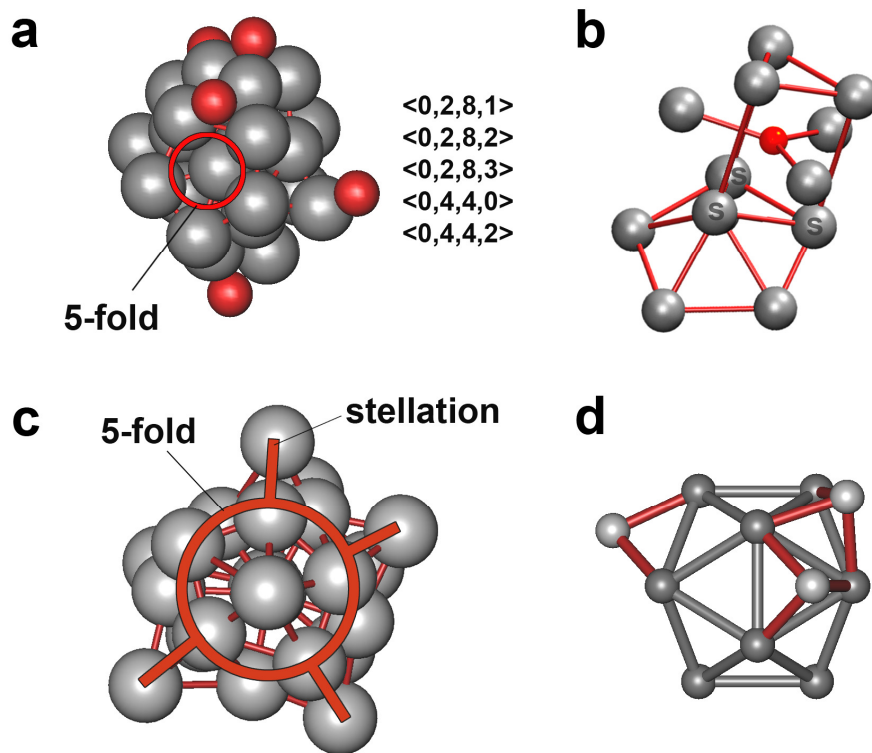


Figure 3.18 A 0.92 nm Fe-cluster (large atoms) of $\text{Fe}_{83}\text{B}_{17}$ with surrounding B atoms (small atoms) of TPs over triangular sites are shown in (a). Five-fold symmetry is marked with a solid circle. The Voronoi indices diffracted by atoms embedded in the cluster are noted. In (b) a typical triangular facet sharing (marked with *s*) of an Fe-cluster/contour with a TP is sketched. In (c), cross-section of a stellated Fe-contour directly from the simulation is given. Solid circle represents a 5-fold symmetrical plane and straight lines represent stellation directions. In (d) an atom deficient small-triambic icosahedron is sketched.

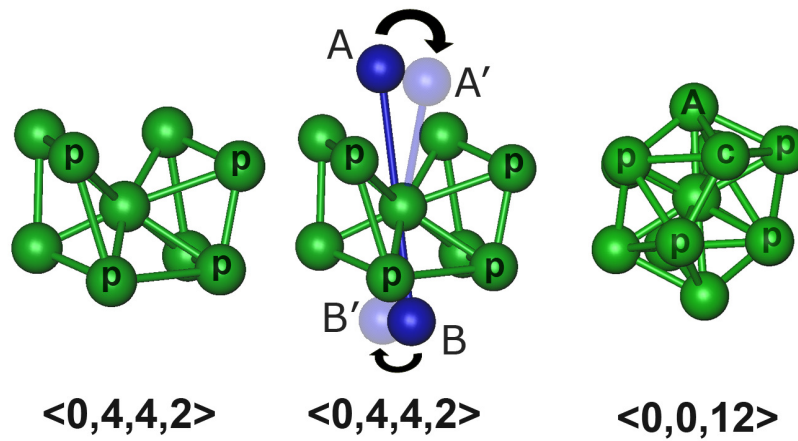


Figure 3.19 Distorted structures arising due to simultaneously progressing incomplete Mackay and Bain transformations of icosahedral clusters. The frontal pentagon is formed by four atoms marked as *p* and the *A* atom, and *c* denotes the capping atom.

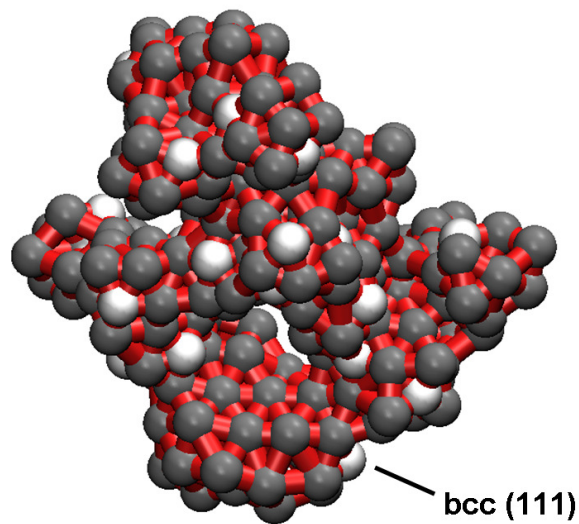


Figure 3.20 Bcc (111) plane extending through several atoms, formed in a $\langle 0,3,6,4 \rangle$ aggregate. Dark spheres and white spheres are Fe and B atoms respectively.

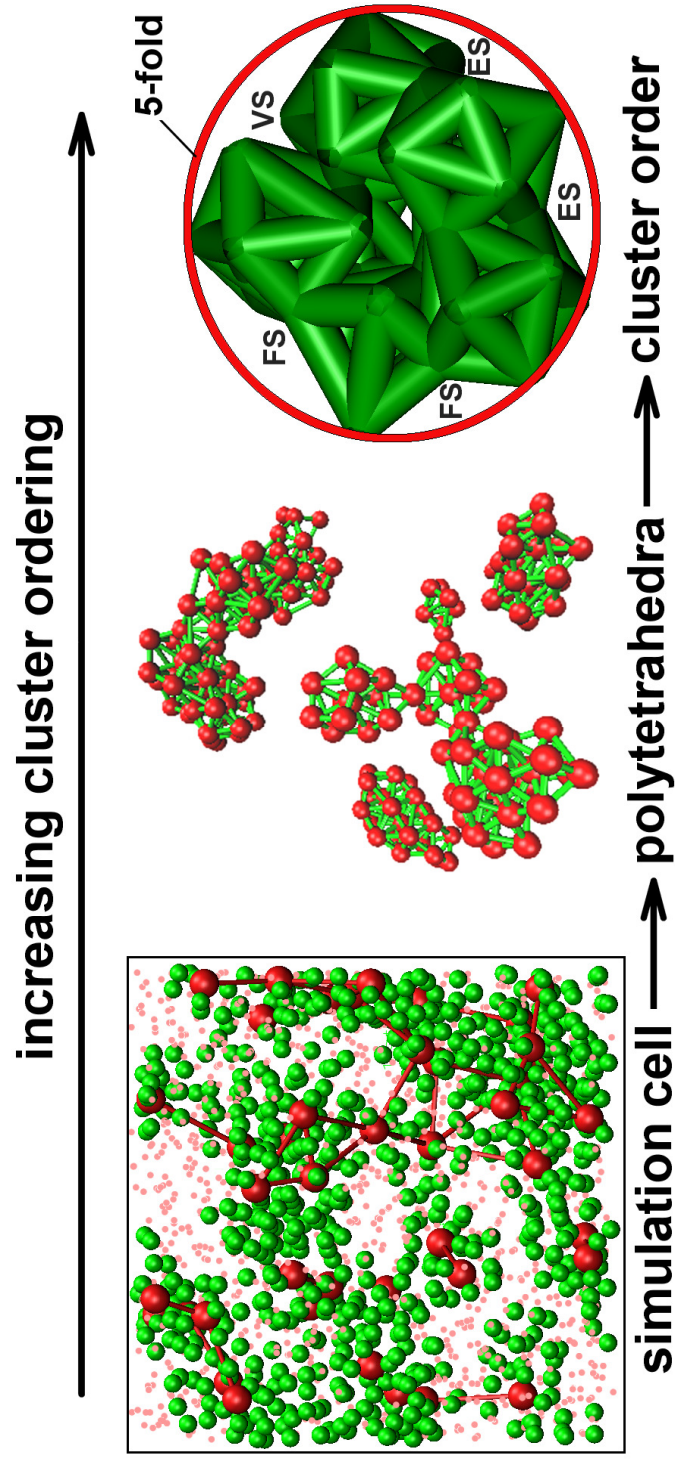


Figure 3.21 Left image is a snapshot of simulation cell where all points indicate B-centered prisms, largest spheres connected with lines are prisms having more than 10 neighbor prisms, coordination decreases with decreasing sphere size ($CN = 9$ for intermediate white spheres and $CN \leq 8$ for small gray spheres). Central image shows several polytetrahedral aggregates of B-prisms. Right sketch denotes an ico-like pentagonal lining of NN B-prisms and their connection modes (only Fe-Fe bonds are drawn for clarity).

3.6.9. Cluster-wise Decompositions of RDFs

The methodology applied during decompositions of Fe-Fe and Fe-B RDFs depends on the TP clusteral nature of these amorphous alloys. Clusters or NNs are defined being enclosed in first minimum of corresponding RDFs. While decomposing Fe-Fe RDF, radial search starts from Fe atoms in the cluster (NN and non-NN Fe atoms can be identified) and then extends to unshared Fe atoms of two neighboring clusters (possessing several maxima). As shown in Figure 3.22a, the intra-cluster coordinations of Fe-Fe pairs produce a two peak contribution, corresponding to the nearest neighbor peak and first sub-peak of the second peak of Fe-Fe RDF. As a result, these two arise mainly from trigonal prismatic local order of Fe-B clusters having two distinct Fe separations; a “touching” and a pentagon-diagonal one. When the range is extended to Fe’s in neighboring TPs (inter-cluster), additional overlapped peaks were found. To extract the unique inter-cluster correlations, the displacements between “unshared” Fe atoms are considered. The first peak of this inter-clusteral contribution makes up the second sub-peak of the splitted peak. Accordingly, the occurrence of such splitted peak in RDF of this type of metallic glasses is mainly due to internal structure of TPs, *i.e.* intra-cluster pentagonal linings and relative positionings of these B-clusters; *i.e.* cluster ordering.

Fe-B radial search starts from a “bounded” (B-Fe) pair in the cluster. Larger Fe-B separations are classified regarding the relative positions of Fe atoms to this Fe atom bounded to the B atom. Intra-cluster (B-Fe) pairs are nearly equidistant making up the first peak in Figure 3.22b. B atom being at the origin, when the searching range of Fe atoms is extended to first neighbors of the CZ Fe atoms (the path being (B-Fe)-Fe’), one ends up with the solid line in Fig Figure 3.22b which wholly covers the splitted peak. Non-NN of CZ Fe’s (the path being (B-Fe)-Fe’’) produces the upcoming peak. At first glance, the small non-linear shift of second and following peaks of Fe-B pairs relative to Fe-Fe pairs, to lower distances, arises since Fe-B first neighbor distance is smaller than that of Fe-Fe.

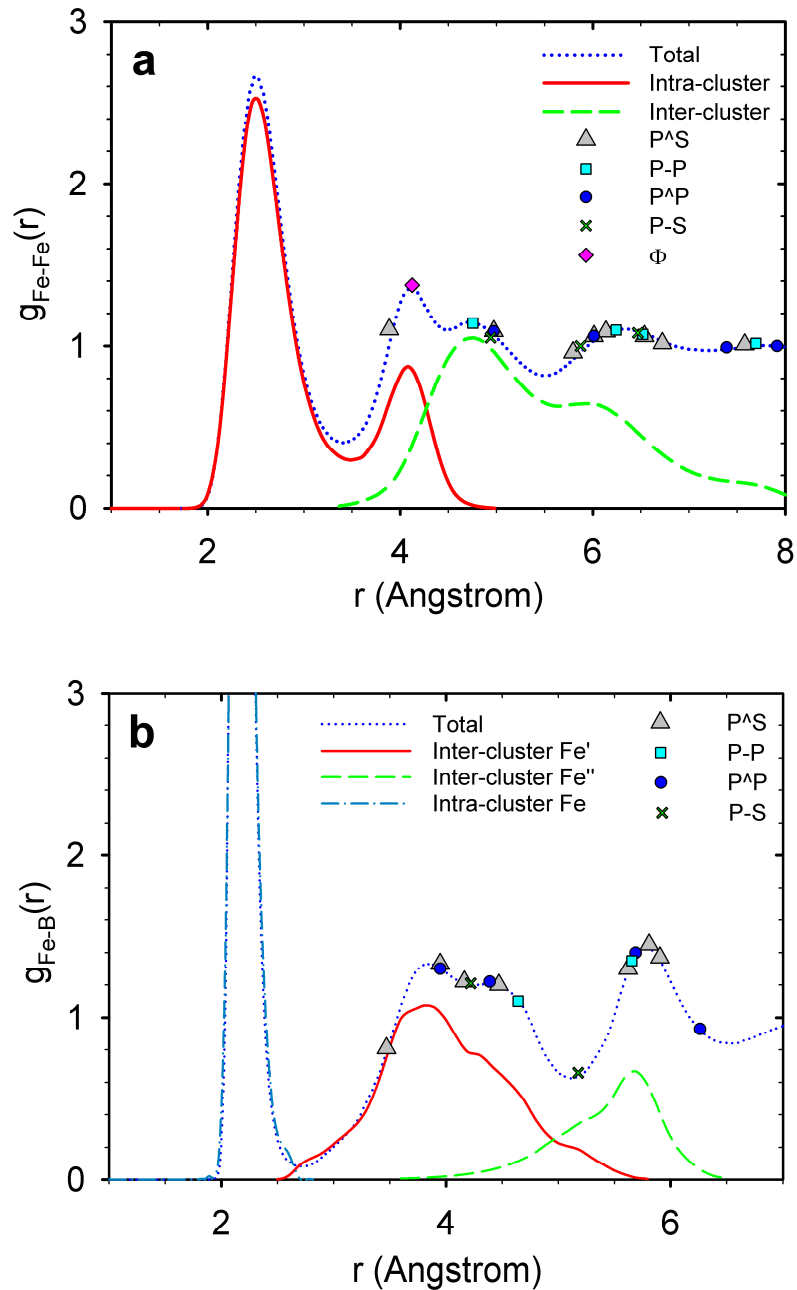


Figure 3.22 Cluster-wise decomposition of (a) Fe-Fe and (b) Fe-B RDFs. In (a) intra-cluster means Fe atoms bounded to the same B atom and inter-cluster means non-NN Fe atoms of two neighboring B-prisms. In (b) Inter-cluster Fe' denotes vector originating from a B atom, pointing NN Fe atoms of CZ Fe atoms whereas Fe'' pointing non-NN Fe atoms of CZ Fe atoms. The separations predicted by 2D-projection model are scattered on total RDFs.

3.6.10. Two-Dimensional Projection Model

Unlike the previously developed solute-solvent embodied random packing or quasi-crystal models (e.g. [38-45]), a more simplistic model will be introduced, specific to short and medium range order of TM-M glasses. Primarily, a pentagon with unit edge length has five diagonals of Φ , the golden ratio. Since previous analysis up to here proved the presence of pentagonal linings of Fe atoms (See Figure 3.23), a striking feature of this type of TM-M glasses trivially turns out to be that the ratio of the positions of first peak and first sub-peak of second peak in TM-TM RDF, equals to golden ratio; $\Phi = (1 + \sqrt{5})/2 \approx 1.618$. As a result, position of the first sub-peak of the splitted peak can be estimated for any of these glasses. The estimation error is less than $\pm 3\%$ for amorphous Fe-B, Fe-P, Ni-B, Ni-P and Pd-Si regarding findings in [46, 57], [47], [48], [49] and [50] respectively.

Unifying Voronoi polyhedra, BLAHs and cluster orderings, a simplistic 2D model can be contrived. A TP unit can possess up to 6 interpenetrating sets of nearly coplanar 5 Fe atoms forming a pentagonal ring and 3 such sets of nearly coplanar 4 Fe atoms on TP face forming a square ring (Figure 3.23; TP). Pentagonal angle of 108° is highly occurring (Figure 3.15) but a square tendency is low; *i.e.* right angles are linked to more stretched - less frequent Fe-Fe bonds (See Figure 3.16; Intra-cluster NN Fe). In average bond lengths, distortions make the right angles of TP faces split into a couple of slightly wider and narrower angles. When the cluster orderings are examined, every pair of neighboring clusters has nearly coplanar such rings initiating from the CZ. In CZs, four representative 2D-projected connection modes are determined (Figure 3.23). First two modes; two pentagons sharing an edge (P-P) and a pentagon sharing an edge with a square (P-S) are excessively encountered connection mechanisms. Other two modes P[^]P and P[^]S are tetrahedral CZ counterparts of edge sharing ones. When projected to 2-D, TP ES and FS can reproduce all four modes; P-P, P[^]P, P-S and P[^]S. TP VS sharing can be reproduced only the 60 degree point junctions; P[^]S and P[^]P. The idealized Fe-Fe separations in

these modes can summarize Fe-Fe MRO. MRO of B-Fe pairs can also be extracted from projections in Figure 3.23 calculating “C”-Fe separations. B atoms are slightly apart from the “C” of the pentagonal rings. The average error of depressing B atoms to pentagon centers is less than 1.0 %, in terms of $d_{\text{Fe-Fe}}$ and $d_{\text{Fe-B}}$. Such an error is larger (~17%) at the center of a square because B atoms are considerably apart from TP faces. Consequently, any vector $\mathbf{r}_{\text{B-Fe}}$ originating from center of a square are not included. The drawback of this model is that, error introduced due to 2D projection increases at larger distances. But it turned out to be sufficient considering MRO.

When the atomic displacements presented by these four modes are scaled with $d_{\text{Fe-Fe}}$ and scattered on the Fe-Fe and Fe-B RDFs, they represent short to medium range order satisfactorily (See Figure 3.22a and Figure 3.22b). All discrete atomic separations of the model accumulate near coordination shells. Even the ones which seem least accurate by falling in or near minima of total RDFs, are supported by their correspondence to flat maxima of decomposed RDFs both in Fe-Fe and Fe-B. The best correspondence with peak positions is acquired by P-P mode in Fe-Fe RDF. This estimates the second sub-peak distance in Fe-Fe RDF as the distance between unshared atoms, forming an angle of 144° with a shared atom (scaling factor is $\sqrt{\Phi + 2}$). This also explains the peak near 150° in BAD of Fe-Fe-Fe (Figure 3.15) which was shown to be a CZ feature (Figure 3.16; Fe NN CZ). The slight shifting might be due to other modes diffracting wider angles like 162° and 168° for equal pairs, due to 2D projection and/or distortions in polyhedra. Since identified by modes P[^]P and P[^]S (See Figure 3.22b), the split in second peak in B-Fe RDF is solely due to tetrahedral TP ordering and following peaks are related to mixture of all modes.

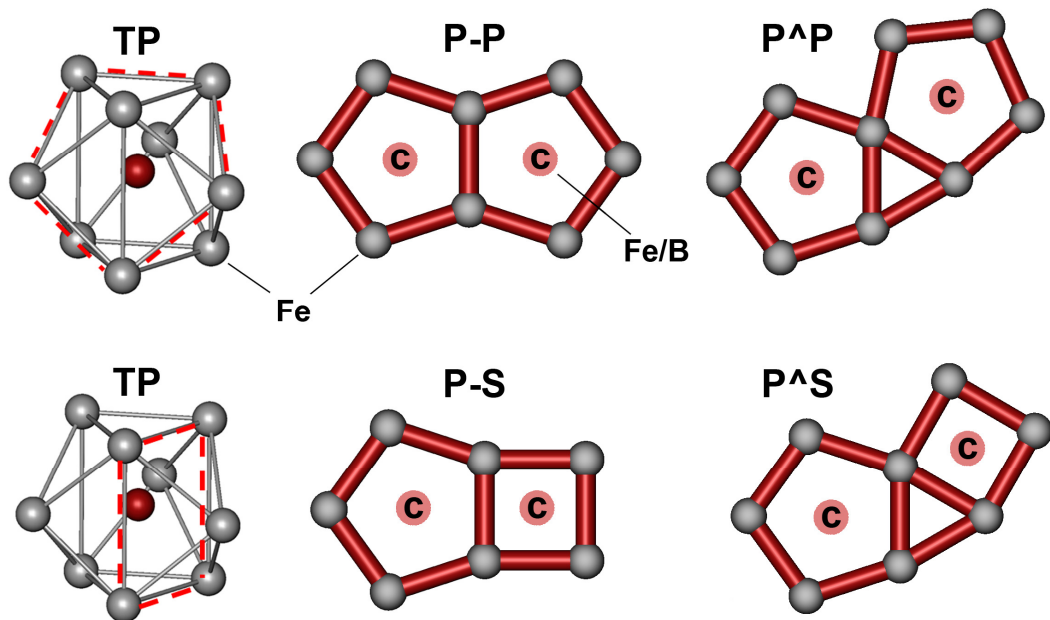


Figure 3.23 Nearly co-planar 5 Fe atoms and nearly co-planar 4 Fe atoms (spheres at corners) in a schematic B-centered (dark spheres) TP unit with three capping atoms ($\langle 0,3,6,0 \rangle$), forming a pentagonal ring and a square ring respectively are marked with dashed lines. Numbers of rings can vary depending on TP type. P-P, P[^]P, P-S and P[^]S modes are sketched. All spheres at the corners are Fe atoms. Spheres marked as “C” are Fe or B atoms above or below idealized planes.

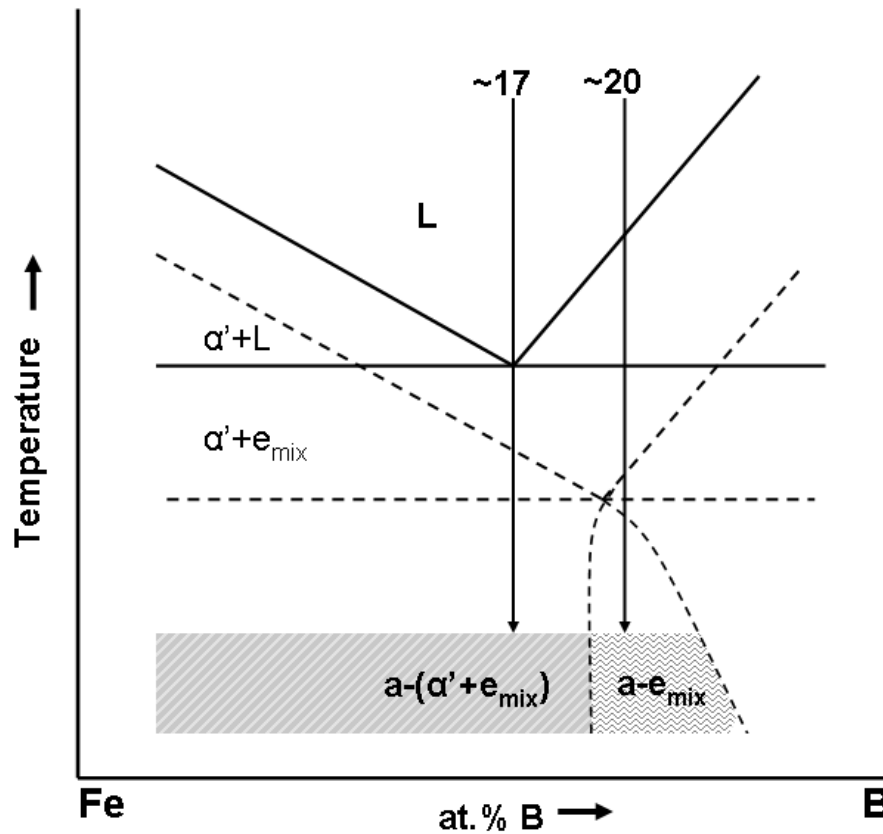


Figure 3.24 An arbitrary sketch of near eutectic region of Fe-B binary phase diagram. The solid lines, dashed lines, α' , e_{mix} and “a” represent, equilibrium cooling, non-equilibrium cooling, primary α -Fe, eutectic mixture and amorphous phase respectively. The crossed and zigzagged regions represent room temperature structures resembling hypo-eutectic and eutectic regions after rapid solidification (metallic glass formation).

3.6.11. Pseudo-Eutectic Mixture and Nanoscale Phase Separation

The eutectic point close to Fe rich part lies around 17 at.% B in the equilibrium phase diagram of Fe-B binary system, which is sketched by the solid curves in Figure 3.24 (See Appendix A, Figure A. 1 for equilibrium phase diagram of Fe-B system). When cooling rate is increased, the eutectic reaction shifts to lower temperatures and higher B concentrations, shown by the dashed curves in Figure 3.24. When solidified more rapidly, near-eutectic Fe-B melts quench into the glassy state. However, as shown before, this glassy state resembles the phases that make up the eutectic mixture, but shows macroscopically no trace of phase separation.

The phase separation occurs in nanoscale. The propagation of a pure and thin Fe-contour of ~ 0.72 nm thickness separating B-rich domains of deformed-bcc resembles a eutectic mixture which could not nucleate. Moreover, both of these deformed regions resemble their crystalline counterparts. The 5-fold symmetry of Fe-contour supports that if this size of an Fe-cluster is to evolve in the melt, it would be icosahedral (or alike 5-fold symmetry clusters). Surrounded by these contours is the B-containing domains of a variety of structures discussed previously, making up an amorphous *pseudo*-eutectic mixture ($a-e_{\text{mix}}$) with the Fe-contours.

Up to here, there is evidence that the so-called suppressed nucleation did not avoid a eutectic-like phase separation in the atomic scale. A more satisfying trace emerges when composition of the alloy is altered slightly. When Fe content is increased from 80 to 83 at.%, it was found that pure α' -Fe-perturbations (with no dissolved B) from these contours occur in spherical forms with diameters around ~ 0.9 nm directly into the B-rich domains. These greatly imitate the primary phase of the eutectic reaction and are comprised of excess iron atoms which can be accommodated by neither of the components of $a-e_{\text{mix}}$. This phenomenon of nanoscale phase separation is sketched in Figure 3.24. This is very surprising since even with such high cooling rates that can allow high solubilities, a phase boundary may exist between $a-e_{\text{mix}}$

and $a-(\alpha'+e_{\text{mix}})$, exact position of which cannot be known, but presence of which shall be proposed.

3.6.12. Pre-crystallization of Amorphous Fe-B

The first nucleation product of amorphous-Fe-B alloys is α -Fe. However, although glassy state is always less stable than crystalline ground state, initiating any crystal nucleation in the amorphous matrix is not probable in practical time scales without introducing a seeding crystal cluster into the matrix during simulation. Accordingly, it is of particular interest whether the Fe-Fe pair potential in the Fe-B system can stabilize bcc structure solely. Interacting in the current Fe-Fe field, the potential was capable of stabilizing the bcc structure at 10 K up to melting of the crystal. In Figure 3.25, evolution of bond angle distribution functions with temperature are sketched. At 10 K, bond angles are strictly confined to first coordination sphere of bcc structure. With increasing temperature, the first two coordination spheres unite (Figure 3.26) and become indistinguishable. As a result three additional peaks arise in Figure 3.25. Crystal melts at a relatively low temperature around 800 K due to softness of the potential. In summary, if an Fe crystal were to nucleate in the matrix, it would definitely be bcc-Fe, validating the versatility of the interaction fields employed. Since Fe-Fe pair potential in Fe-B system strictly stabilizes bcc crystal structure, the presence nanoscale phase-separated structure bearing proposed deformed-bcc domains becomes discussable. The deformation results from remaining inter-prismatic Fe-domains being under strong interaction field of Fe-B.

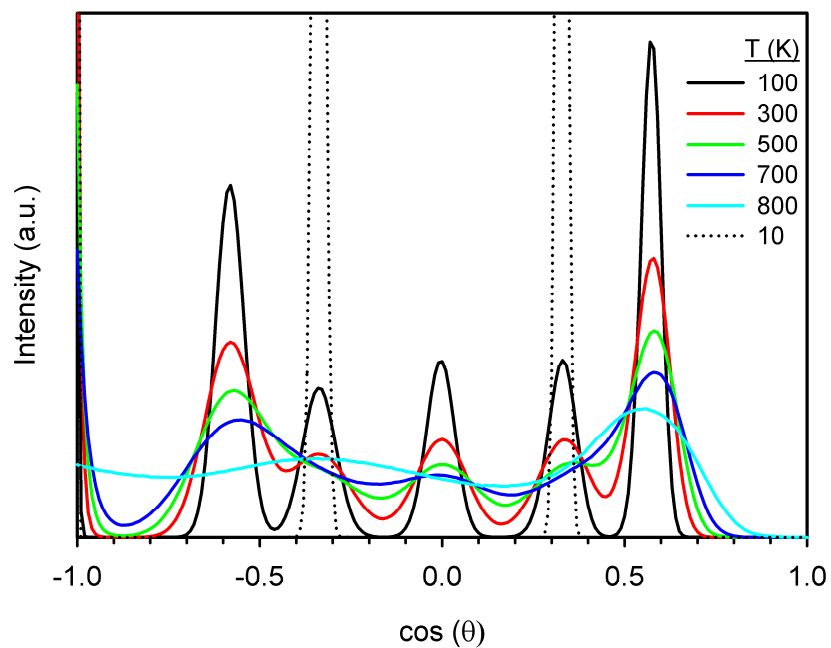


Figure 3.25 Variation of BAD in crystalline bcc-Fe from 10 K to melting.

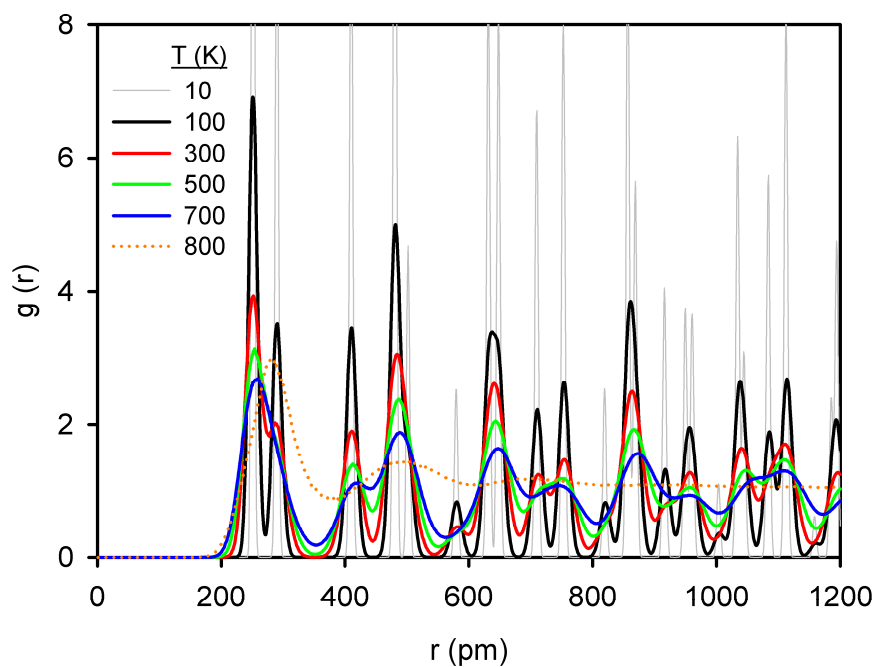


Figure 3.26 Variation of RDF in crystalline bcc-Fe from 10 K to melting.

CHAPTER 4

PRODUCTION, DEVELOPMENT AND PROPERTIES OF IRON-BORON BASED BULK METALLIC GLASSES

4.1. Introduction

A question like, “Why investigate the Fe-B binary, if the experimental interest is to produce BMGs with more than three kinds of atoms?” may arise. The answer is three-fold;

- First of all, theoretically investigating a system with three or more kinds of atoms with MD or MC simulations is computationally not practical.
- Secondly, although today a variety of BMGs can be produced, even the binary metallic glasses, their topology and subsequent glass formation have not been clearly understood yet. BMG alloys are still designed considering empirical rules (See Section 2.3), empirical criteria, trial/error routes and even by guess of an experienced scientist. Consequently, the origins of glass formation, before BMGs, lie beneath binary systems, as Fe-B systems in this case.
- Lastly, structural units are expected to be the same in binary metallic glasses and BMGs. Even the compositions are broadly the same like; high amount of TM accompanied by lower amount of M.

The last observation is actually the starting point of developing any TM-M based BMG. The mother alloy is always chosen as a validated, glass forming TM-M binary and further alloying additions cause no drastic change in TM/M balance which otherwise leads to failure in improving GFA generally. For example, rather than $\text{Fe}_{80}\text{B}_{20}$ the alloys can now be considered as $(\text{Fe}_a\text{TM}_b)_{80-x}(\text{B}_c\text{M}_d)_{20+x}$ where a, b, c, d and x denote deviations from mother composition.

In the previous chapter, the structure of TM-M glasses were investigated and discussed in Fe-B binary system. However, today, there is a demand (especially commercially) of metallic glasses which can be cast into bulk forms in desired shapes, and it is currently not possible to obtain bulk metallic glasses (BMGs) in binary Fe-B or any binary TM-M system. Consequently, in the light of the findings in the previous chapter, experimental metallic glass (more specifically, BMG) production should not be confined to Fe-B binary, and more alloying elements should be added. Moreover, the BMG production procedure employed in this study is totally conventional and commercially promising, and those BMGs that are produced are converted into Bulk Nanocrystalline Alloys (BNCAs) which are rarely available via such direct production methods. The spatial atomic relations of BNCAs and precursor BMGs are studied in terms of the developed MRO in the glassy state and corresponding precipitated nanocrystals.

4.2. Background

4.2.1. Glass Forming Ability of Current BMG Alloys

Formation of glass requires suppression of the crystallization by avoiding the formation and growth of crystal nuclei during cooling from melt, bypassing the T_m , until the glass transition temperature T_g is reached. At T_g a second-order diffuse phase transition takes place by freezing the densely packed random atomic structure

of the supercooled liquid (See Sections 0 and 2.2). So stabilizing the liquid and increasing its resistance against stable crystalline phases is the primary concern of glass forming. Several parameters like reduced glass transition, $T_{rg}=T_g/T_m$, supercooled liquid region, $\Delta T_x=T_x-T_g$, atomic size ratio and electronegativity ratio are proposed (See Section 2.3), but none of them have been completely successful in predicting GFA of all systems [95]. In Figure 4.1, Inoue classified several types of glasses with respect to their R_c (critical cooling rate), d_{max} (maximum rod diameter), and T_{rg} . It can be depicted that with the aid of experimental progress in development of new BMGs, there are several of them with R_c values very close to oxide glasses and maximum diameters even above 100 mm. Moreover, it can be seen that there is a roughly linear correlation present between T_{rg} and R_c (or d_{max}) values of BMG alloys.

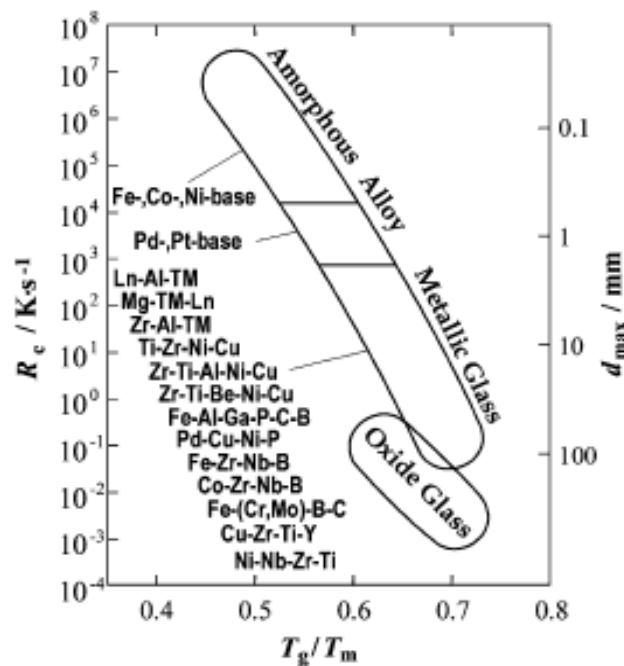


Figure 4.1 Relationship among the critical cooling rate, R_c , for glass formation, maximum thickness and reduced glass transition temperature [96].

4.2.2. Bulk Amorphous Soft Magnets

In 1995, Inoue et. al. reported the first bulk metallic ferromagnetic Fe-based alloy of Fe–Ga–Al–P–B–C multicomponent system [97] and many Fe-B based BMGs have been developed since then which could mainly be grouped as Fe-(Zr, Hf, Nb)-(Mo, W)-B [98], Fe-(Cr, Mo)-Ga-P-(C, B) [99] and (Fe,Co)-Nb-(B, Si) [100, 101]. Typical alloys developed in Fe-(Al,Ga)-(P,B,C,Si) BMG system are $Fe_{72}Al_5Ga_2P_{11}C_6B_4$, $Fe_{72}Al_5Ge_2P_{11}C_6B_4$, $Fe_{72}Al_5Ga_2P_{10}C_6B_4Si_1$ and $Fe_{70}Nb_2Al_5Ga_2P_{11}C_6B_4$ and this alloy system is worth to be reviewed since it pioneers the Fe-B based BMGs. These Fe-based alloys have R_c as low as 10 K/s and ΔT_x of ~60 K which reflects the effectiveness of metal and metalloid elements added to Fe-Si-B and Fe-P-C alloys (first reported ferromagnetic metallic glass [5]). Nb, Cr, or Mo additions can further increase the ΔT_x to 65 K. B_s of 1.1 - 1.3 T, μ_e of 7000-12000 at 1 kHz and H_c of 2-6 Am⁻¹ can be considered as good soft magnetic properties of these alloys. Inoue also showed that substitution of Si with P or C rather than Fe improves saturation magnetization [96]. $Fe_{72}Al_5Ga_2P_{11}C_6B_4$ and $Fe_{72}Al_4Ga_2P_{11}C_6B_4Si_1$ having high thermal stability of supercooled liquid, improved soft magnetic properties and higher T_c , are decided by Inoue as copper mold castable into 1-3mm cylinders and they found that diameters up to 2 mm are possible with good soft magnetic properties similar to ribbons [96].

Pawlik et. al. investigated and compared glass forming abilities and magnetic properties of Fe-Al-Ga-P-B-Si and Fe-Al-Ga-P-B-C produced by both melt-spinning and suction die casting integrated to an arc melting unit to reveal the effect of production method also [102]. They found for $Fe_{76-x}Al_4P_{12}Ga_xB_4Si_4$ and $Fe_{75-x}Al_5P_{11}Ga_xB_4C_5$ (where $x = 0, 2, 5$) that, $x = 2$ at.% and $x = 0$ at.% resulted in the thickest amorphous ribbons respectively. For the suction cast rods, the former showed the best result at $x = 5$ at.% and the latter at 0 at.% again with X-ray analysis of the samples. Finding more amorphous phase in $Fe_{75}Al_5P_{11}B_4C_5$ with both methods revealed the fact that it is a better glass former. They also mentioned that this composition having the largest glass forming ability has the smallest ΔT_x of 53

K and GFA of the alloys are smaller than previously reported in [97, 103]. Consequently, as mentioned in Section 2.3, although referred in almost every experimental study, empirical parameters are not always dependable. It was interestingly reported that although H_c is low (6-11 A/m) for fully amorphous ribbons, it is much lower (2-3 A/m) for amorphous-crystalline thicker samples with co-existence of anisotropy fields. However, susceptibility of thicker ribbons was lower.

K. Pekała and co-workers relied on the GFA of such alloys and with addition of 1 at.% Cu, produced bulk nanocrystalline $Fe_{74}Al_4Ga_2P_{11}B_4Si_4Cu_1$ [104]. In addition to improving GFA, Cu atoms going out of solution early, provide conventional nucleation sites for nanocrystallization. They found crystallization to be consisting of three stages 725, 810, 860 K, the first period being suitable for nanocrystallization. Annealing at 720 K produced 6-11 nm diameter bcc-Fe crystals with a slightly higher lattice parameter than pure Fe. This is because of Si being in solution in Fe. Following the secondary and tertiary crystallization temperatures, Fe_3P and Fe_3Si , and Fe_2B precipitated respectively. Saturation magnetization increased from 0.9 T to 1.4 T by nanocrystallization in first interval. Moreover, coercive force, H_c dropped significantly from 14 to 1.8 A/m. This softening affect is due to the grain sizes being smaller than ferromagnetic exchange length. Best annealing was the one mentioned at 720 K, higher temperatures resulting in much higher H_c and lower B_s with bcc-Fe(Si) nanocrystals. Precipitation of neither the mentioned phases nor FeSi has desirable effects on soft magnetic properties. The fraction of nanocrystalline phase were calculated from $X(T)=M(T)/M(T)_{FeSi(6\%)}$ where $M(T)_{FeSi(6\%)}$ is known as 164 Am²/kg and $M(T)$ is obtained from experiments. This alloy as well as all nanocrystalline alloys exhibit high resistivity due to very high electron scattering at grain boundaries, resulting in very small eddy current losses required for high frequency applications.

Koshiba et al. reported another type of BMG, $Fe_{56}Co_7Ni_7Zr_2Nb_8B_{20}$ and $Fe_{56}Co_7Ni_7Zr_2Ta_8B_{20}$ with a wide ΔT_x of 60 K [105]. Moreover, Inoue et al.

reported that $\text{Fe}_{56}\text{Co}_7\text{Ni}_7\text{Zr}_8\text{Nb}_2\text{B}_{20}$ has an enormous ΔT_x of 85 K with possibility of much larger bulk casts [106].

The only ternary Fe-based BMG reported is in Fe-Y-B system and had a composition of $\text{Fe}_{72}\text{Y}_6\text{B}_{22}$ [107] with 2 mm rod diameter and 1.56 T saturation magnetization. The alloy seemed promising due to simplicity of its composition and very attracting magnetic properties. The authors discovered it after trying a great number of rare-earth and lanthanide group elements as a ternary constituent added to Fe-B system. The coercivity was around 40 A/m and electrical resistivity was over 200 $\mu\Omega$ cm. This alloy was first in Fe-based BMG systems to involve Y as a main constituent and tried to be produced as shown in Section 4.5.1.

After introduction of Fe-Nb-B-Si BMG system [100], with the optimum composition of $(\text{Fe}_{0.75}\text{B}_{0.15}\text{Si}_{0.1})_{96}\text{Nb}_4$, via Co, Ni, Y or Cu modifications, GFA of the alloy has been improved greatly with no significant loss in magnetic properties. The system is basically of the Finemet-type, alloys of which also show nanocrystallization capabilities. The pioneering $(\text{Fe}_{0.75}\text{B}_{0.15}\text{Si}_{0.1})_{96}\text{Nb}_4$ with 1.5 mm thickness had a ΔT_x of 50 K, T_{rg} of 0.61, B_s of 1.4 T, H_c of 3.7 A/m and permeability of 14400. The best glass forming Co added alloy, $\text{Fe}_{36}\text{Co}_{36}\text{B}_{19.2}\text{Si}_{4.8}\text{Nb}_4$ was able to be cast into 5 mm diameter rods and showed a ΔT_x of 50 K, T_{rg} of 0.587, B_s of 0.84 T, H_c of 1.5 A/m and permeability of 25000 [101]. This alloy was selected to be cast and is investigated in Section 4.5.2.

4.2.3. Nanocrystalline Alloys from Amorphous Precursors

Nanocrystalline soft magnetic alloys attracted many scientists due to their ability of optimizing magnetic properties with the aid of chemical and structural adjustments and diversity between properties of nanometer-sized structures and macroscopic ones. Primarily, Fe or Co with around 20 at.% B is used as the base material in amorphous alloys and nanocrystal precursors for soft magnetic applications. The

remaining composition should be adjusted according to the GFA and crystallization parameters. By a proper annealing, nanocrystals of 10-50 nm α -Fe, α -FeSi, α - or α' -FeCo, surrounded by a TL-TE-B-Cu intergranular amorphous phase (TL and TE denote late and early transition metals), can be obtained between the primary and secondary crystallization temperatures.

Nanocrystalline and amorphous Fe-based alloys have been developed and found significant uses especially in applications of low and high frequency transformers, inductors, motors and electrical energy managements. These applications mostly exploit the good soft magnetic properties that indicate high permeability, low hysteresis loss, large saturation and low remnant magnetizations, and high Curie temperature. Several successful commercial alloys like Finemet (Fe-Si-B-Nb-Cu), Nanoperm (Fe-M-B-Cu, M = Zr, Nb, Hf) and Hitperm (Fe/Co-M-B-Cu, M = Nb, Hf, Zr) have evolved in ribbon forms.

4.2.3.1. Finemet Ribbons

Finemet type ribbons are of great importance since the most established and commercially most attractive alloys are of this kind. Moreover, the nanocrystallization capability of amorphous-Finemets seem promising for producing bulk nanocrystalline alloys which cannot be produced with a conventional method like heat treatment of amorphous precursor. Actually, the Fe-Co-Nb-B-Si BMG's studied experimentally in this study belong to Finemet type alloys with Hitperm type modifications, the only difference being a good compositional adjustment to improve GFA.

Finemet is the patented trade name of nanocrystalline Fe-Si-B-Nb-Cu alloys discovered in late 1980's by Yoshizawa et al. [108, 109]. After quenching the melt into an amorphous state, nanocrystallization is generally carried out in an argon atmosphere furnace. In these alloys, nanocrystalline phases consist of α -Fe with

some Si dissolved-in and FeSi (of DO₃ structure). Depending on the crystallization parameters, these are surrounded by an intergranular amorphous phase with a lower Fe content.

A typical composition of Finemet is like Fe_{73.5}Cu₁Nb₃(Si_xB_{1-x})_{22.5}, (0.5 ≤ x ≤ 0.8), with saturation magnetizations around 1.0-1.2 T and Curie temperatures generally lower than 1050 K. Although 5-10 at.% B can be substituted for Si, generally it is 9 at.% due to good soft magnetic properties. Addition of B worsens the magnetic properties and precipitation of Fe₂B with second crystallization temperature introduces hard magnetism [110]. Noh et al. found that with this substitution, a B-rich ferromagnetic phase forms at the interfaces, in addition to magnetic α-Fe(Si) nanocrystals [111]. They also investigated the effect of Nb and Cu added solely and effect of both added at the same time on the crystallization kinetics of Finemet alloy [112]. Atomistically, it was shown that Cu goes out of solution before crystallization, forms Cu-rich bcc crystals of ~5 nm and serves as heterogeneous nucleation sites for α-Fe(Si) with very little Cu and Nb dissolved in. Nb is known to diffuse slowly and allow microstructural control of the alloy by avoiding the grain growth.

Zbroszczyk and co-workers studied the effect of 7 at.% Co substitution for Fe and observed that Co improves magnetic properties and enhances nanocrystallization [113]. They also found that Co increases the initial susceptibility. However, Yoshizawa et al. reported that Co additions up to 40% increase coercivity in Fe_{79.4-x}Co_xNb_{2.6}Si₉B₉ [114]. Because, Co lowers the driving force of clustering of copper and decreases number of Cu nucleation sites, grain size increases. Recently, Chau et al. looked for the results of substituting Au for Cu. The alloy exhibited ultrasoft magnetic properties [115] and a very high magnetic entropy change of 7.8 J/kgK. Au is believed to act like Cu and form heterogeneous nucleation sites. However, with much higher diffusion rate, it lowers the crystallization barrier *E* from 3.25 eV to 2.8 eV. The measured grain size by Scherrer expression is 10.8-11.6 nm, which is much lower than 35 nm, the ferromagnetic exchange length of Finemet, leading to

soft magnetism. They conducted annealings at 530 °C for 30, 60 and 90 min., the last one yielding the best soft magnetic properties.

4.2.3.2. Nanoperm Ribbons

Suzuki et al. reported a nanocrystalline soft magnetic alloy of B_s over 1.5 T, μ_e around 16×10^4 (at 1 kHz) and zero magnetostriction in 1991 [116]. The alloys were melt-spun ribbons of Fe-M-B with M=Zr, Hf or Nb. Later, many substitutions for M and addition of other alloying elements to promote GFA and nanocrystallization are reported in literature. A typical composition of Nanoperm is like $Fe_{88}Zr_7B_4Cu_1$ with an α -Fe(bcc) nanocrystals, B_s of 1.5-1.8 T and T_c around 770 °C.

4.2.3.3. Hitperm Ribbons

Fe and Co is known to produce the best ferromagnetic properties with generally 50% addition of each element [117]. The typical $Fe_{44}Co_{44}Zr_7Cu_1B_4$ nanocrystalline alloy with α' -FeCo nanocrystal phase reported by Willard et al., is actually superior to those alloys mentioned previously [118]. Their B_s is around 2.0 T and permeabilities are not smaller. However, the main advantage of Hitperm alloys is their ability of working and resisting corrosion at elevated temperatures, above 900°C. Nb and Hf can be substituted for Zr and many studies are available about this in literature.

4.3. Alloy Design

Optimizing magnetic properties of an amorphous alloy contradicts with the fact that alloying additions that favor glass formation generally deteriorate magnetic properties significantly. This necessitates a well-established procedure:

- a. Maximizing the intrinsic magnetic properties by appropriate chemistry; alloy should be based on Fe (and/or Co).
- b. Conducting Reverse Monte Carlo, and Monte Carlo statistical thermodynamics simulations via pseudopotential theory. Conducting experiments according to currently in-use alloys, develop them and identify the phenomenon of GFA.
- c. Maximizing the extrinsic magnetic properties by microstructure adjustment.
- d. Characterization of the final product with XRD, SEM, DSC and VSM (See Section 4.4.2).

4.4. Experimental Methods

The current experimental procedure for casting BMGs in Novel Alloys Design and Development Laboratory (NOVALAB) follows a completely conventional route. After arc-melting (of which there is also industrial types available) the alloys, the actual rapid solidification is conducted in a centrifugal casting (CC) equipment. Opposite to experimental techniques reported, CC is an industry friendly method which is actively used in dentistry and jewellery productions. Consequently, if current route can be well-established in production of BMGs, it would allow commercialization of the alloys and mass production. The conventionality starts with employing alumina crucibles, which would at first glance seem like a detrimental casting element since GFA is destroyed by introduction of oxygen to melt. However, alumina is a cheap raw material which is readily available and currently NOVALAB produces her own alumina crucibles with an established route. The remedy for reaction of melt with the crucible is avoided by coating the interior of the crucibles by boron-nitride or yttria. The following casting into pre-cooled copper moulds of any desired shape allows a rapid casting of the BMG proper for mass productions thus is very promising.

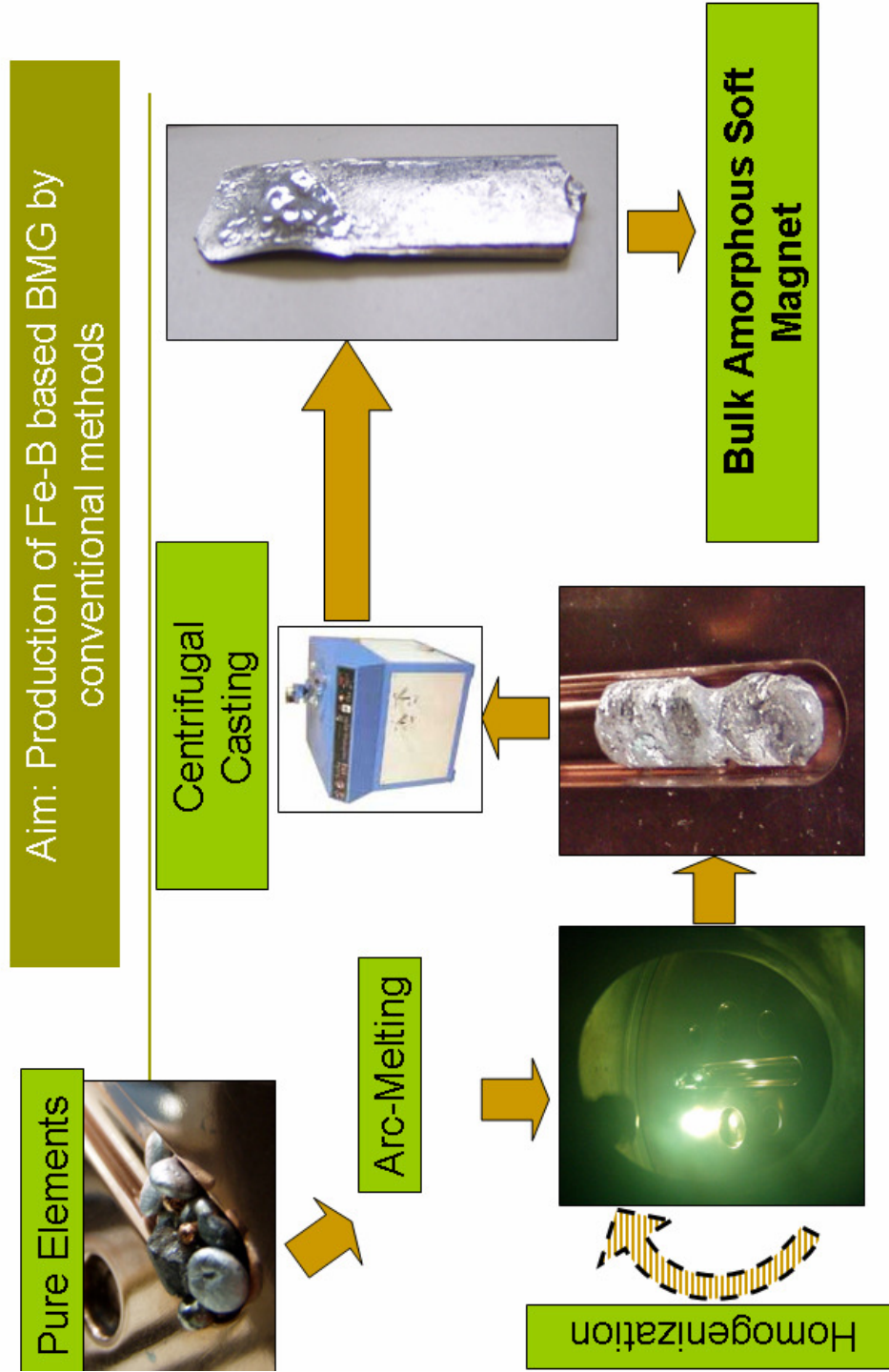


Figure 4.2 Preparation route of the bulk amorphous alloys produced in NOVALAB.

4.4.1. Preparation of the Alloys

The preparation route of BMGs is as follows; homogenization in arc-melting and rapid solidification in centrifugal casting into pre-cooled copper moulds as sketched in Figure 4.2. The precision of the composition and amount of the impurities introduced to the produced alloy are decisive in metallic glasses and especially in bulk metallic glasses. Consequently, the constituent elements of the alloys are weighed without any hand contact up to fourth decimal place precision. Alloys are all cast from elemental and scientific-grade materials and the purity grades are listed in Table 4.1. Any alloy composition reported follows the convention of *nominal* compositions mentioned.

Table 4.1 Purity grades of alloying elements used for alloy preparation. All elements are supplied from Alfa Aesar.

Element	Grade (%)
Fe	99.97
Co	99.9
Nb	99.6
B	99.5
Si	98.5
Cu	99.9
Y	99.9

4.4.1.1. Homogenization

The alloys especially with more than two components must be homogenized prior to rapid solidification, which is carried out by Edmund Bühler GmbH Arc Melter AM device. The Arc Melter has multi-purpose button and groove crucibles in a copper plate with highly reliable, hydraulic heavy-duty hoist. By contactless high-voltage, high-frequency arc ignition is done through a motor driven, water-cooled tungsten electrode which can be moved freely above the crucibles. The vacuum chamber is water-cooled and double-walled with two windows allowing an excellent observation of the experiment. Melting can be conducted on alloys of maximum 500 g weight up to 4000°C temperature. The vacuum is supplied by Varian rotary (DS-102) and diffusion (HS-2) pumps which has capacities of 10^{-4} and 6.5×10^{-8} mbar respectively. See Figure 4.3 for the copper tray and a sample operation.

For the sake of avoiding any contamination from the residuals of the alloys arc-melted previously, the copper tray is cleaned with acetone, alcohol and polished with a special metal cleaning solution before every operation. The arc-melting device having integrated rotary and diffusion pumps, can provide an ideal and oxygen free melting atmosphere which is vital to avoid the detrimental effect of oxygen on glass forming ability of metallic glasses. The stainless steel chamber is evacuated up to 10^{-5} mbar and rinsed with 99.995% pure argon gas prior to every casting. This process removes any undesired gas that would otherwise remain in the chamber including oxygen and is repeated at least four times just to ensure the attainment of perfect melting conditions. Following that, any trace amount of oxygen is removed by gettering with pure Zirconium which is melted separately before the actual alloy. Lastly, the melting of the alloy is initiated in a 600 mbar Argon atmosphere.

All the alloys prepared are melted at least four times each time turning up side down, to ensure the homogeneity. In certain alloys involving high melting point elements like Niobium, alloy is melted more than ten times. The origin of this difficulty arises not from the weakness of the arc-melting device because the arc can produce extreme temperatures over 4000 °C, high enough to melt all elements and alloys that are dealt. The difficulty arises from the fact that the metallic glasses are mostly deep eutectics which melt at relatively low temperatures. After the first melting of the alloy, for example in the studied Fe-B-Si-Nb alloy, Fe and B also involving Si form a low melting point liquid in which the solid and denser Nb particles having a melting point over 2468°C, settle down, coming closer to the water cooled copper tray, making Nb hard to liquefy. The solid remnants could be melted by exposing higher Arc currents and reaching very high temperatures. However, this also results in loss of material from the low melting point liquid solution via evaporation or scattering. As a result, the melting requires a compromise between two opposite demands and the Arc current should be adjusted accordingly, neither too low nor too high. In such a case as in the mentioned alloy, the melted piece is cut with a Buehler Micro-Cutter and observed under optical microscope for any trace of particles that did not melt. The overall preparation of the alloy would take 6 hours in general and that would reach 12-14 in some cases as mentioned.

4.4.1.2. Rapid Solidification

The rapid solidifications of the homogenized alloy melts were conducted via Manfredi Multihertz Neutromag Digital centrifugal casting machine (See Figure 4.2) with a wedge shaped copper mould. The cavity thickness starts from 0 mm and rises to 3 mm at the end of the mould with a 16 mm width and 70 mm length. The alloys are induction melted in alumina crucibles coated with boron-nitride or yttria and driven into the pre-cooled copper moulds by centrifugal forces.



Figure 4.3 The copper tray and chamber of the Arc-Melting device is cleaned and polished prior to every melting. Zirconium metal standing solely in a small reservoir next to the -to be prepared- alloy is melted in advance to justify the removal of any trace amount of oxygen.

4.4.2. Characterization of the Alloys

4.4.2.1. X-ray Diffractometry

X-ray diffraction (XRD) was conducted to evaluate whether the analyzed region of the specimen is amorphous or retains crystalline phases and obtain the total structure factor for calculating RDFs. It was performed using a Rigaku diffractometer with $\text{CuK}\alpha$ radiation in the diffraction angle (2θ) range of 5-105°. The d-spacing of curved graphite - single crystal monochromator was 6.708 Å.

4.4.2.2. Scanning Electron Microscopy

Scanning electron microscopy (SEM) studies were performed using a JEOL JSM-6400 equipped with NORAN System 6 X-ray Microanalysis System & Semafore Digitizer. Energy dispersive spectroscopic analyses (EDS) were employed to determine the general compositions of alloys.

4.4.2.3. Differential Scanning Calorimetry

Thermal analyses were conducted using Setaram Setsys 16/18 differential scanning calorimetry (DSC) under flowing high purity argon gas and a cooling system attached to the DSC. Runs were performed with 20-30 mg of samples. All measurements are conducted as heating to 1573 K with a rate of 40 K/min (or 0.67 K/s), waiting there in molten state for 5 minutes and cooling the melt to room temperature with a rate of 40 K/min

4.4.2.4. Magnetization Measurements

Magnetization measurements were conducted on ADE Magnetics Model EV9 Vibrating Sample Magnetometer (VSM) with an optional temperature controller. Most of these measurements were performed at room temperature and magnetic field up to 2.2 kOe while several measurements are taken at higher temperatures.

4.5. Results and Discussion

4.5.1. Fe-Y-B System

Although ternary BMGs are known to be castable in Mg- and Ln- alloy systems, there was no Fe-B based ternary BMG reported until the Fe-Y-B system [119]. That study pointed out that a 2 mm diameter BMG rod with 1.47 T saturation magnetization and 40 A/m coercivity is attainable with composition of $\text{Fe}_{72}\text{Y}_6\text{B}_{22}$. Yttrium is known to act as an oxygen scavenger which is detrimental for glass formation. Moreover, it has a much bigger radius with respect to Fe and B. It has eutectics with B and Fe, the latter eutectic being located close to pure Fe. Since Y does not have a net magnetic moment, it would not be expected to worsen the magnetic properties and oppositely it is expected to improve magnetic properties due to its broadening effect on Fe-Fe separations. In summary the benefits of Y can be listed as;

- Y may provide the capability of obtaining a ternary Fe-B based BMG by increasing GFA due to;
 - Very high radius difference with Fe and B,
 - Scavenging dissolved oxygen,
 - Presence of eutectic points with Fe and B,
 - Possibility of forming stable complex crystalline compounds which require long range diffusion,

- Very promising magnetic properties,
- Lower cost with respect to elements of same type and simplifying the composition.

Since high GFA is reported to be achieved by a single ternary additive [119], the system seemed very promising for relating the high GFA of BMGs with the effects of elements increasing GFA on topology (via results of theoretical studies) and also for producing a simple good soft magnetic BMG. Accordingly, studies were initiated exploiting the promising features of $\text{Fe}_{72}\text{Y}_6\text{B}_{22}$ alloy, which later on turned out to have an insufficiently stable melt for conventional casting.

The alloy is homogenized prior to centrifugal casting by melting Fe, B and Y, all in elemental form in a cylindrical copper tray of arc melting device. The as-prepared alloys were cut into slices and cast into a pre-cooled wedge-shaped copper mould by centrifugal casting at 1523 K. The alloy melted around 1423 K which indicates the low temperature melting eutectic behavior of the alloy. This was actually one of the most important principles in determining the composition $\text{Fe}_{72}\text{Y}_6\text{B}_{22}$. The first examination of the cast alloy is conducted by bare eyes (See Figure 4.4). A tiny piece of amorphous phase exhibiting a shiny luster is seen around the thinnest sections and edges. For further investigation an XRD and an SEM micrograph of the alloy are required as given in Figure 4.5 and Figure 4.6 respectively. After CC, as it can be seen in both XRD and SEM analysis, no trace of amorphous structure can be observed in the bulk of the material. Several Fe, B and Y bearing compounds precipitated. Dendrites, especially observed in slower cooling middle sections, are found to be Fe-Y. (See Appendix C, Figure C. 1). Of course, whether they possess any B cannot be determined via available EDS equipment. The inter-dendritic phase turned out to be Fe (See Appendix C, Figure C. 2), and most probably it is also α -Fe having some dissolved B. In summary, it was concluded that Fe-Y-B BMG cannot be produced via current conventional route.

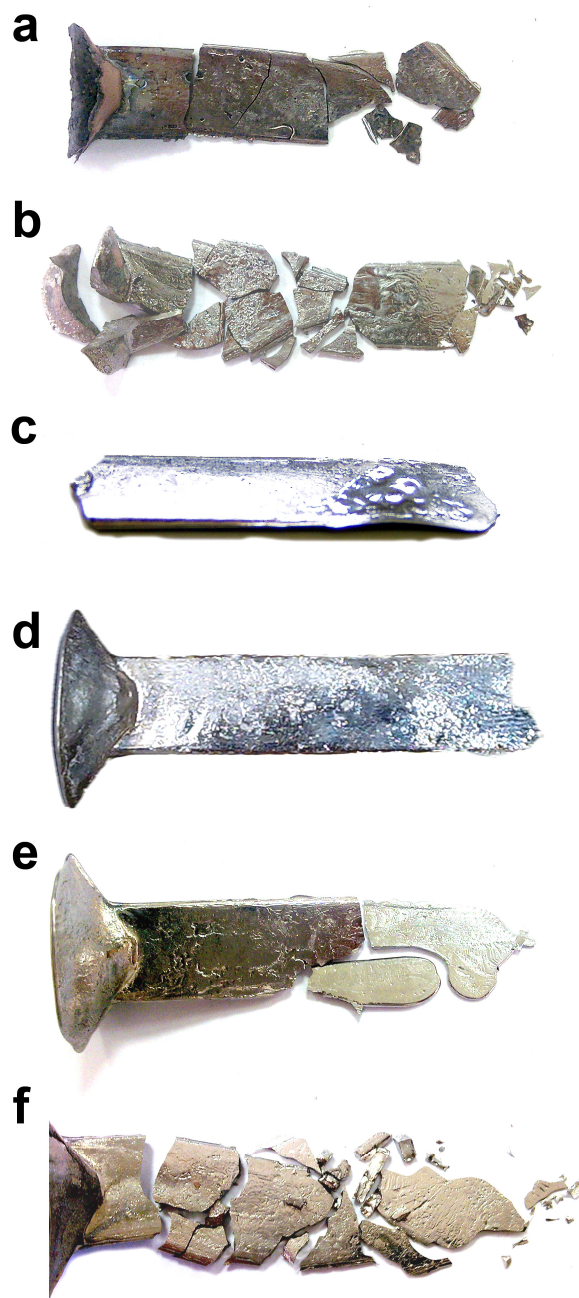


Figure 4.4 The photographs of centrifugal cast (a) Fe-Y-B, (b) Fe-Nb-B-Si, (c) Fe-Co-Nb-B-Si, (d) Fe-Co-Nb-B-Si with 0.5at.% Cu , (e) Fe-Co-Nb-B-Si with 0.75at.% Cu and (f) Fe-Co-Nb-B-Si with 1.0 at.% Cu alloys.

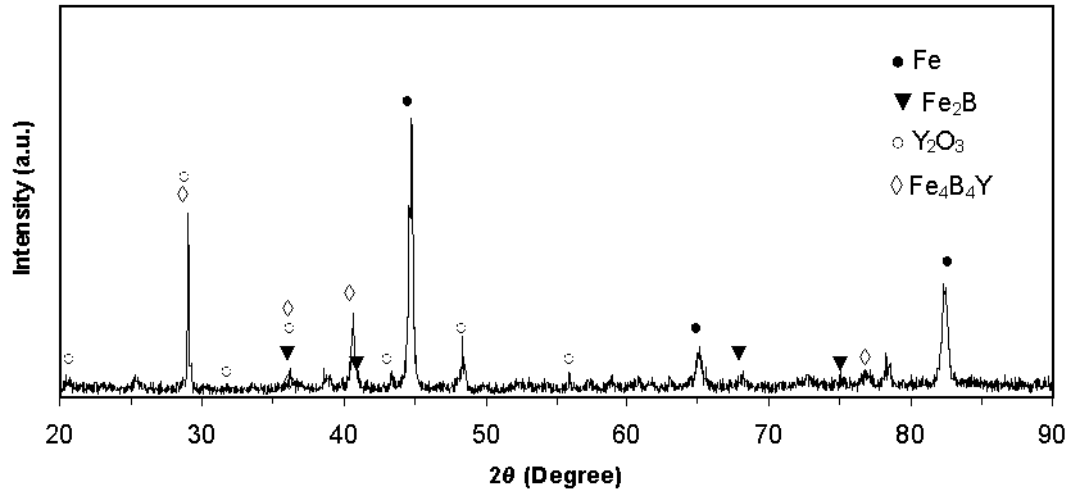


Figure 4.5 X-ray diffraction pattern of $\text{Fe}_{72}\text{Y}_6\text{B}_{22}$ alloy after centrifugal casting.

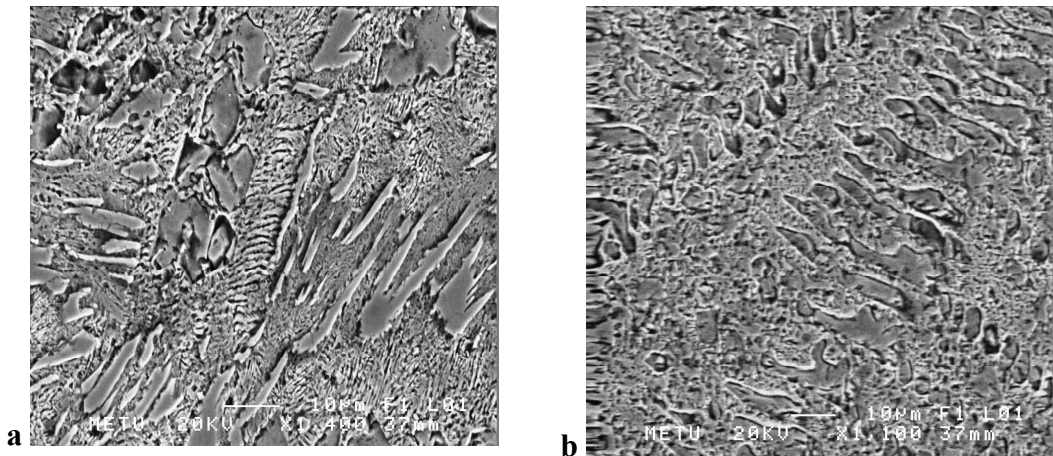


Figure 4.6 SEM images of $\text{Fe}_{72}\text{Y}_6\text{B}_{22}$ alloy taken from (a) thin sections and (b) middle sections.

4.5.2. Fe-Nb-B-Si System

As discussed in Section 4.2.2, Fe-Nb-B-Si system is worth to study due to its relatively simple composition, high GFA, similarity to Finemet alloys and good soft magnetic properties. In addition to forming BMG alloys with high GFAs, they are promising precursors for bulk nanocrystalline alloys (See Section 4.2.3) since they are compositionally derivatives of Finemet alloys. A three-fold benefit; like producing a BMG to study the glass formation phenomenon with results of theoretical studies in Chapter 3, combining those results with possible nanocrystallization of the BMG yielding a rare bulk nanocrystal alloy produced by a conventional route and at the same time obtaining good soft magnets, can be gained. This relatively simple quaternary metallic glass system with good soft magnetic properties is open for investigations related to improving the GFAs of alloys belonging to it. System allows obtaining BMGs with relatively high Fe contents (and Co also) and a TM/M ratio close to binary $\text{Fe}_{80}\text{B}_{20}$ alloys. The advantages of the system can be summarized as;

- A relatively simple composition to obtain a good soft magnetic BMG and theoretically investigate its structure,
- Capability of Nb element of improving GFA via small additions by slowing down the diffusion in the melt, and its high atomic radius differences with Fe and B atoms,
- A potential base alloy system for producing a bulk nanocrystalline alloy by proper Cu addition,
- Fe-Si alloys are good commercial soft magnets, nanocrystals of which may precipitate by proper heat treatment.

4.5.2.1. The Quaternary Alloy

In the Fe-Nb-B-Si system, the first studied composition was $\text{Fe}_{72}\text{B}_{14.4}\text{Si}_{9.6}\text{Nb}_4$ [120]. The alloys were prepared via the route given previously in Section 4.4.1. From the macroscopic observations (See Figure 4.4), it was found that a fully amorphous structure exists in thin sections, a partially amorphous structure prevails in middle sections as shown in Figure 4.7 via XRD and a fully crystalline structure exists in the thickest regions. The alloy broke into pieces due thermal shock induced in the copper mould because the co-existence of amorphous structure and intermetallics most probably made the alloy more prone to breaking apart.

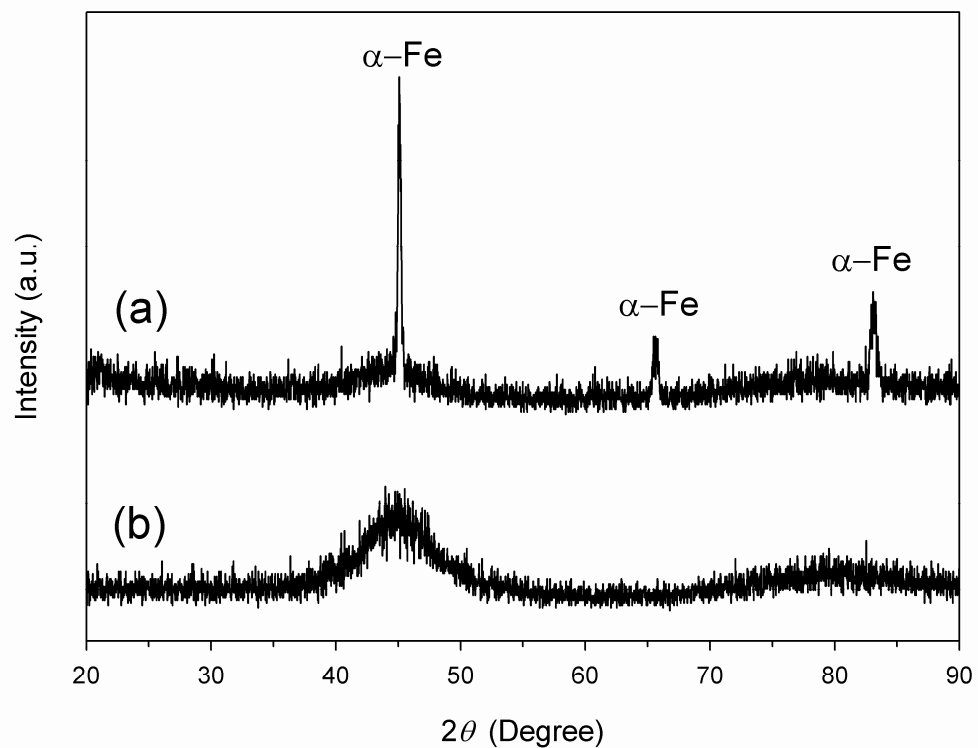


Figure 4.7 X-Ray diffractogrammes of centrifugal cast (a) partially amorphous $\text{Fe}_{72}\text{B}_{14.4}\text{Si}_{9.6}\text{Nb}_4$ and (b) bulk amorphous $\text{Fe}_{36}\text{Co}_{36}\text{B}_{19.2}\text{Si}_{4.8}\text{Nb}_4$ alloys

4.5.2.2. Cobalt Substitution

For the sake of obtaining a fully amorphous metallic alloy $\text{Fe}_{36}\text{Co}_{36}\text{B}_{19.2}\text{Si}_{4.8}\text{Nb}_4$ composition [101] was prepared. Alloys containing Nb were arc-melted more than 10 times due to sinking of Nb in the melt (See Section 4.4.1). This alloy was achieved to be cast into a fully amorphous structure with 3 mm thickness with conventional casting from alumina crucible to wedge shaped copper mould (See Figure 4.4).

One of the mostly applied instrumental characterization techniques is XRD in crystalline alloys as well as in amorphous alloys. The former would show sharp peaks related to different crystallographic planes of crystals whereas the latter would show broad maxima (*halo* patterns) related to short range order pertaining in the structure. Figure 4.7a shows a partially amorphous structure of $\text{Fe}_{72}\text{B}_{14.4}\text{Si}_{9.6}\text{Nb}_4$ with α -Fe precipitates in the matrix opposite to the *halo* pattern of $\text{Fe}_{36}\text{Co}_{36}\text{B}_{19.2}\text{Si}_{4.8}\text{Nb}_4$ in Figure 4.7b. In Figure 4.7, structural evolution of the alloy can be observed directly from suppression of Fe crystal peaks in (a), to a fully amorphous structure in (b) by proper compositional adjustment. Hirata and co-workers [121] proposed that this increase in GFA can be related to developing a MRO similar to a Fe_{23}B_6 -type meta-stable crystal which is the primary crystallization product of the latter (Co added) alloy.

An amorphous alloy is expected reflect no trace of a microstructure in any microscopic image analysis due to lack of any defect like grain boundaries or precipitates which would form detectable distinct contours upon etching and polishing the specimen. Secondary electron image is of primary interest due to its being a strong evidence of glassy state and is given in Figure 4.8 with accompanying backscattered electron image of $\text{Fe}_{36}\text{Co}_{36}\text{B}_{19.2}\text{Si}_{4.8}\text{Nb}_4$ amorphous alloy. While secondary electron image is a proof of microstructure deficient structure, back scattered image proves the compositional homogeneity of the alloy, which would not be featureless as in Figure 4.8 if there were different phases not

extracted in the secondary electron image. Although compositions are nominal, EDS analysis provided in Appendix C, Figure C. 3 shows the lack of contamination.

The fracture surface is another factor giving clues about whether the structure is amorphous or not. As shown in Figure 4.9, the fracture mode of $\text{Fe}_{36}\text{Co}_{36}\text{B}_{19.2}\text{Si}_{4.8}\text{Nb}_4$ alloy resembles that of conventional glasses or amorphous polymers. No fibrous surfaces are observed which would have supported the presence of a crystalline phase.

In addition to these SEM analyses, a macroscopic observation of the amorphous $\text{Fe}_{36}\text{Co}_{36}\text{B}_{19.2}\text{Si}_{4.8}\text{Nb}_4$ alloy specimen would readily give some clues about the microstructure. A metallic glass has some specific macroscopic features as a shiny luster with very smooth surface as shown in Figure 4.10.

4.5.2.3. Copper Addition

Due to the reasons discussed in Sections 4.2.2, 4.2.3.1 and 4.5.2, Cu additions to the current $\text{Fe}_{36}\text{Co}_{36}\text{B}_{19.2}\text{Si}_{4.8}\text{Nb}_4$ BMG composition are determined to be conducted via the present conventional route. Three new alloys with compositions of $(\text{Fe}_{36}\text{Co}_{36}\text{B}_{19.2}\text{Si}_{4.8}\text{Nb}_4)_{100-X}\text{Cu}_X$ were prepared for $X = 0.50, 0.75$ and 1.00 individually and their as-cast forms are shown in Figure 4.4. The shiny luster of the fracture surface of 3 mm region of $X = 0.75$ alloy is shown in Figure 4.10. All of these alloys were able to form at least 3 mm thick BMGs by centrifugal casting as verified by the provided *halo* X-ray patterns in Figure 4.11 with no sharp crystalline phase peaks present.

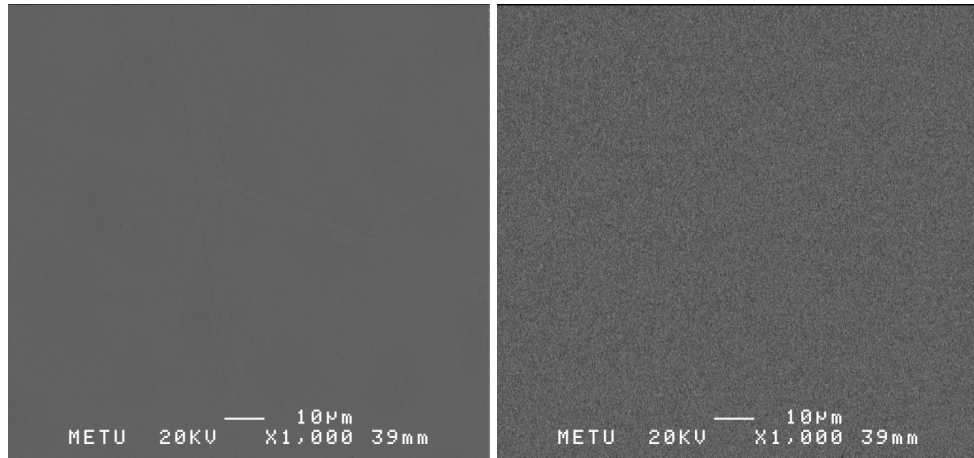


Figure 4.8 Secondary electron image (left) and back scattered electron image (right) of $\text{Fe}_{36}\text{Co}_{36}\text{B}_{19.2}\text{Si}_{4.8}\text{Nb}_4$ bulk amorphous alloy.

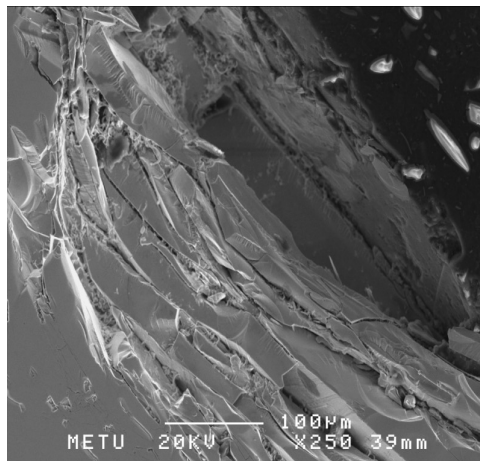


Figure 4.9 Secondary electron image of fracture surface of $\text{Fe}_{36}\text{Co}_{36}\text{B}_{19.2}\text{Si}_{4.8}\text{Nb}_4$ bulk amorphous alloy.



Figure 4.10 Photographs show the shiny luster of the 3 mm thick regions of the wedge shaped bulk amorphous $\text{Fe}_{36}\text{Co}_{36}\text{B}_{19.2}\text{Si}_{4.8}\text{Nb}_4$ (upper image) and $(\text{Fe}_{36}\text{Co}_{36}\text{B}_{14.4}\text{Si}_{9.6}\text{Nb}_4)_{99.25}\text{Cu}_{0.75}$ (lower image) alloys.

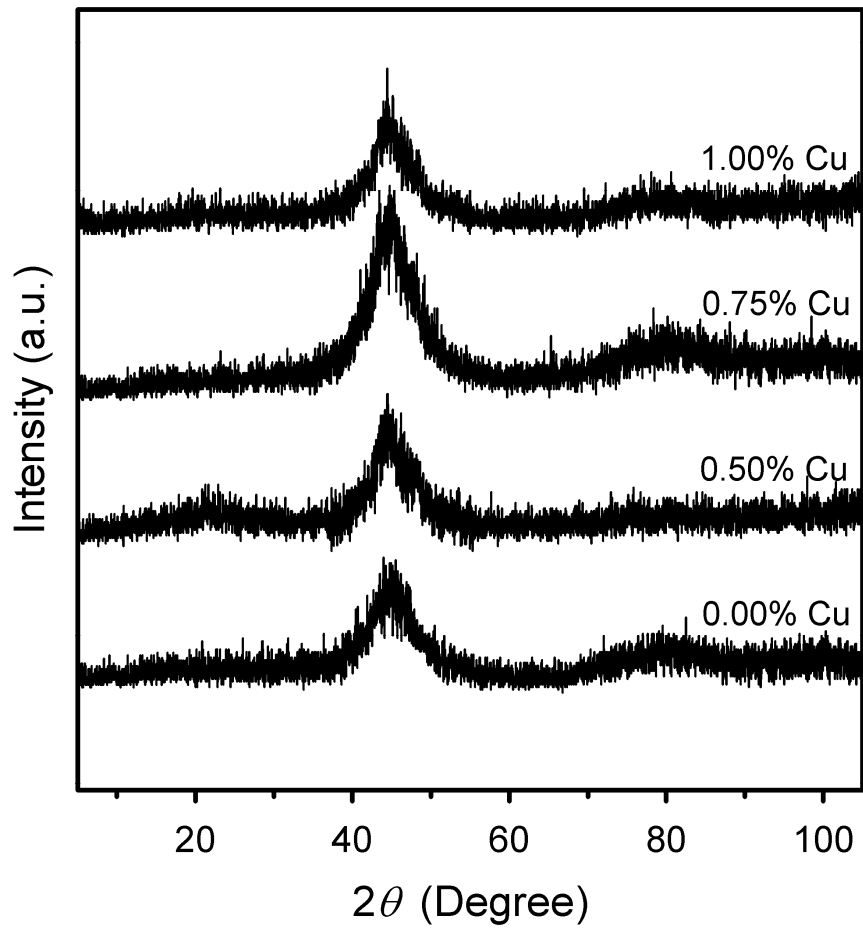


Figure 4.11 X-Ray diffractogrammes of centrifugal cast bulk metallic glass $(\text{Fe}_{36}\text{Co}_{36}\text{B}_{19.2}\text{Si}_{4.8}\text{Nb}_4)_{100-X}\text{Cu}_X$ alloys where X ranges between 0 and 1.

4.5.3. Thermal Analysis

For all of the produced bulk glassy alloys, DSC analyses were conducted with two subsequent paths, both paths bearing a heating and cooling pattern. The 1st path gives information regarding the glass transition and following crystallization of the bulk glassy alloy while the following melting pattern shows the melting of as-crystallized meta-stable phases. The cooling regions of 1st paths seemed useless due to strong local order preserving even in the molten state, thus transition temperatures are not much dependable due to effect of that remnant order in the liquid on products of solidification. Consequently, a 2nd path is initiated for all alloys, melting of which is initiated from the final solid products of 1st path and is more comparable in terms of behavior. The last path; cooling of the 2nd path is more is more dependable to extract several transition temperatures. As a result, glass transition; T_g and primary crystallization; T_x temperatures were determined from 1st heating paths and, liquidus; T_l , eutectic; T_e , allotropic transformation; $T_{\gamma-\alpha}$ and order-disorder transition; T_{odt} temperatures were determined from 2nd cooling paths. For the details of paths, see the Sequential Thermal Analysis (Section 4.5.3.1).

4.5.3.1. Sequential Thermal Analyses

A sequential thermal analysis (STA) would be beneficial for identifying the thermal behavior of the glass forming melt. In such a multicomponent system with five or six different elemental constituents it is not possible to draw definite conclusions about peaks in DSC curves. However, due to eutectic nature of these TM-M based BMGs (See Appendix A, Figure C. 1), some comments can be made for most of the peaks keeping in mind the small uncertainty remaining. The system can be thought as a two component one; a TM-rich TM-M alloy and a eutectic reaction is expected to be present near the composition.

STA of Fe₃₆Co₃₆B_{14.4}Si_{9.6}Nb₄ Alloy

Sequential thermal analysis of Fe₃₆Co₃₆B_{14.4}Si_{9.6}Nb₄ bulk glassy alloy is shown in Figure 4.12. The 1st path follows heating of the amorphous phase (follows the corresponding DSC curve in Figure 4.17), shows the melting of the alloys and ends with the subsequent solidification of this melt. The solidification behavior of this 1st path revealed no significant information other than two-fold reactions that were also observed during heating which can be attributed to eutectic reaction and primary phase precipitation. The liquid seems not well homogenized yet. As a consequence a more informative 2nd path was initiated for obtaining a more differentiable DSC pattern.

As mentioned by Hirata and co-workers [121], the first and highest amount crystallization product of Fe₃₆Co₃₆B_{14.4}Si_{9.6}Nb₄ is a Fe₂₃B₆-type meta-stable compound (See Section 4.5.4.1). Consequently, the 1st path in Figure 4.12 does not produce products close to equilibrium ones during heating. The exothermic peaks following the first crystallization of the amorphous phase (See Figure 4.16) might be due to an off-eutectic phase mixture precipitating. Due to the remnant Fe₂₃B₆ like order (as in the glassy state) after melting of the alloy, alloy solidified with a pattern similar to prior heating of the 1st path.

The 2nd path showed a similar heating behavior with the 1st path with an apparently different cooling pattern. The cooling curve of the 2nd path shows that when the liquid is more and more homogenized, the alloy approached the eutectic composition since T_e and T₁ became observable and close to each other; indicating that the composition is near eutectic. The peak in between these two points might have occurred due several reasons like; a peritectic reaction is followed by a eutectic reaction upon cooling, or a separate unknown phase like Fe₂₃B₆ precipitates in between. In summary, it can be depicted that the alloy shows a high degree of MRO even in the molten state, which cannot be removed easily even with a single melting, but it vanishes to a great extent after the second melting and composition

approaches the eutectic point. Two unmarked arrows pointing upwards near 1470 and 1490 K on heating paths in Figure 4.12 indicate extension of melting to high temperatures and consequently, the presence of a high melting point phase. The unmarked arrow pointing downwards on the 1st cooling path around 1420 K similarly shows that a weak solidification reaction is starting around that temperature. Regarding the composition of the alloy, when 1st and 2nd cooling paths are compared, there is also an additional exothermic peak around 1170 K in the 2nd path, which is not observed in the 1st path. This peak would be due to $\gamma\text{-Fe}(\text{Co}) \rightarrow \alpha\text{-Fe}(\text{Co})$ allotropic phase transformation which is expected to occur around those temperatures [117] and shows the presence of a BCC Fe(Co) phase. Since also this transition was not observed neither in heating and cooling of 1st path nor in heating of 2nd path (all of these might be occurring with Fe₂₃B₆-type metastable phase), the first-crystallization product (Fe₂₃B₆-type) is not the one that would be yielded by the eutectic reaction of the alloy, which would have produced $\alpha\text{-Fe}$ if otherwise.

STAs of (Fe₃₆Co₃₆B_{14.4}Si_{9.6}Nb₄)_{100-x}Cu_x Alloys

STAs graphs of copper modified bulk glassy (Fe₃₆Co₃₆B_{14.4}Si_{9.6}Nb₄)_{99.5}Cu_{0.5}, (Fe₃₆Co₃₆B_{14.4}Si_{9.6}Nb₄)_{99.25}Cu_{0.75} and (Fe₃₆Co₃₆B_{14.4}Si_{9.6}Nb₄)₉₉Cu₁ alloys are shown in Figure 4.13, Figure 4.14 and Figure 4.15 respectively. The 1st paths follow heating of the amorphous phase (follows the corresponding DSC curves in Figure 4.17), show the melting of the alloys and end with the subsequent solidification of these melts. The solidification behavior of these 1st paths show a near eutectic like solidification, but possible T₁ and T_e temperatures (not shown in corresponding figures) are too close. The extension of melting reaction to higher temperatures (indicated by unmarked upwards arrows around 1470 K) in the 1st heating paths is not observed in the corresponding 2nd paths, so the high-temperature melting phases might have vanished in all of the Cu added alloys. A small exothermic peak is present near 1120 K in all Cu-added alloys which might be attributed to $\gamma\text{-Fe}(\text{Co}) \rightarrow \alpha\text{-Fe}(\text{Co})$ allotropic phase transformation (See Section 4.5.3.3).

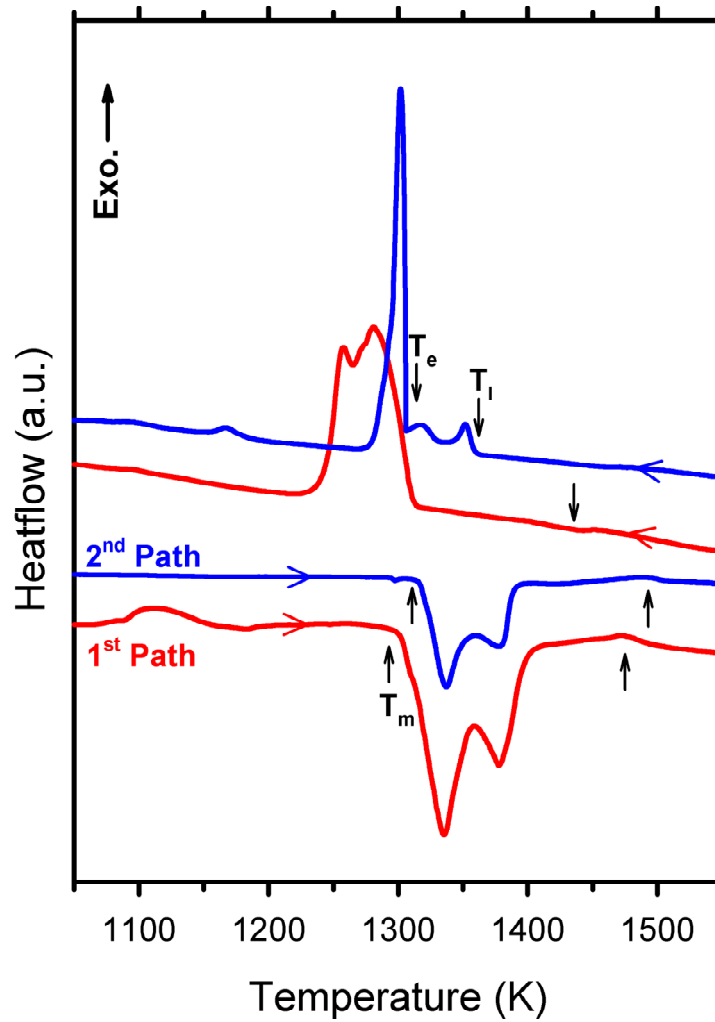


Figure 4.12 Sequential thermal analyses of $\text{Fe}_{36}\text{Co}_{36}\text{B}_{19.2}\text{Si}_{4.8}\text{Nb}_4$ bulk glassy alloy, in which 1st path is plotted in red and 2nd path in blue. Heating and cooling paths are marked with arrows pointing right and left respectively.

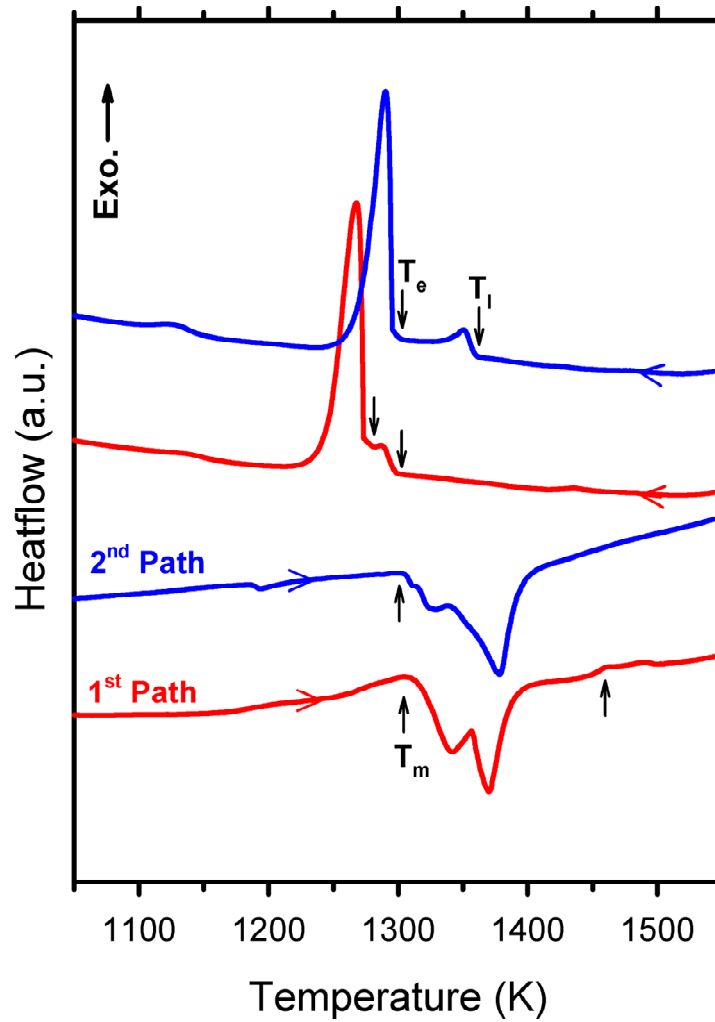


Figure 4.13 Sequential thermal analyses of $(\text{Fe}_{36}\text{Co}_{36}\text{B}_{19.2}\text{Si}_{4.8}\text{Nb}_4)_{99.5}\text{Cu}_{0.5}$ bulk glassy alloy, in which 1st path is plotted in red and 2nd path in blue. Heating and cooling paths are marked with arrows pointing right and left respectively.

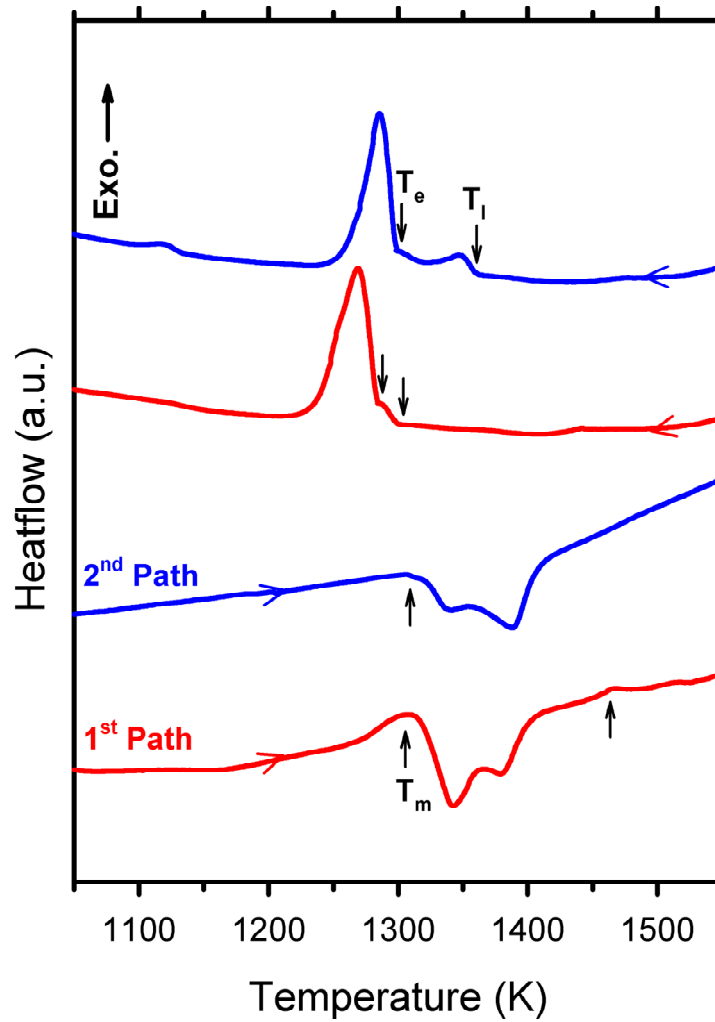


Figure 4.14 Sequential thermal analyses of $(\text{Fe}_{36}\text{Co}_{36}\text{B}_{19.2}\text{Si}_{4.8}\text{Nb}_4)_{99.25}\text{Cu}_{0.75}$ bulk glassy alloy, in which 1st path is plotted in red and 2nd path in blue. Heating and cooling paths are marked with arrows pointing right and left respectively.

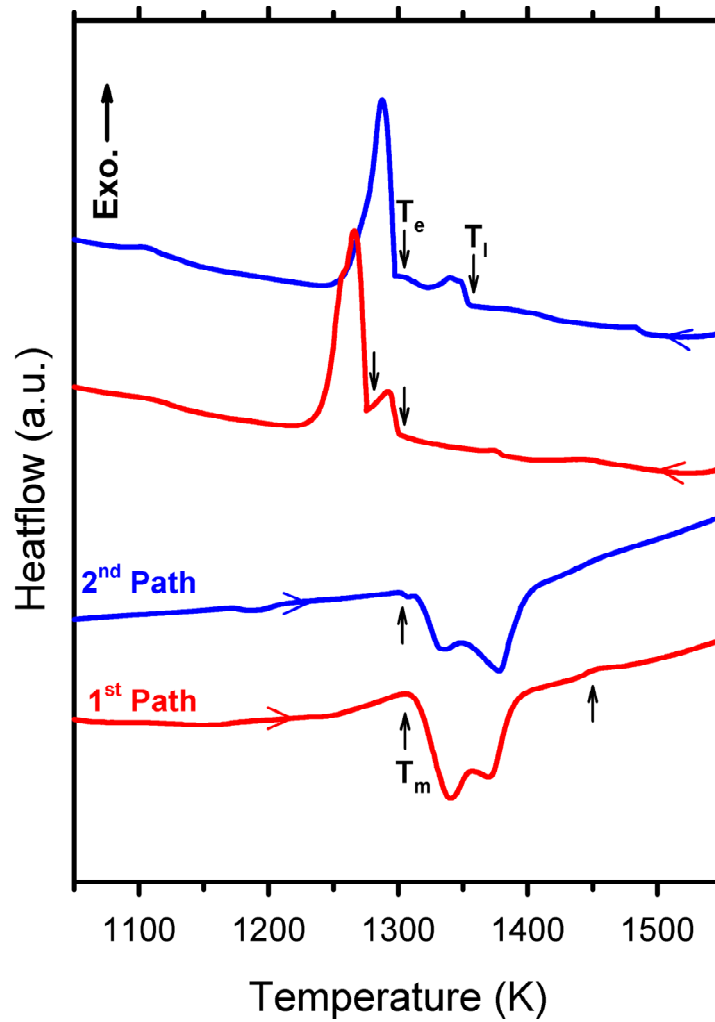


Figure 4.15 Sequential thermal analyses of $(\text{Fe}_{36}\text{Co}_{36}\text{B}_{19.2}\text{Si}_{4.8}\text{Nb}_4)_{99}\text{Cu}_1$ bulk glassy alloy, in which 1st path is plotted in red and 2nd path in blue. Heating and cooling paths are marked with arrows pointing right and left respectively.

4.5.3.2. Thermal Behavior of the Base Alloy

The DSC plot of base alloy; $\text{Fe}_{36}\text{Co}_{36}\text{B}_{19.2}\text{Si}_{4.8}\text{Nb}_4$ amorphous alloy showing the region of glass transition and following crystallization peaks are given in Figure 4.16. First, it can be depicted that the alloy could be used structurally until its T_g , located around 817 K, the supercooled liquid region follows up to 856 K which is the onset of crystallization, T_x . Presence of a very apparent glass transition and crystallization couple definitely proves the existence of an amorphous structure in $\text{Fe}_{36}\text{Co}_{36}\text{B}_{19.2}\text{Si}_{4.8}\text{Nb}_4$. The empirical parameters mentioned in Section 2.3, can readily be calculated and are listed in Table 4.2 with other important thermal parameters. Since measurements are done with a high rate of 40 K/min, the temperatures provided in Table 4.2 are highly heating/cooling rate dependent; i.e. T_g and T_x are shifted to higher temperatures T_1 is suppressed to lower temperatures, all relative to corresponding equilibrium values. As a result, thermal parameters are not exactly the same of the ones reported in [101]. A great portion of the crystallization is accomplished in the first crystallization peak with following small peaks being also exothermic. The first crystallization product was proposed to be a Fe_{23}B_6 -type meta-stable phase by Hirata et. al [121]. Consequently, alloying elements in $\text{Fe}_{36}\text{Co}_{36}\text{B}_{19.2}\text{Si}_{4.8}\text{Nb}_4$ amorphous alloy have altered the crystallization mode and the first product that nucleates is not α -Fe any more as in simpler Fe-B metallic glasses.

4.5.3.3. Effect of Cu Content on Thermal Behavior

In Figure 4.17, Figure 4.18, Figure 4.19 and Figure 4.20, low temperature region of 1st heating, high temperature regions of 1st heating, 2nd heating and 2nd cooling paths of $(\text{Fe}_{36}\text{Co}_{36}\text{B}_{19.2}\text{Si}_{4.8}\text{Nb}_4)_{100-x}\text{Cu}_x$ bulk glassy alloys are compared respectively. The transition temperatures extracted from these patterns are listed in Table 4.2.

Table 4.2 Transition temperatures and GFA parameters of BMG alloys produced, measured by DSC analysis at a rate of 40 K/min for $(\text{Fe}_{36}\text{Co}_{36}\text{B}_{19.2}\text{Si}_{4.8}\text{Nb}_4)_{100-X}\text{Cu}_X$ bulk glassy alloys. All parameters are in Kelvin except for T_{rg} which is unitless.

Parameters (K)	$X = 0$	$X = 0.5$	$X = 0.75$	$X = 1$
T_{g}	817	805	781	778
T_{x}	856	830	818	815
T_{l}	1360	1359	1358	1355
T_{e}	1307	1297	1297	1297
$T_{\gamma-\alpha}$	1185	1148	1132	1130
T_{odt}	1128	1038	1037	1029
ΔT_{x}	39	25	37	37
T_{rg}	0.601	0.592	0.567	0.567

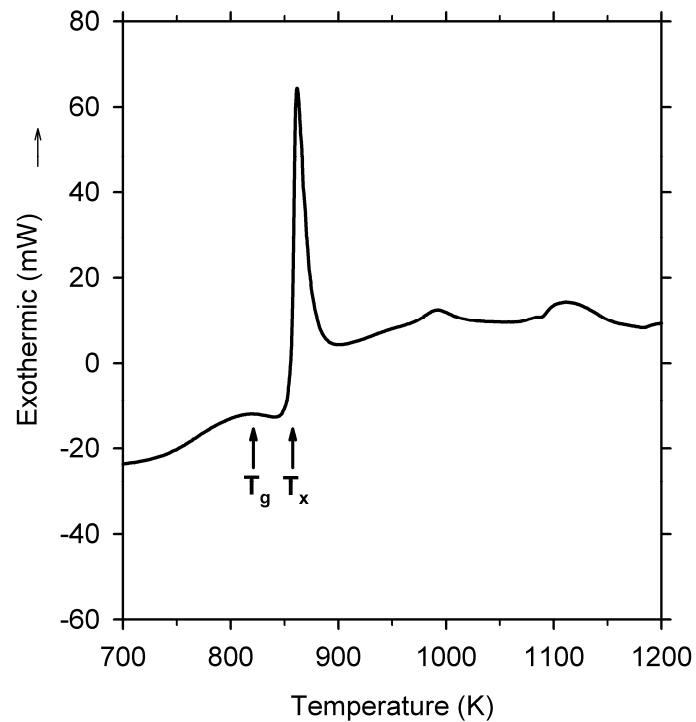


Figure 4.16 Glass transition region and crystallization of $\text{Fe}_{36}\text{Co}_{36}\text{B}_{19.2}\text{Si}_{4.8}\text{Nb}_4$ bulk amorphous alloy. Heating rate is 40 K/min.

The effects of varying copper additions on the thermal behavior of $\text{Fe}_{36}\text{Co}_{36}\text{B}_{19.2}\text{Si}_{4.8}\text{Nb}_4$ alloy near crystallization region are plotted in Figure 4.17. In all Cu added bulk glassy alloys, T_g values got lower but the clarity of transition is partially lost. This might be due to significant drops in T_x values as listed in Table 4.2, which can hinder the glass transition occurring around similar temperatures. The massive lowering of T_x in Cu added alloys is thought to be due to that Cu atoms move out of the solution prior to crystallization and form homogeneously dispersed heterogeneous nucleation sites, exploited previously in nanocrystalline alloys like Finemet [109]. Moreover, Cu additions definitely altered the crystallization mode, from a primary intense crystallization of Fe_{23}B_6 -type metastable phase [121] to several different crystallization peaks as shown in Figure 4.17. The small and broad crystallization peaks following the intense crystallization peak in Cu-free BMG are removed with Cu addition. Regardless of Cu content (effect of content is insignificant), the pattern is changed to that a broad and intense primary crystallization peak (See Table 4.2 for T_x values) is followed by a secondary crystallization peak around 940 K.

Melting regions of the as-crystallized BMGs are shown in Figure 4.18 which do not reflect the equilibrium melting since the as-crystallized products are not equilibrium ones. The actual melting behavior comparison should be done on Figure 4.19 which compares the melting regions of 2nd heating paths. Both Cu-added and Cu-free BMGs show melting reactions extending up to ~1470 K in 1st heating paths whereas this behavior completely vanishes in 2nd heating path except for Cu-free BMG. According to 2nd path, all alloys start melting around ~1300 K and finish the reaction around ~1400 K except for Cu-free alloy, which extends a tail above ~1470 K as in 1st path.

The final solidification paths; i.e., 2nd cooling paths of all alloys are compared in Figure 4.20 and extracted transition temperatures are listed in Table 4.2. Liquidus temperature T_l , gets lower with increasing Cu content indicating that composition gets closer to eutectic point with increasing amount of Cu. With Cu addition T_e

drops to 1297 K and does not vary with varying amount of Cu. Following the eutectic reaction, as the alloy is further cooled down, two exothermic reactions occur in all alloys. As mentioned previously, the first one can be attributed to γ -Fe(Co) \rightarrow α -Fe(Co) allotropic phase transformation. Fe and Co are known to have wide solubilities both in high temperature γ (FCC) and low temperature α (BCC) phases [117] and α is assumed to be a B2-type intermetallic compound. For equiatomic FeCo, which corresponds to the current alloys since they have same amount of Fe and Co, is known to go through this $\gamma \rightarrow \alpha$ transformation around 1250 K in equilibrium. The highest $T_{\gamma-\alpha}$ is 1185 K which is observed in Cu-free BMG. This lower $T_{\gamma-\alpha}$ can be firstly due to thermal effect (the cooling rate is relatively high for obtaining an equilibrium value) and secondly due to probable dissolution of other alloying elements (e.g. Si [117]) in that γ phase. In Cu-added alloys, $T_{\gamma-\alpha}$ is significantly lowered with increasing amount of Cu. After $\gamma \rightarrow \alpha$ transformation, the disordered A2 phase is expected to go through an A2 \rightarrow B2 order disorder transition (ODT) with further cooling. In equilibrium, the equiatomic FeCo is known to go through this ODT reaction around 1000 K [117], and for Cu-free bulk glassy alloy, a higher T_{odt} of 1128 K, probably due to dissolved Si [117] is observed. With further alloying with Cu, T_{odt} gets lower and comparable to equilibrium value of 1000 K, but still stays higher than that value. Again Cu is known have such effect on ODT in FeCo [117]. These differences in T_{odt} values cannot be identified easily, since ODT reactions are extremely sensitive to many variables like, kind and amount of dissolved alloying element, grain size, cooling or heating rate etc. which could not be identified simultaneously and out of scope of this study. However, these results are promising for a soft magnetic alloy, since FeCo is known to yield the highest saturation magnetization of any material [117] and if these FeCo crystals can be stabilized in nano-scale, the alloy would provide excellent soft magnetic properties.

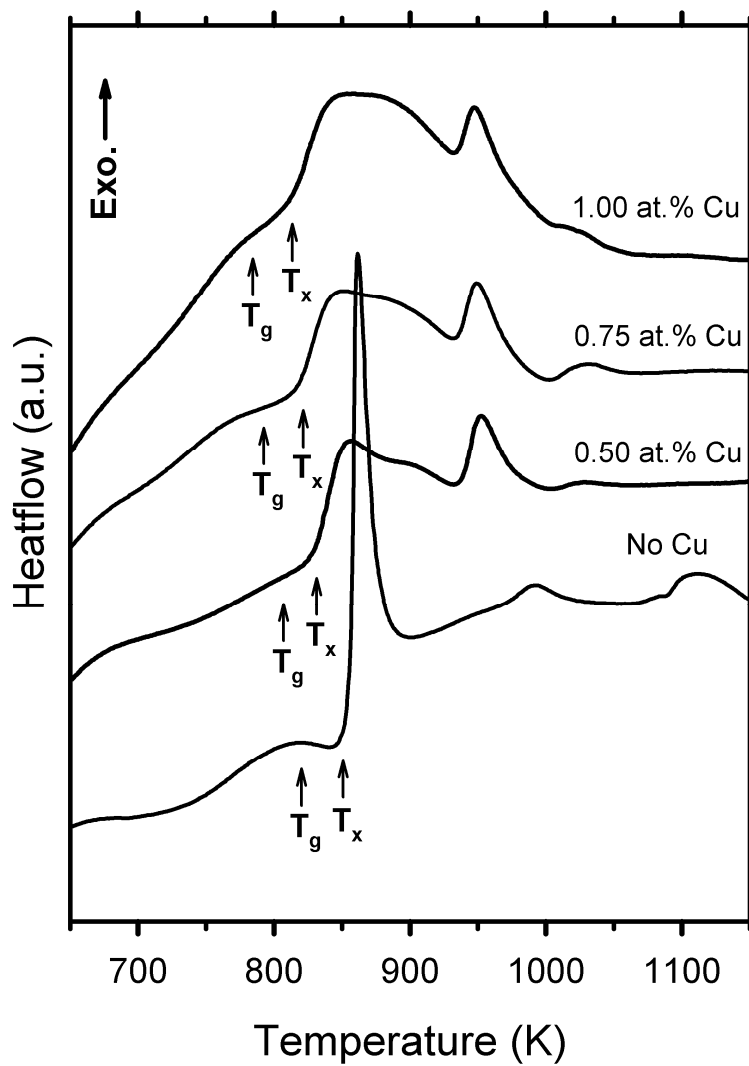


Figure 4.17 Comparison of low temperature regions of 1st heating paths of $(\text{Fe}_{36}\text{Co}_{36}\text{B}_{19.2}\text{Si}_{4.8}\text{Nb}_4)_{100-X}\text{Cu}_X$ bulk glassy alloys where X ranges between 0 and 1, showing the glass transition and crystallization regions.

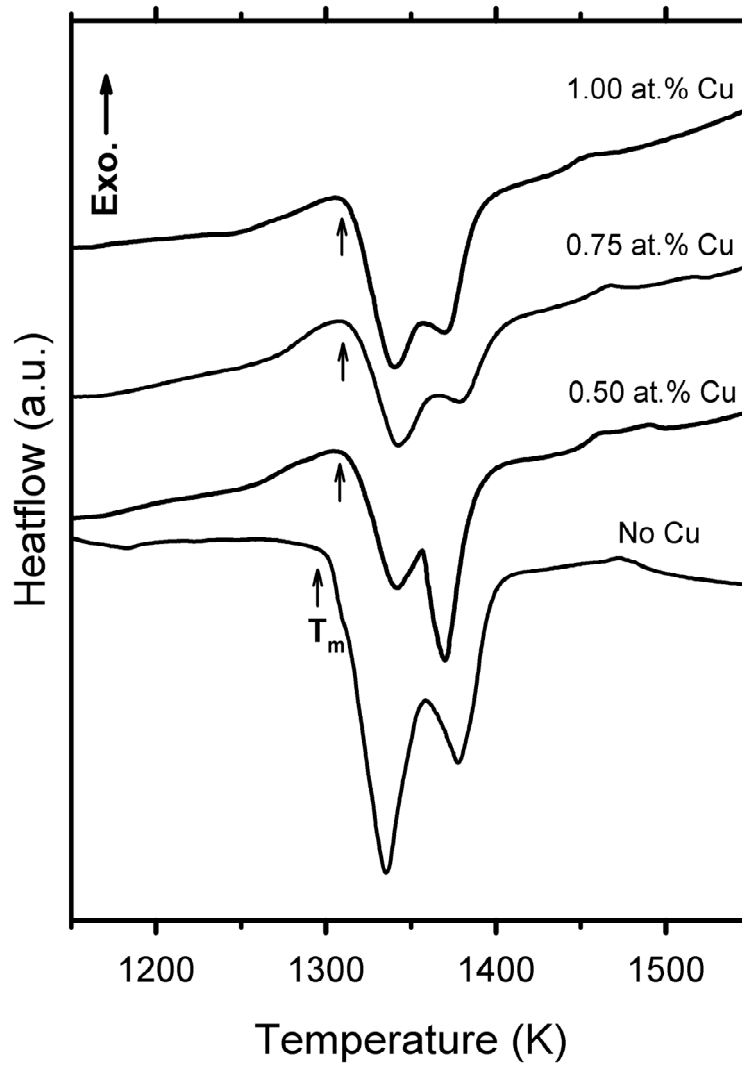


Figure 4.18 Comparison of high temperature regions of 1st heating paths of $(\text{Fe}_{36}\text{Co}_{36}\text{B}_{19.2}\text{Si}_{4.8}\text{Nb}_4)_{100-X}\text{Cu}_X$ bulk glassy alloys where X ranges between 0 and 1, showing the melting behaviors of as-crystallized alloys.

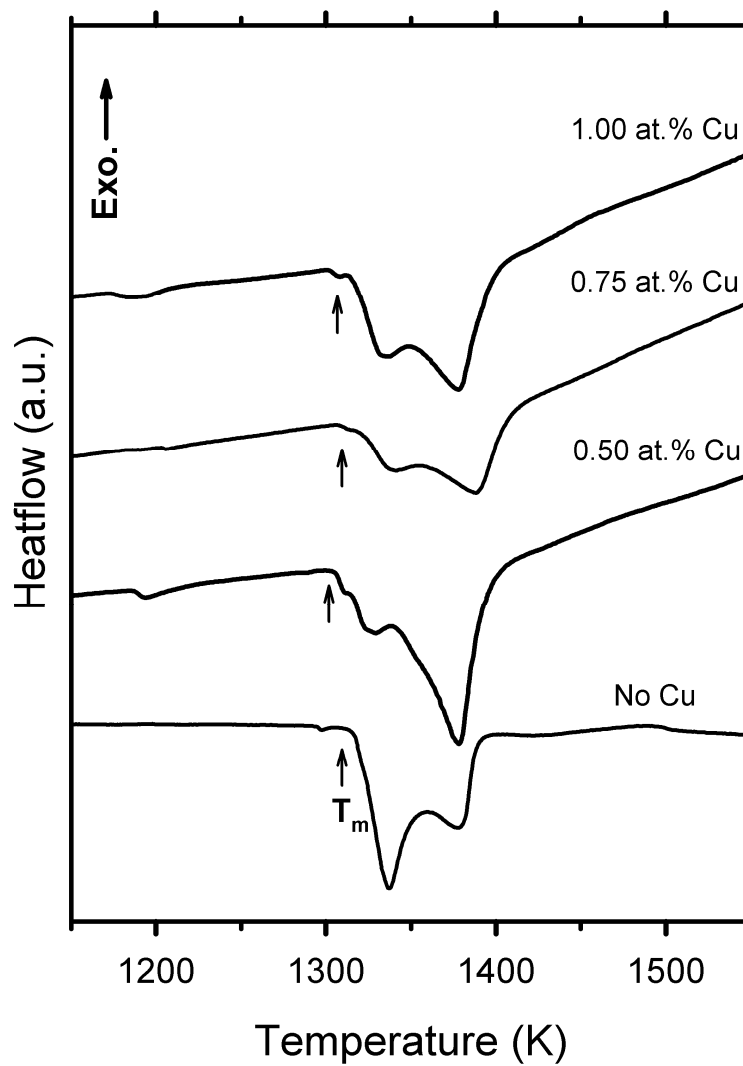


Figure 4.19 Comparison of 2nd heating paths of $(\text{Fe}_{36}\text{Co}_{36}\text{B}_{19.2}\text{Si}_{4.8}\text{Nb}_4)_{100-x}\text{Cu}_x$ bulk glassy alloys where X ranges between 0 and 1, showing the melting behaviors following the 1st solidification.

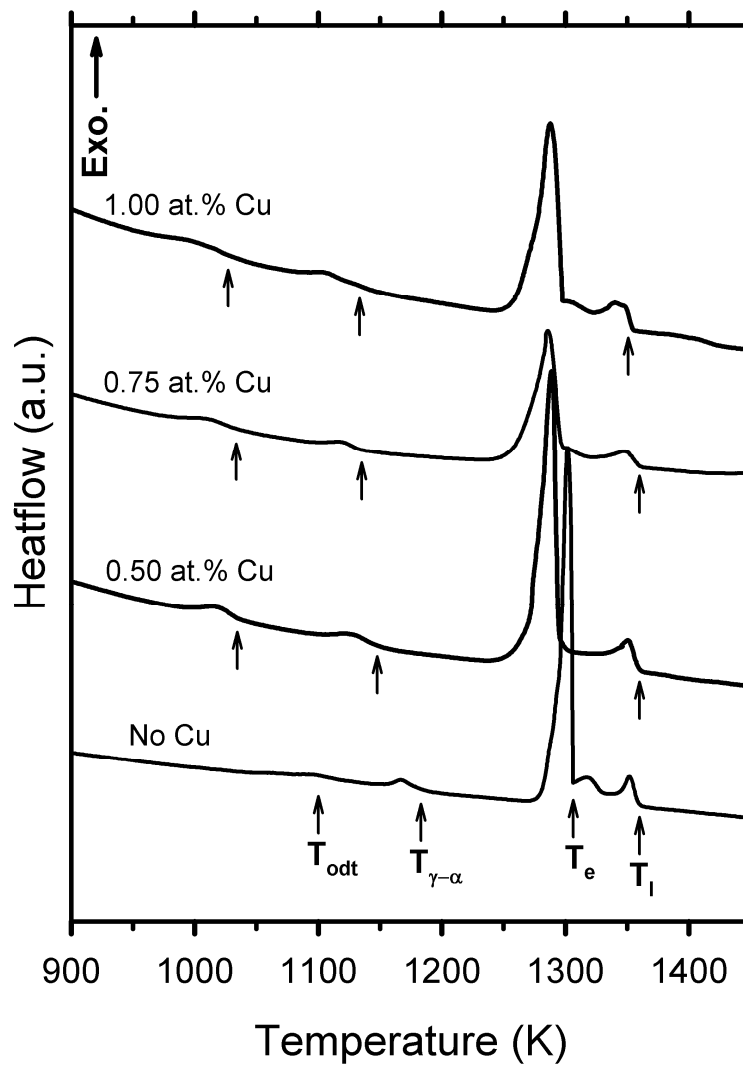


Figure 4.20 Comparison of 2nd cooling paths of $(\text{Fe}_{36}\text{Co}_{36}\text{B}_{19.2}\text{Si}_{4.8}\text{Nb}_4)_{100-x}\text{Cu}_x$ bulk glassy alloys where X ranges between 0 and 1, showing the solidification behaviors following the 2nd melting.

4.5.4. Nanocrystallization from BMG Precursors

4.5.4.1. Nanocrystallization of $\text{Fe}_{36}\text{Co}_{36}\text{B}_{19.2}\text{Si}_{4.8}\text{Nb}_4$

For the sake of verifying that the proposed primary crystallization product of the base BMG is Fe_{23}B_6 type meta-stable phase [121], the as-quenched and bulk glassy $\text{Fe}_{36}\text{Co}_{36}\text{B}_{19.2}\text{Si}_{4.8}\text{Nb}_4$ alloy is annealed between first (856 K) and second crystallization (~1000 K) temperatures at 943 K for 1.2 ks (20 min.). Since a MRO similar to Fe_{23}B_6 in the amorphous phase is thought to be responsible for the increase in GFA and precipitation of such a meta-stable phase upon crystallization, the XRDs given in Figure 4.21, comparing the as-quenched and annealed BMGs are very important. The corresponding diffraction peaks of crystallographic planes are similar to that reported in [122]. The precipitated phases are identified as Fe_{23}B_6 and $\alpha\text{-Fe}$, where the former might have Co and Nb dissolved whereas the latter might have Co, Si, etc. dissolved. The $(\text{Fe, Co, Nb})_{23}\text{B}_6$ phase has an FCC type unit cell with a large lattice parameter a , which is calculated from the provided XRD pattern as 1.0602 nm. A complex crystal with such a large lattice parameter requires long range diffusion and increases the GFA of the base alloy. The lattice parameter of the BCC $\alpha\text{-(Fe, Co, Si)}$ phase is calculated as 0.2844 nm, which is quite similar to that reported for stoichiometric FeCo alloy [117].

4.5.4.2. Nanocrystallization of $(\text{Fe}_{36}\text{Co}_{36}\text{B}_{19.2}\text{Si}_{4.8}\text{Nb}_4)_{100-x}\text{Cu}_x$

Considering the DSC analysis (See Figure 4.17), with Cu modifications, the crystallization mode of $\text{Fe}_{36}\text{Co}_{36}\text{B}_{19.2}\text{Si}_{4.8}\text{Nb}_4$ is altered from a primary intense crystallization of Fe_{23}B_6 -type phase (verified in Section 4.5.4.1) to several exothermic crystallization peaks of unknown phases. Accordingly, if the first crystallization peak in Cu added alloys is changed to precipitation of

α -Fe(Co,Si,etc.) particles in the amorphous matrix, bulk nanocrystalline soft magnetic alloys can be synthesized. A heat-treatment comprising of 300 s of isothermal treatment at 873 K, which is just above the peak of the primary crystallizations of Cu-added alloys (Table 4.2), is conducted in argon flowing atmosphere. The resulting alloy microstructures are qualitatively analyzed by XRD method as given in Figure 4.22. With increasing Cu content, precipitation of a BCC crystal-phase can be observed and is most significant for bulk glassy precursors with 0.75 and 1.00 at.% Cu, while for 0.5 at.% Cu added alloy a weaker crystallization is observed. This observation proves that the first crystallization peaks in DSC plots of Cu-added BMGs (Figure 4.17) corresponds to precipitation of α -FeCo. The relative degrees of accomplished nanocrystallization seems parallel to the drop in T_x with increasing copper amount, which accordingly increases the driving force for nucleation at a given annealing temperature. For both $X = 0.75$ and 1.00 alloys, the lattice parameters of the BCC α -Fe(Co,Si,etc.) nanocrystals are calculated as 0.2850 nm, again in good agreement with equiatomic α -FeCo [117]. The crystal size is roughly estimated by Scherrer formula; $B = 0.9\lambda_{Cu}/(t\cos\theta)$ where B is the broadening (full width at half maximum) in radians, λ_{Cu} is wave-length of diffracting beam; i.e. $CuK\alpha$ (1.5418 Å), t is the average grain size, and θ is the diffraction angle. The broadening B is corrected in reference to a FeAl standard sample. Finally, the grain sizes of alloys with 0.75 and 1.00 at.% Cu additions are estimated as 12 and 18 nm respectively. Although these values are rough and lack precision, it can definitely be concluded that the annealed BMG $(Fe_{36}Co_{36}B_{19.2}Si_{4.8}Nb_4)_{99.25}Cu_{0.75}$ and $(Fe_{36}Co_{36}B_{19.2}Si_{4.8}Nb_4)_{99}Cu_1$ alloys yielded crystals precipitated in nano-scale and they can be regarded as nanocrystals. Consequently, besides showing that the $(Fe, Co, Nb)_{23}B_6$ phase is suppressed and first crystallization product is altered to a BCC crystal like α -Fe(Co) phase (B2-type FeCo intermetallic), two bulk nanocrystalline alloys (BNCA, nanocrystals embedded in amorphous matrix) are achieved to be developed in Fe-Nb-B-Si system.

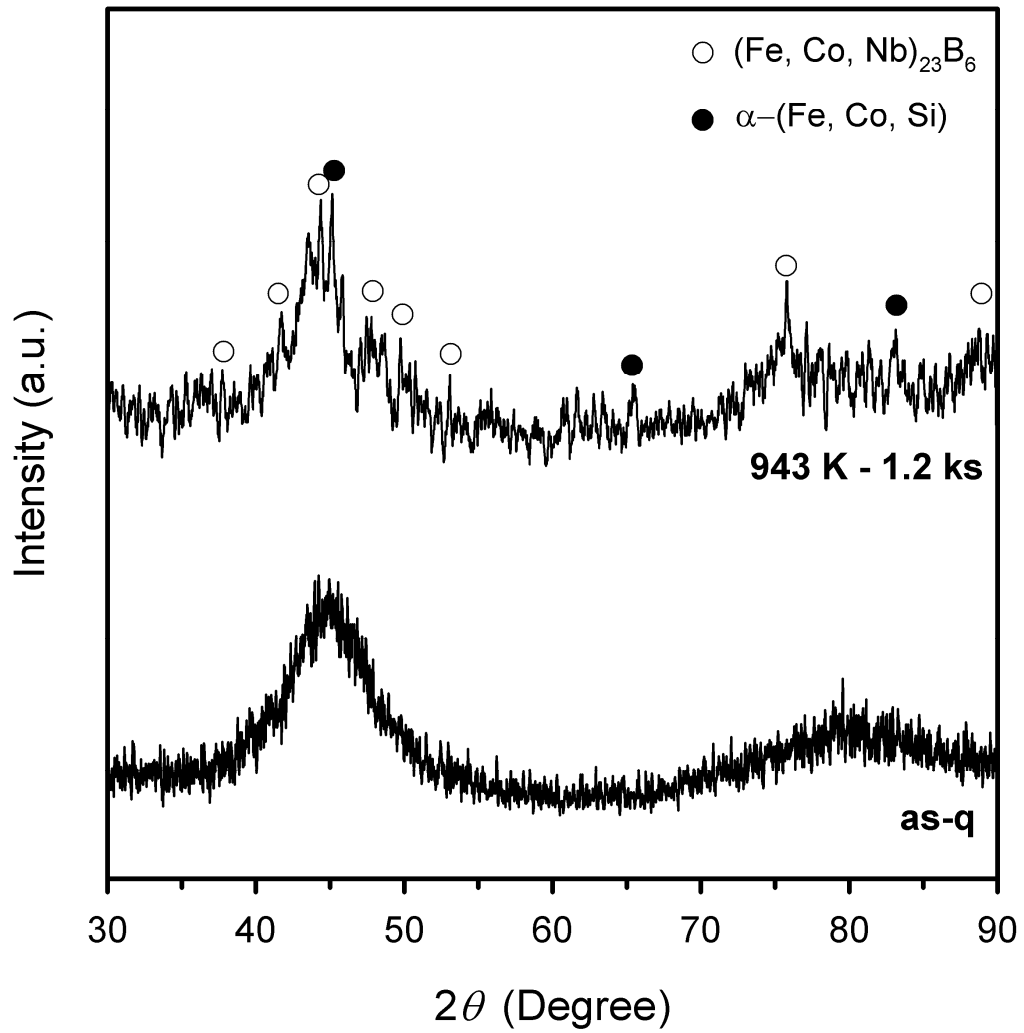


Figure 4.21 X-Ray diffractogrammes of as-quenched (as-q) and annealed $\text{Fe}_{36}\text{Co}_{36}\text{B}_{19.2}\text{Si}_{4.8}\text{Nb}_4$ alloys.

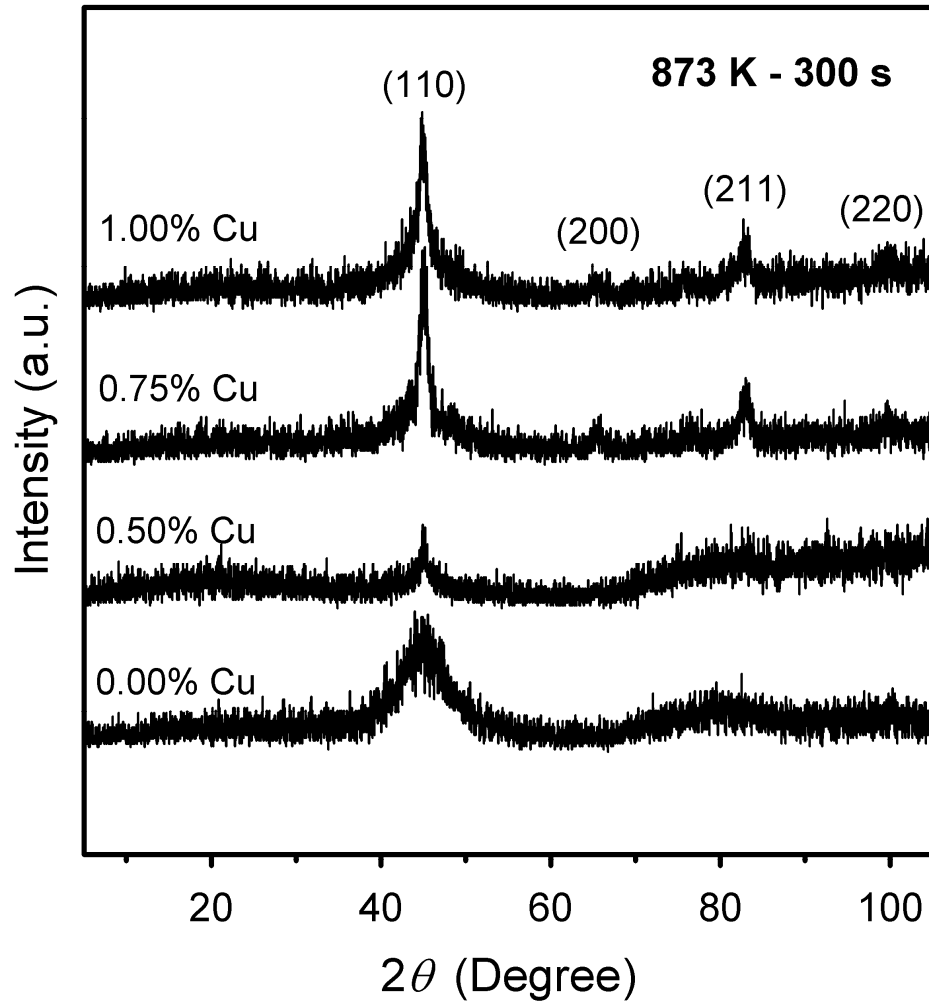


Figure 4.22 X-Ray diffractogrammes of $(\text{Fe}_{36}\text{Co}_{36}\text{B}_{19.2}\text{Si}_{4.8}\text{Nb}_4)_{100-x}\text{Cu}_x$ alloys annealed at 873 K for 300 s, where X ranges between 0 and 1. The XRD peaks are marked with the corresponding BCC plane indices.

4.5.5. Magnetic Measurements

The soft magnetic performances of the alloys are also important for their promising uses since they have been developed in a totally conventional route. The desired properties for a soft magnet can be described as a saturation induction above 1 T and coercivity below 1000 A/m (~13 Oe). The room temperature (RT) saturation magnetization and coercivity of $\text{Fe}_{36}\text{Co}_{36}\text{B}_{19.2}\text{Si}_{4.8}\text{Nb}_4$ BMG are measured as 1.02 T and 0.239 Oe (1 Oe = 79.58 A/m) respectively and hysteresis (B-H) loop is given in Figure 4.23, proving that this alloy is a good soft magnet without any phase precipitated which shows no ferromagnetism. The inset shows the region of B-H loop near zero field strength, clarifies the very low coercivity. Very surprisingly magnetic properties of the current BMG produced via the current conventional route are much better than the ones reported in the original work [101] in which; e.g., B_s was reported as 0.84 T.

The response of B-H loop of $\text{Fe}_{36}\text{Co}_{36}\text{B}_{19.2}\text{Si}_{4.8}\text{Nb}_4$ BMG to increasing temperature is sketched in Figure 4.24 where the upper inset shows an amplified example of paramagnetic state at 873 K. The coercivities (H_c 's) did not vary much as expected, but saturation induction B_s dropped significantly with increasing temperature. Due to thermal fluctuations induced by the DSC instrument, the Curie temperature T_c was not readily extractable from the previous DSC analyses. However, from data provided in Figure 4.24, exploiting the power law dependence of ferromagnets below their T_c , a fitting to $B_s \approx k(T_c - T)^n$ relation was carried out to roughly estimate the T_c as shown in the lower inset. All B_s values were assumed to be B values at 2.2 kOe, including the paramagnetic states. By setting $n \approx 0.55$ and scaling with an appropriate k factor, T_c of the alloy is estimated as 690 K, which is similar to the one reported in [101].

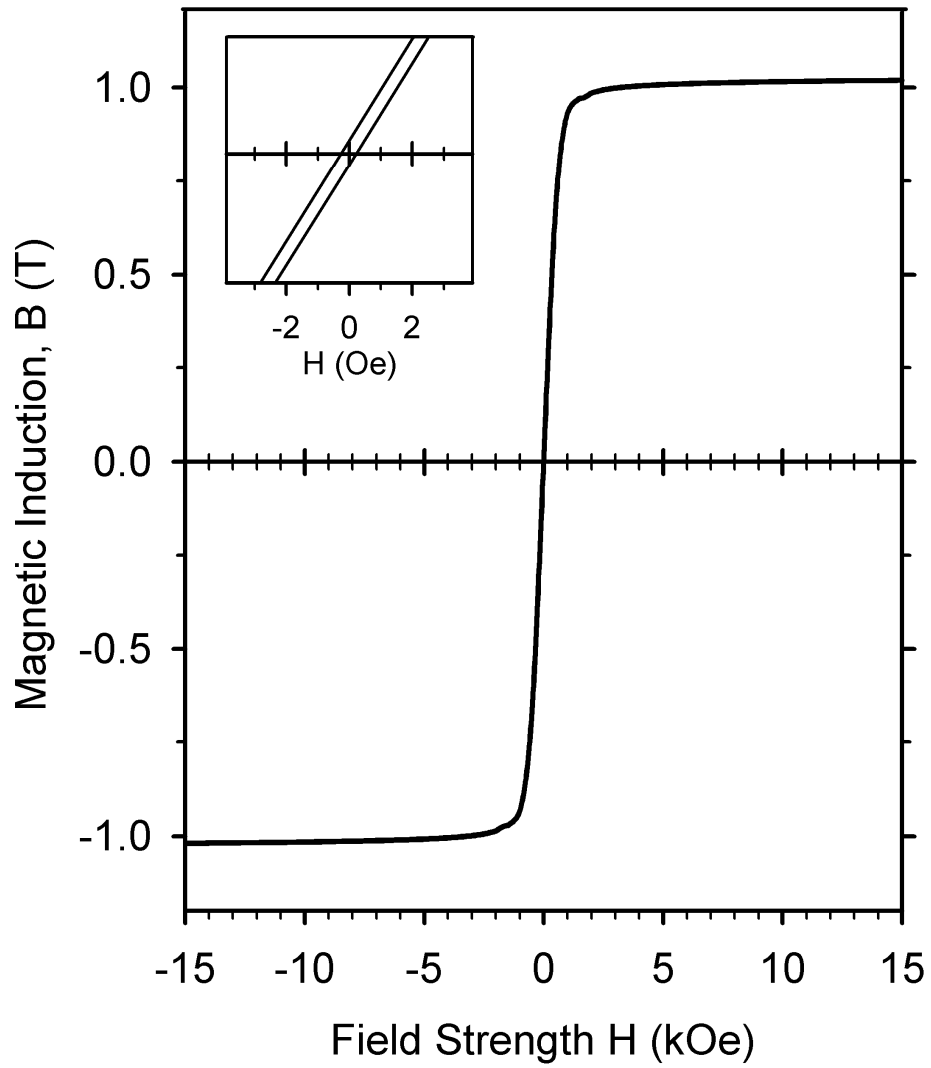


Figure 4.23 Hysteresis loop of bulk glassy $\text{Fe}_{36}\text{Co}_{36}\text{B}_{19.2}\text{Si}_{4.8}\text{Nb}_4$ alloy. Inset shows the region around zero field strength.

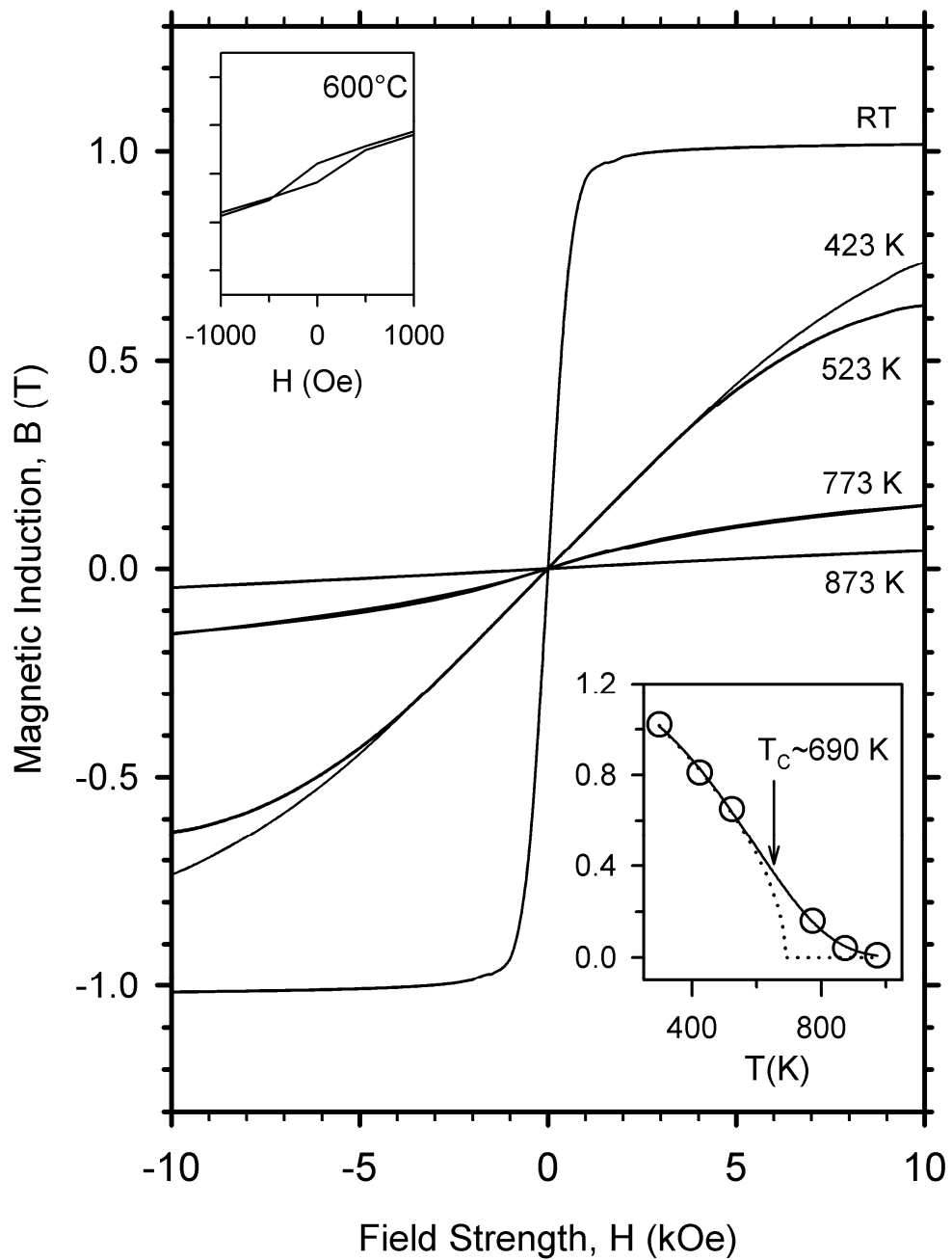


Figure 4.24 Hysteresis loops of amorphous $\text{Fe}_{36}\text{Co}_{36}\text{B}_{19.2}\text{Si}_{4.8}\text{Nb}_4$ alloy at RT (room temperature), 423, 523, 773 and 873 K. Upper inset shows the region around zero field strength at 873 K. Lower inset shows the application of power law for estimation of T_c .

The effect of Cu modification on the magnetic behavior of the $\text{Fe}_{36}\text{Co}_{36}\text{B}_{19.2}\text{Si}_{4.8}\text{Nb}_4$ glassy base alloy is provided in Figure 4.25. Cu seems to alter the shape of the B-H loop and monotonously lowers the B_s values with increasing amount. The slightly altered shapes can be attributed to demagnetization effects caused due samples being in bulk forms and is observed in previously reported bulk nanocrystalline soft magnets [123, 124]. Accompanying the slight lowering in magnetization, above 0.5 at.%, Cu causes a drastic drop in H_c values like 0.028 Oe for $X = 1$, as listed in Table 4.3, which are excellent values for a good soft magnet.

After annealing the Cu-added as-quenched BMGs at 873 K for 300 s and obtaining an α -(Fe,Co,Si) phase dispersed in the amorphous matrix in all of them, extreme improvements in saturation induction are observed as shown in B-H loops traced in Figure 4.26. After nanocrystallization, H_c 's of the bulk nanocrystalline alloys (BNCAs) turned out slightly larger than their corresponding BMG precursors (Figure 4.27) but for alloys of $X \geq 0.5$, H_c values fall at least below that of the amorphous base alloy. In addition to an H_c of 0.449 Oe, the $X = 0.5$ alloy also bears a lower B_s of 1.43 T among other annealed alloys of higher Cu content. The reason behind its higher H_c relative to the amorphous precursor and lower B_s relative to higher Cu-alloys can be described as that, nanocrystallization was stuck at its onset which would yield insufficient exchange coupling of nanocrystals since they would share a small volume fraction of the material at that point. This phenomenon is further supported by the drops in H_c 's and increases in B_s 's of annealed $X = 0.75$ and 1.0 alloys relative to $X = 0.5$ alloy as shown in Figure 4.27 because $X = 0.75$ and 1.0 alloys revealed more distinct α -(Fe,Co,Si) peaks in XRD analyses (see Figure 4.22). Consequently, with increasing Cu content, magnetic softening is enhanced due to higher driving forces for nucleation resulting from lower T_x values (See Table 4.2). Moreover, any undetectable phase other than α -(Fe,Co,Si) precipitated in the amorphous matrix would be pinning the domain walls.

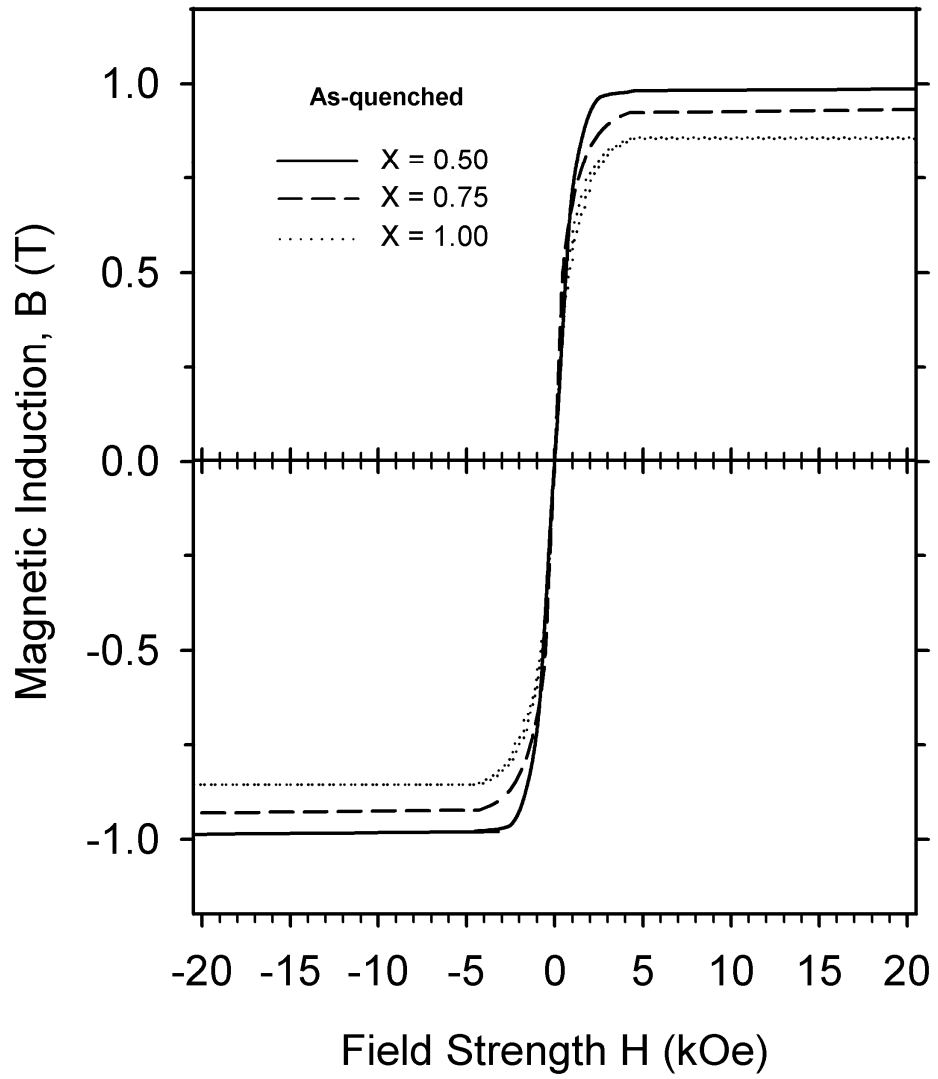


Figure 4.25 Hysteresis loops of as-quenched $(\text{Fe}_{36}\text{Co}_{36}\text{B}_{19.2}\text{Si}_{4.8}\text{Nb}_4)_{100-x}\text{Cu}_x$ bulk glassy alloys.

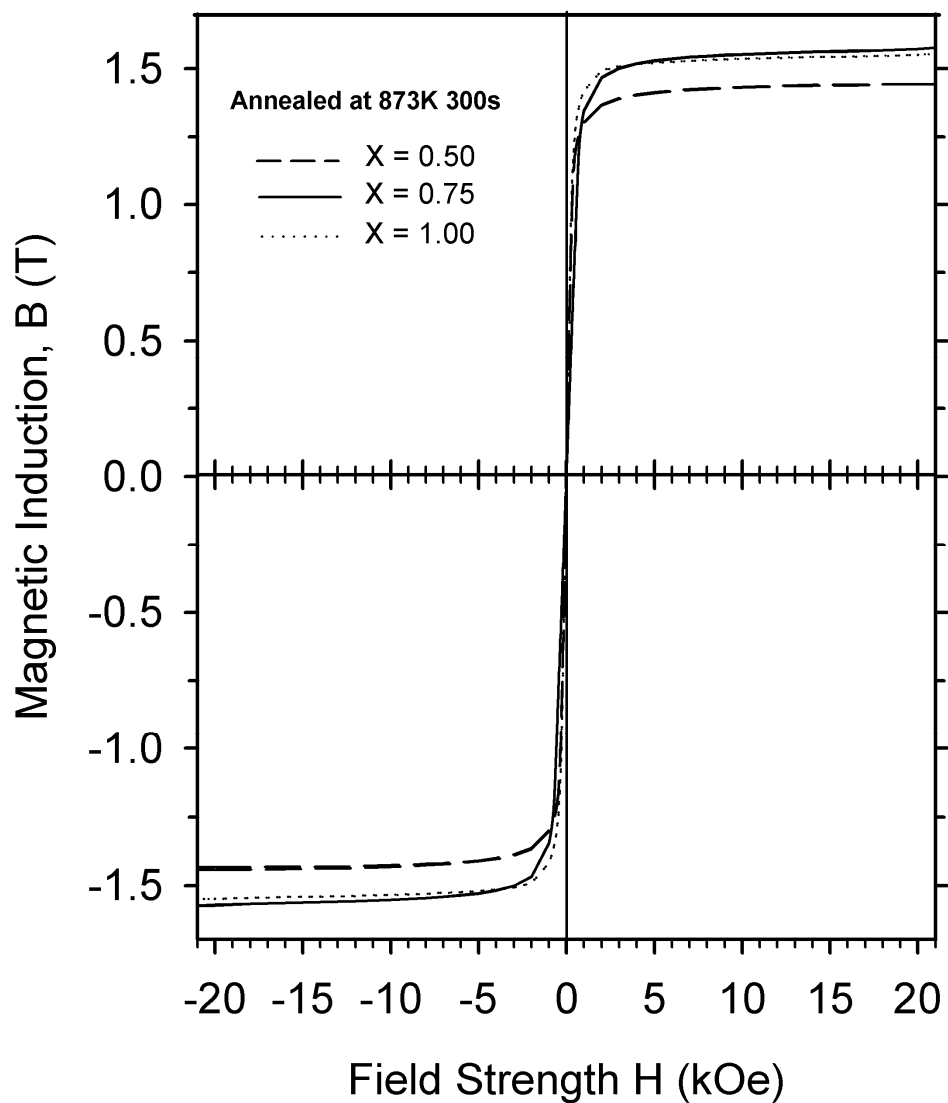


Figure 4.26 Hysteresis loops of soft magnetic $(\text{Fe}_{36}\text{Co}_{36}\text{B}_{19.2}\text{Si}_{4.8}\text{Nb}_4)_{100-x}\text{Cu}_x$ bulk nanocrystalline alloys obtained by annealing the corresponding BMG alloys at 873 K for 300 s.

As it can be depicted from Figure 4.16, the first crystallization is actually comprised of two consecutive peaks overlapping partially, which brings about a confinement to annealing temperature, since while first sub-peak is definitely due to precipitation of a BCC phase, the higher temperature sub-peak may cause precipitation of undesired non-magnetic or such domain pinning compounds. A critical complication of these alloys arises as; due to the lack of a large gap between primary and secondary crystallizations observed in an Fe- and Si-rich derivatives [125], isothermal heat treatment is confined to a rather small temperature range. However, current annealing at 873 K for 300 s provided excellent soft magnetic properties in anyway for all Cu-added BNCA alloys. The optimum performance is attained for the BNCA corresponding to the best glass forming composition, $(\text{Fe}_{36}\text{Co}_{36}\text{B}_{19.2}\text{Si}_{4.8}\text{Nb}_4)_{99.25}\text{Cu}_{0.75}$ with a high saturation induction of 1.58 T and low coercivity of 0.148 Oe respectively. BNCA $(\text{Fe}_{36}\text{Co}_{36}\text{B}_{19.2}\text{Si}_{4.8}\text{Nb}_4)_{99}\text{Cu}_1$ exhibited a slightly lower B_s of 1.55 T and slightly larger H_c of 0.162 Oe.

Table 4.3 Magnetic properties of $(\text{Fe}_{36}\text{Co}_{36}\text{B}_{19.2}\text{Si}_{4.8}\text{Nb}_4)_{100-x}\text{Cu}_x$ as-quenched bulk glassy alloys and annealed bulk nanocrystalline alloys measured at room temperature.

X	As-quenched		Annealed	
	B_s (T)	H_c (Oe)	B_s (T)	H_c (Oe)
1	0.86	0.028	1.55	0.162
0.75	0.93	0.048	1.58	0.148
0.5	0.98	0.228	1.43	0.449
0	1.02	0.239	-	-

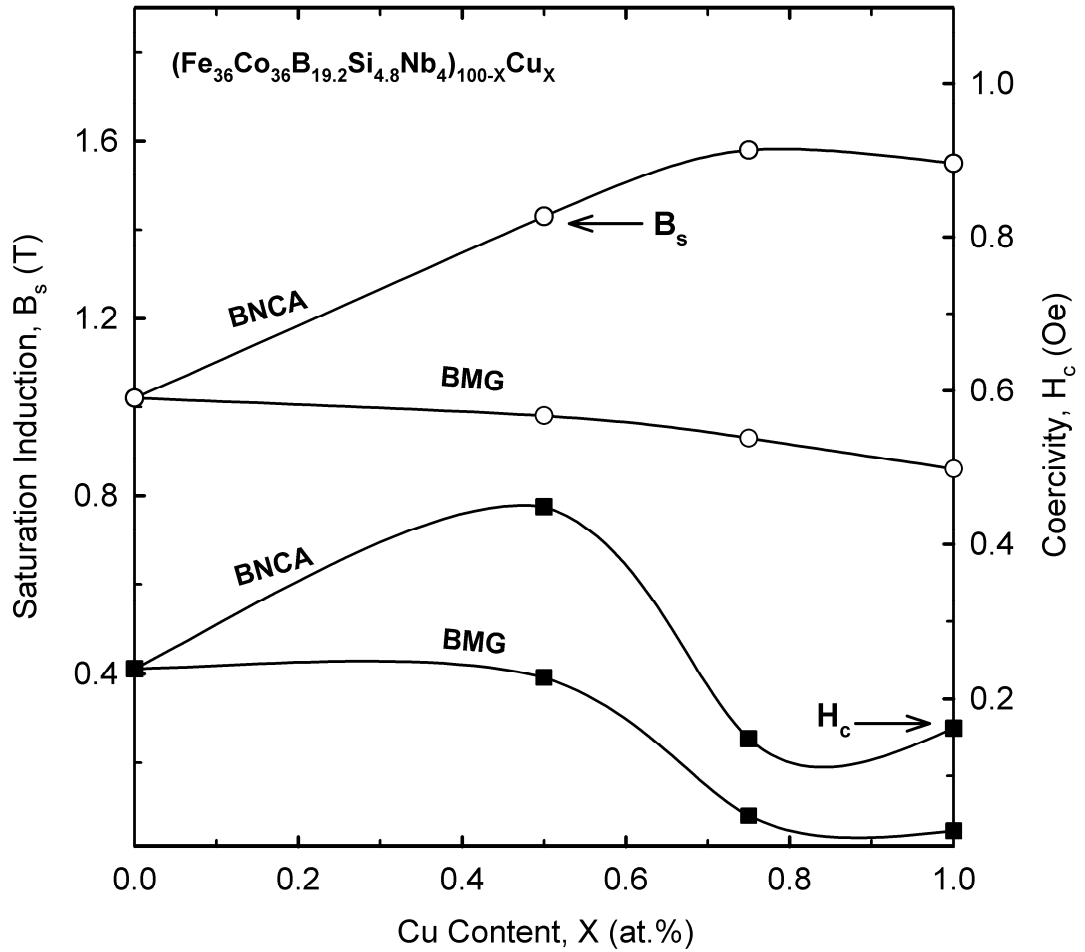


Figure 4.27 Variation of saturation induction (B_s) and coercivity (H_c) for as-cast; BMG and annealed; BNCA $(\text{Fe}_{36}\text{Co}_{36}\text{B}_{19.2}\text{Si}_{4.8}\text{Nb}_4)_{100-X}\text{Cu}_X$ alloys with Cu content.

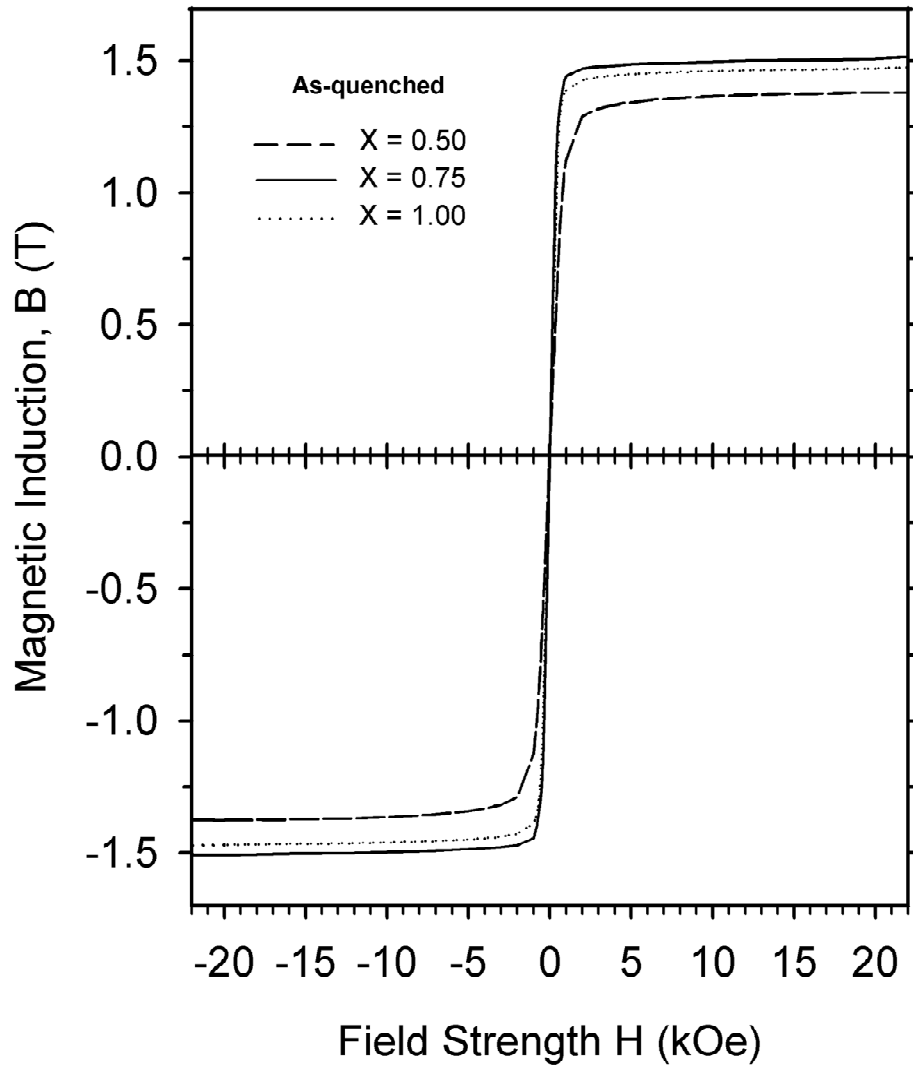


Figure 4.28 Hysteresis loops of as-quenched $(\text{Fe}_{36}\text{Co}_{36}\text{B}_{19.2}\text{Si}_{4.8}\text{Nb}_4)_{100-x}\text{Cu}_x$ bulk glassy alloys obtained without annealing, showing unexpectedly excellent magnetic behaviors.

A very interesting behavior is observed for the very thick sections of as-quenched BMGs, which showed unexpectedly good soft magnetic properties, much better than rest of the thinner sections as shown in Figure 4.28. These as-quenched BMGs showed saturation inductions of 1.37, 1.50 and 1.47 T, and coercivities of 0.003, 0.021 and 0.096 Oe in alloys of $X = 0.5, 0.75$ and 1 respectively. The B_s values are slightly lower than BNCA counterparts prepared by annealing the amorphous precursors but H_c 's are even better than them. However, since the formations of these regions cannot be controlled in current experimental setup, the BNCA's produced by annealing procedure are more dependable in terms of alloy reproducibility. Since these unexpected behaviors are unique to the thickest regions of the as-quenched samples, the only explanation possible is that during rapid solidification, ferromagnetic FeCo nanocrystals precipitated in the thickest sections of specimens, formed undetectable (via XRD) nanocrystallites, which sounds very attractive but is, however, very uncontrollable. This may also explain the decrease in coercivities, since below ~ 100 nm, coercivity decreases as nanocrystals get smaller [126]. This *direct casting into BNCA's* phenomenon should be studied in future, and may be subject to a detailed investigation, which would provide casting of super-soft magnets directly from alloy melts by high precision controlling of the cooling rates through the specimen cross-sections.

CHAPTER 5

BULK METALLIC GLASS FORMING ABILITY FROM TWO DIMENSIONAL PROJECTION MODEL

5.1. Introduction

The progress achieved in development of new metallic glasses, especially BMGs, has not been achieved yet in explaining the glass forming ability. There have been several recent studies concerning the interrelation between radial atomic distribution and high GFA BMGs structure [121, 127-129], putting on a new step but still very far from a final complete explanation. According to Hirata et al. [121], and as verified in this study, the first crystallization product of Fe-Co-Nb-B-Si BMG is a complex Fe_{23}B_6 -type crystal phase. They proposed that such a complex compound which also results in the development of such a complex MRO present in the amorphous phase in advance, promotes GFA. In addition to dealing with the crystallization products, the effect of alloying elements in the BMG on spatial arrangement of atoms in $\text{Fe}_{80}\text{B}_{20}$ (which is compositionally very close to Fe_{23}B_6 meta-stable phase) metallic glass is investigated in this chapter by applying the 2-D Projection Model.

5.2. Method of Calculating RDF from X-Ray Diffraction

An approximate method for handling an amorphous material containing more than one kind of atom is explained in this section. Some convenient unit of composition designated by uc , is chosen and the number of units of composition in the sample is given as N . The intensity is given by;

$$I_{eu} = \sum_m f^2 + \sum_m f^2 \sum_{m \neq n} e^{(2\pi i / \lambda)(\bar{s} - \bar{s}_o) \bar{r}_{mn}} \quad (5.1)$$

An average scattering factor per electron is defined as;

$$f_e = \frac{\sum_{uc} f_m}{\sum_{uc} Z_m} \quad (5.2)$$

where the sum over uc represents a sum over the atoms in the unit of composition and Z_m is the atomic number of the component m . The scattering factor is represented in terms of f_m by the relation;

$$f_m = K_m f_e \quad (5.3)$$

where K_m is called the effective electron numbers which will approximately be equal to the atomic numbers Z_m . The effective number K_m will vary somewhat with $\sin \theta / \lambda$ for each kind of atom and the approximation involves using an average and treating K_m as a constant for each kind of atom.

$$I'_{eu} = N \sum_{uc} f_j^2 + f_e^2 N \sum_{uc} K_j \int_0^{\infty} 4\pi r^2 [\rho_j(r) - \rho_e] (\sin Qr / Qr) dr \quad (5.4)$$

Let's define the total structure factor as;

$$S(Q) = (I'_{eu} / N - \sum_{uc} f_j^2) / f_e^2 \quad (5.5)$$

By using Equation (5.4) and inverting the Fourier integral, the following equation is obtained:

$$\sum_{uc} K_j 4\pi r^2 \rho_j(r) = 4\pi r^2 \rho_e \sum_{uc} K_j + (2r/\pi) \int_0^{\infty} QS(Q) \sin rQ dQ \quad (5.6)$$

If the intensity involves both the modified and unmodified scattering, the absolute units are obtained by dividing the experimental intensity curve by the proper polarization factor and then adjusting the scale of ordinates so that at large $\sin \theta / \lambda$ this curve oscillates above and below the independent scattering curve; $\sum_{uc} [f_j^2 + i_j(M)]$. The final curve; $\sum_{uc} K_j 4\pi r^2 \rho_j(r)$ represents the superposition of radial distribution functions for each kind of atom in the unit of composition. By this method, total radial distribution function $g(r)$ can be calculated.

The total RDFs like shown in Figure 5.2 was calculated by employing the corresponding X-Ray Diffraction Pattern shown in Figure 4.11 and, calculated structure factor in Figure 5.1.

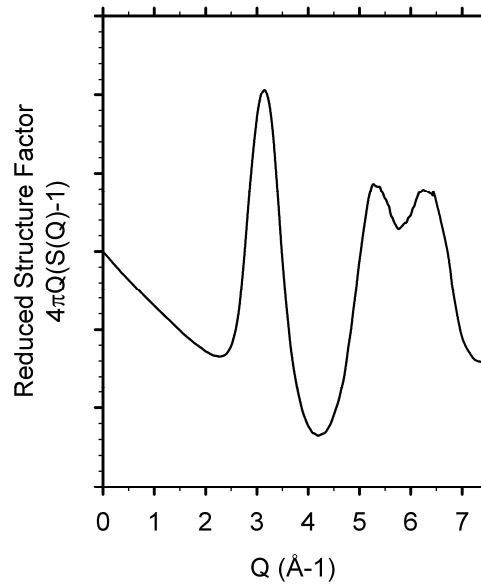


Figure 5.1 Total experimental reduced scattering factor for amorphous Fe-Co-Nb-B-Si alloy.

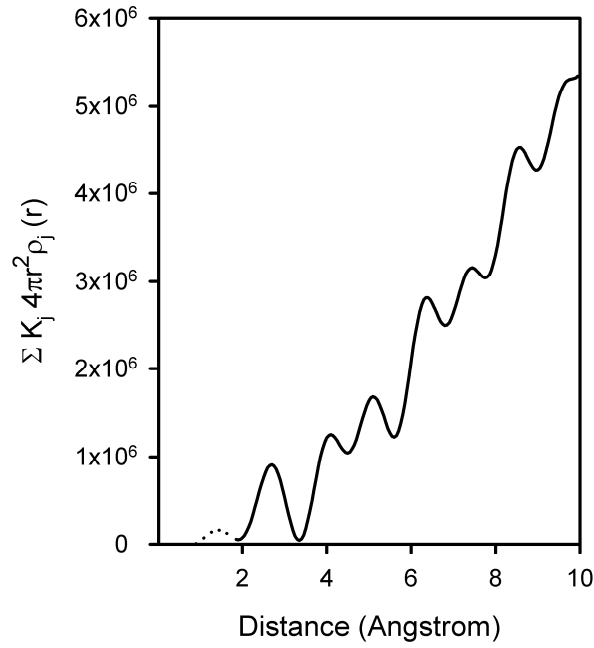


Figure 5.2 The Fourier-transformed $\sum_{uc} K_j 4\pi r^2 \rho_j(r)$ curve from which $g(r)$ can be extracted.

5.3. Results and Discussion

5.3.1. Origins of Bulk GFA

In Figure 5.3, total experimental RDFs of amorphous $\text{Fe}_{80}\text{B}_{20}$ and $\text{Fe}_{36}\text{Co}_{36}\text{B}_{19.2}\text{Si}_{4.8}\text{Nb}_4$ alloys are plotted with their radial difference $\Delta g(r)$ defined as;

$$\Delta g(r) = g_b(r) - g_a(r) \quad (5.7)$$

Where subscripts a and b denote $\text{Fe}_{80}\text{B}_{20}$ and $\text{Fe}_{36}\text{Co}_{36}\text{B}_{19.2}\text{Si}_{4.8}\text{Nb}_4$ (BMG) alloys respectively. The $\Delta g(r)$ function would allow making comments regarding topological effects of alloying elements that promoted GFA. In experimental RDF

of $\text{Fe}_{80}\text{B}_{20}$ there is a shoulder around 1.9 Å which showed up due to error introduced by transforming the $S(Q)$ to RDF, as a consequence of which the minimum of $\Delta g(r)$ around 1.9 Å is avoided during discussions and what is referred as the first minimum is the one around 2.5 Å.

The first two peaks (~2.2 and 2.8 Å) and the first minimum (~2.5 Å) in between these peaks in $\Delta g(r)$ arose due to broadening of first peak of BMGs RDF. Cobalt atoms definitely substitute for Fe atoms due to their very similar covalent atomic radii. Consequently, broadening of the first peak is due to nearest neighbor TMs; Fe-Co, Fe-Nb and Co-Nb. The second minimum in $\Delta g(r)$ which is around 3.2 Å shows that first neighbor coordinations are defined better in BMG which is an expected result.

A tricky problem is to identify the compacting effect of Nb and Si atoms on the first second peak (first peak of the splitted peak, around 4.2 Å) of the RDF. As shown previously with 2-D Projection Model, second peak of the RDF (first splitted peak) is dominated by interclusteral pentagonal linings of TP units. A positional change in this peak is quite important since it indicates the presence of a modification in structural units. In Figure 5.3, none of the peaks other than this first splitted peak show positional variation which shows that the effect of GFA elements in BMG is mainly on outset of MRO. This is quantified by the third maximum of $\Delta g(r)$ around ~3.7 Å and the following minimum.

Besides the broadening effect of Co, Nb and Si on the first peak which provides clues about their influence only on SRO, they strongly altered the MRO and somehow this fact improved GFA to form BMG. According to 2-D Projection Model, to provide pentagonal diagonal squeezes to reveal the shift of first splitted peak of BMG to lower distances relative to $\text{Fe}_{80}\text{B}_{20}$, Nb atom may be replacing two neighboring Fe atoms or a single Si atom may be replacing a single Fe atom. When Nb replaces two of five Fe atoms on a nearly flat pentagon of TP, internal angles become narrower and such a squeeze in RDF can appear. Thus, in addition to

slowing down atomic diffusion in the liquid state, Nb atoms allow a more efficient compaction of TP-clusters together. By doing so, Nb atoms might be uniting two TP units and result in formation of larger 5-fold symmetrical clusters that can move/translate much harder than single TP units. Nb may have merged the tetrahedral holes at TP junctions into facets by replacing two Fe atoms. By the same way as Nb, when Si replaces an Fe atom on nearly flat pentagons of TP, it may provide a similar squeeze since Si atom is significantly smaller than Fe atom but its uniting effect seems less probable. Although Si atom is larger than B atom, it may also replace B in several TP units and result in homogenously dispersed deformations which again favors compaction (or efficiency of filling 3D space) preserving the 5-fold symmetry.

Since the second peak of the splitted peak ($\sim 5.0 \text{ \AA}$) did not shift considerably relative to binary Fe-B, the co-planarity of the pentagons of united TP's did not change because that peak is mainly due to relation of unshared atoms of TPs via P-P mode. Those unshared atoms became slightly more separated as an expected compensation for local compaction.

The presence of a more compact MRO is supported by the fact that in $\text{Fe}_{36}\text{Co}_{36}\text{B}_{19.2}\text{Si}_{4.8}\text{Nb}_4$ alloys, the alloying additions alter the first crystallization product from $\alpha\text{-Fe}$ to Fe_{23}B_6 crystal (See Sections 4.5.3 and 4.5.4). If such a complex crystal requiring a long range atomic diffusion is to nucleate as the first crystallization product, the developed MRO is expected to bear symmetries similar to that crystal and pretend to be a nucleation precursor. Uniting the TPs, Nb may allow development of such a MRO which would form the basis for such a complex meta-stable product to nucleate upon crystallization. These findings are supported by studies concerning the primary crystallization of Fe-Nb-B and Fe-Co-Nb-B-Si alloys [121, 122].

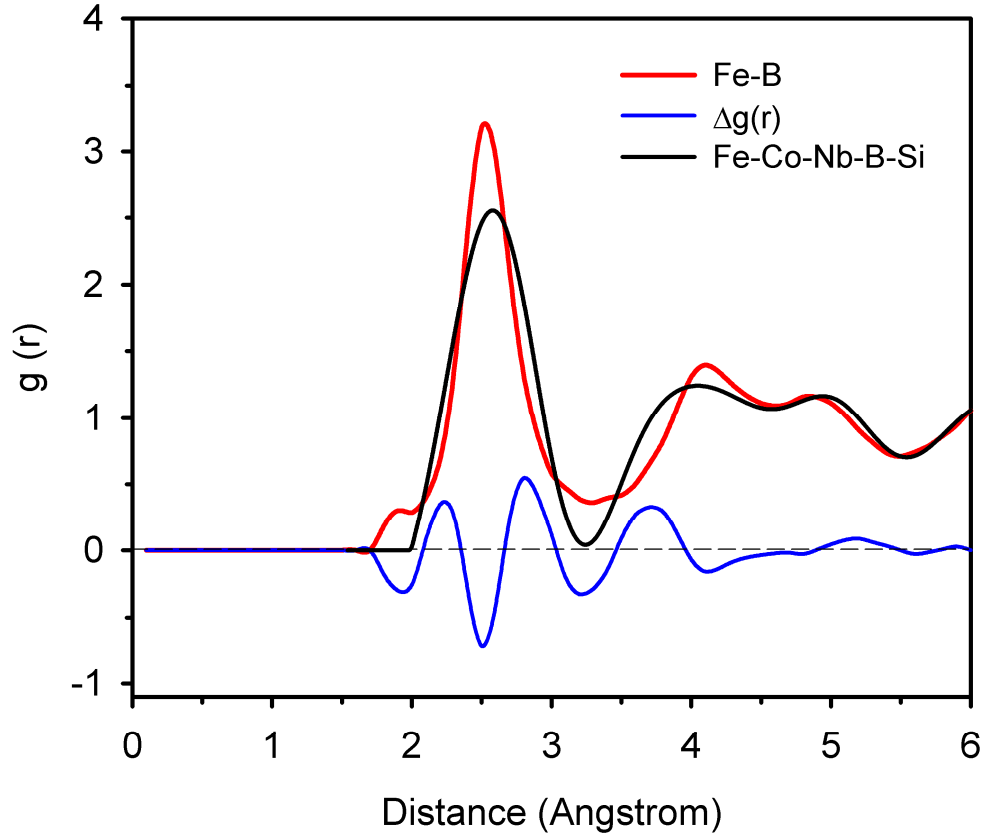


Figure 5.3 Total experimental RDFs of amorphous $\text{Fe}_{80}\text{B}_{20}$ and $\text{Fe}_{36}\text{Co}_{36}\text{B}_{19.2}\text{Si}_{4.8}\text{Nb}_4$ alloys and their radial difference $\Delta g(r)$.

5.3.2. Effect of Precipitation of Fe_{23}B_6 -type Phase on RDF of BMG

The proposed resemblance of as-developed MRO in $\text{Fe}_{36}\text{Co}_{36}\text{B}_{19.2}\text{Si}_{4.8}\text{Nb}_4$ to Fe_{23}B_6 -type meta-stable phase would be determined via comparison of RDFs of as-quenched and annealed $\text{Fe}_{36}\text{Co}_{36}\text{B}_{19.2}\text{Si}_{4.8}\text{Nb}_4$ alloys as in Figure 5.4. The precipitation of $(\text{Fe, Co, Nb})_{23}\text{B}_6$ phase in annealed alloy did not yield a significant change in RDF peak positions at the second coordination sphere showing that the MRO in the alloy corresponds to that of $(\text{Fe, Co, Nb})_{23}\text{B}_6$. Annealing sharpened the

third coordination (around 6.5 Å) and provided a division of the peak around 8.5 Å to two well defined coordination spheres at ~8 and ~9 Å. All of these prove that the MRO in as-quenched amorphous alloy is quite similar to $(\text{Fe, Co, Nb})_{23}\text{B}_6$ and after annealing and precipitation of $(\text{Fe, Co, Nb})_{23}\text{B}_6$, the onset of MRO stays the same, and higher coordination spheres become well defined since the previous MRO is now extended to at least to the ranges of large lattice parameter of $(\text{Fe, Co, Nb})_{23}\text{B}_6$ determined previously as 1.0602 nm in Section 4.5.4.1.

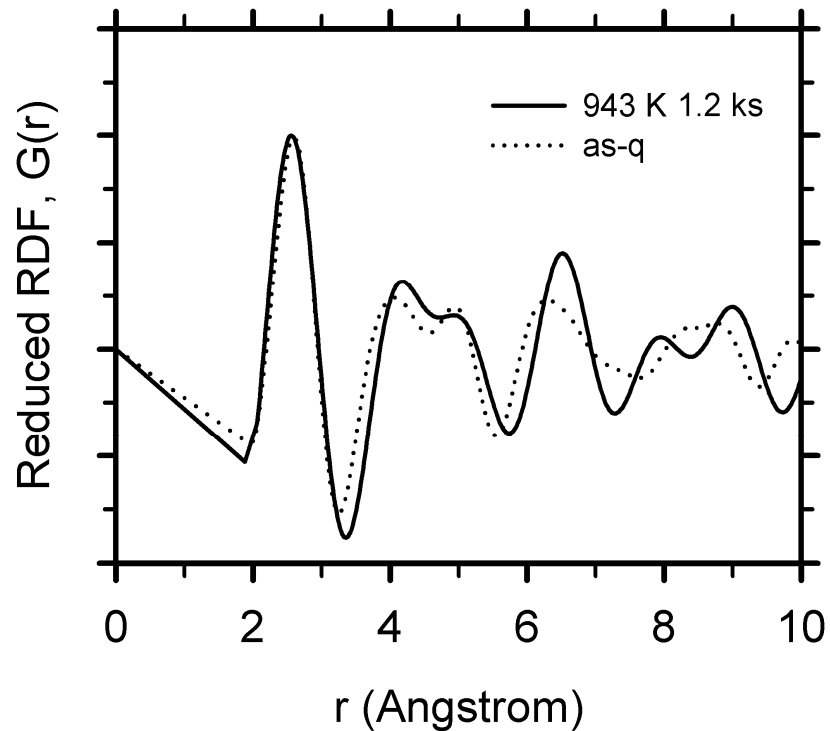


Figure 5.4 Reduced RDFs, i.e. $G(r)$'s of as quenched and annealed $\text{Fe}_{36}\text{Co}_{36}\text{B}_{19.2}\text{Si}_{4.8}\text{Nb}_4$ base alloy.

5.3.3. Effect of Cu on RDF of BMG

$G(r)$'s of bulk amorphous $(\text{Fe}_{36}\text{Co}_{36}\text{B}_{19.2}\text{Si}_{4.8}\text{Nb}_4)_{100-x}\text{Cu}_x$ alloys are plotted in Figure 5.5, which shows the evolution of as-quenched structure with increasing copper content. In the amorphous state, with the presence of Cu in solution, structural gains occur starting from the second coordination sphere and extend to higher separations also. Since the onset of MRO is attributed to a Fe_{23}B_6 like order and did not alter with its precipitation previously in Section 5.3.2, Cu atoms modify atomic structures of these Fe_{23}B_6 embryos making up the local structure. Unlike Nb, Cu yields no compaction at the onset of MRO and is not expected to yield an improvement in GFA topologically. This is supported by the fact that it changes the primary crystallization product from complex Fe_{23}B_6 to BCC-FeCo phase and lowers the onset of crystallization temperature. In contrast, the MRO onset shifts to higher separations in the range of 4.0 – 4.3 Å worsening the local compaction. The sharpening effect on peaks at 6.5 and 8.5 Å, and development of new coordination peaks at ~7.5 Å are due to altering of the MRO to a more BCC-like symmetry with Cu addition to solution. This becomes more clarified and apparent in next section dealing with precipitation of BCC-FeCo in the amorphous matrix.

5.3.4. Radial Investigation of Nanocrystallization of FeCo

What was referred as bulk nanocrystalline alloy is of course a phase mixture of amorphous matrix and as-precipitated nanocrystals embedded in it. The trace of the BCC α -FeCo nanocrystals can readily be observed via their modifications on RDFs as given in Figure 5.6. According to the BCC profile provided (marked as sample-bcc) in the same graph, the deviations of radial spacings of bulk nanocrystalline alloys from the corresponding bulk glassy alloys strictly correspond to a precipitated BCC crystals. After crystallization, a shoulder appeared near the first peak of the RDF, corresponding to the second nearest neighbor separation in BCC lattice, the slight shifting of which to right of which is due to the limited

attainability of structural detail of $S(Q)$ in high Q with available XRD instrument. Following spacings are more accurate since enough detail in $S(Q)$ is available in low Q regions. Another significant contribution is done to the third peaks (second sub-peaks of the splitted peaks) of the RDFs due to fourth coordination sphere of BCC. All following intense neighboring coordination spheres of BCC nanocrystals can be traced also from the corresponding distances on RDFs by proportional structure gains at those atomic separations. When these structural gains are considered and assumed to be related to amount of the crystal phase, the material with 0.75 at.% Cu addition seems to have a higher proportion of α -FeCo nanocrystals precipitated relative to 1.00 at.% Cu alloy.

5.3.5. Investigations on Φ Values

In Table 5.1, r_2/r_1 (from hereafter, this ratio will be cited within the text as Φ) ratios of several metallic glasses with different kinds are listed. First, it could readily be seen that all Φ values are slightly higher than the golden mean (~ 1.618) and seems to approach it with increasing GFA in the corresponding BMG system. Although such a relation can be observed in a metallic glass system, there is no obvious correlation covering all different kinds of metallic alloys. This might be due to the fact that the precision of calculations are not able to reproduce universally comparable Φ values. Consequently, comparing RDFs reported in same studies are more dependable in terms of Φ comparisons. For example, as listed in Table 5.1, Φ values found in this study and extracted from [101] in for Fe-Co-Nb-B-Si alloy are not much close but Φ values of Alloy 2 (the higher GFA alloy in a given system) are always lower than that of corresponding Alloy 1 (the lower GFA alloy in that system). These results indicate that lower the Φ is, higher is the GFA of an alloy in a given metallic glass system.

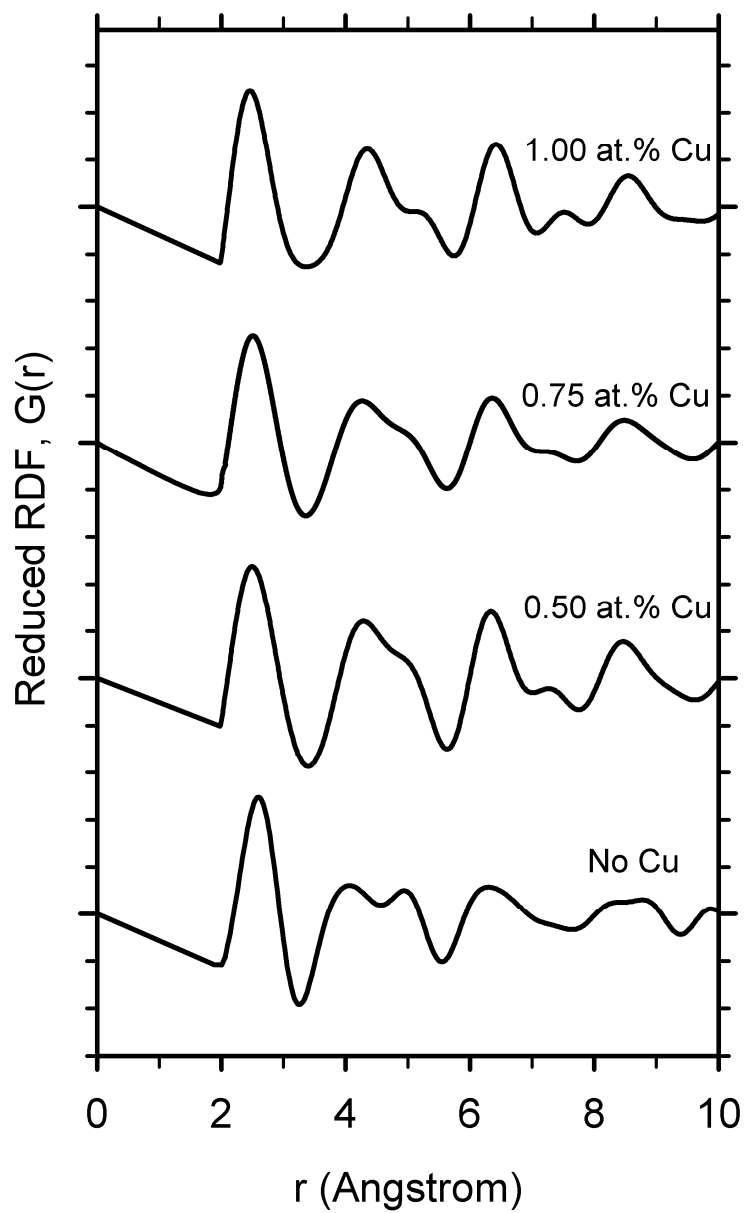


Figure 5.5 Reduced RDFs, i.e. $G(r)$'s of bulk amorphous alloys of $(\text{Fe}_{36}\text{Co}_{36}\text{B}_{19.2}\text{Si}_{4.8}\text{Nb}_4)_{100-X}\text{Cu}_X$, where X ranges between 0 and 1.

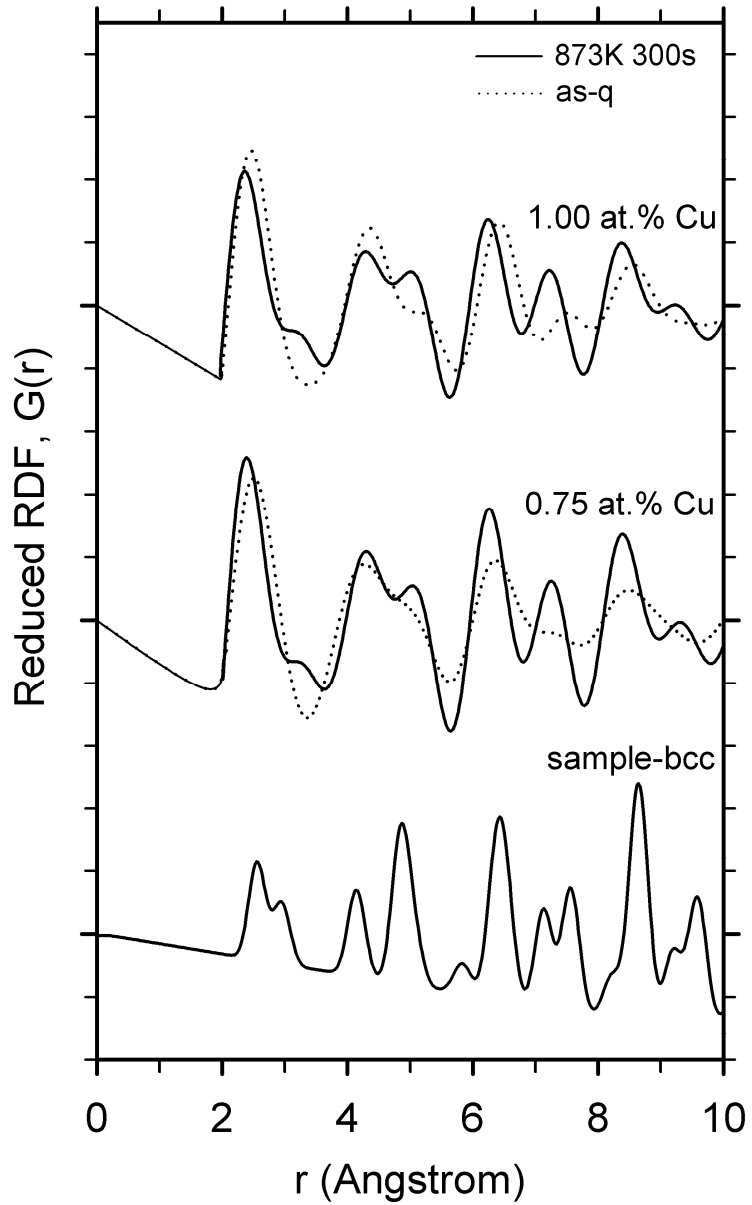


Figure 5.6 Reduced RDFs, i.e. $G(r)$'s of bulk nanocrystalline alloys of $(\text{Fe}_{36}\text{Co}_{36}\text{B}_{19.2}\text{Si}_{4.8}\text{Nb}_4)_{100-X}\text{Cu}_X$, where X is 0.75 and 1.00, are compared to $G(r)$'s their corresponding bulk glassy precursors. The lowest graph is a sample BCC $G(r)$ adjusted to a lattice parameter that would yield a first separation distance equal to first peak of given RDFs.

Table 5.1 The r_2/r_1 ratios (Φ values) of several metallic glasses reported. If Alloy 2 is present, it refers to the alloy with higher GFA and compositions of the alloys are given in the order of Alloy 1 and Alloy 2. If Φ ratio was not readily calculable from provisions of the authors of corresponding reference, it was reproduced from RDFs they provided.

Φ (Alloy 1)	Φ (Alloy 2)	Compositions of Alloys	Reference
1.653	1.639	Pd ₄₀ Ni ₄₀ P ₂₀ and Pd _{42.5} Ni _{7.5} Cu ₃₀ P ₂₀	[130]
1.659		Pd ₄₀ Ni ₄₀ P ₂₀	[127]
1.643		Pd ₄₀ Ni ₁₀ Cu ₃₀ P ₂₀	[131]
1.685	1.651	Pd ₄₀ Ni ₄₀ P ₂₀ and Pd ₄₀ Ni ₁₀ Cu ₃₀ P ₂₀	[96]
1.680		Aluminum	[68]
1.726		Ni ₃ Al	[132]
1.667		Re ₈₂ Tb ₁₈	[133]
1.676		Mg ₆₅ Cu ₂₅ Y ₁₀	[134]
1.635		Cu ₇₀ Zr ₃₀	[135]
1.717	1.697	Zr ₇₀ Cu ₂₀ Ni ₁₀ and (Zr ₇₀ Cu ₂₀ Ni ₁₀) _{0.96} Ta _{0.04}	[136]
1.730	1.636	Fe ₈₄ Nb ₇ B ₉ and Fe ₇₀ Nb ₁₀ B ₂₀	[59]
1.667		(Fe _{0.5} Co _{0.5}) ₇₂ B ₂₀ Si ₄ Nb ₄	[121]
1.680	1.620	Fe ₈₀ B ₂₀ and (Fe _{0.5} Co _{0.5}) ₇₂ B ₂₀ Si ₄ Nb ₄	This study

The compaction effect can also be imitated by application of high pressure (HP). Qi and co-workers recently studied the effect of HP on Pd-Ni [137] and Cu-Ag [138] metallic glass by MD simulation. When Φ values are calculated from their reported r_1 and r_2 and plotted against pressure as in Figure 5.7, it can be seen that with increasing pressure Φ decreases. The experimental data points are fitted to an exponential decay function, $\Phi(P) = y_0 + a \exp(-bP)$ (where P is pressure and, y_0 , a and b are fitting constants) and extrapolation of fitting functions is done to higher pressures. After extrapolating the functions that calculated data are fitted to, Φ approaches golden mean at high pressures. This result is readily available also from y_0 values of decay functions (1.6191 and 1.6186 for Pd-Ni and Cu-Ag respectively),

since at infinite pressure, they converge to y_0 . Consequently, the effect induced by the alloying elements as Nb (See Section 5.3.1), is indirectly the same as applying an external pressure; thus, creating an internal atomic pressure to compact the local structural units or merge them together.

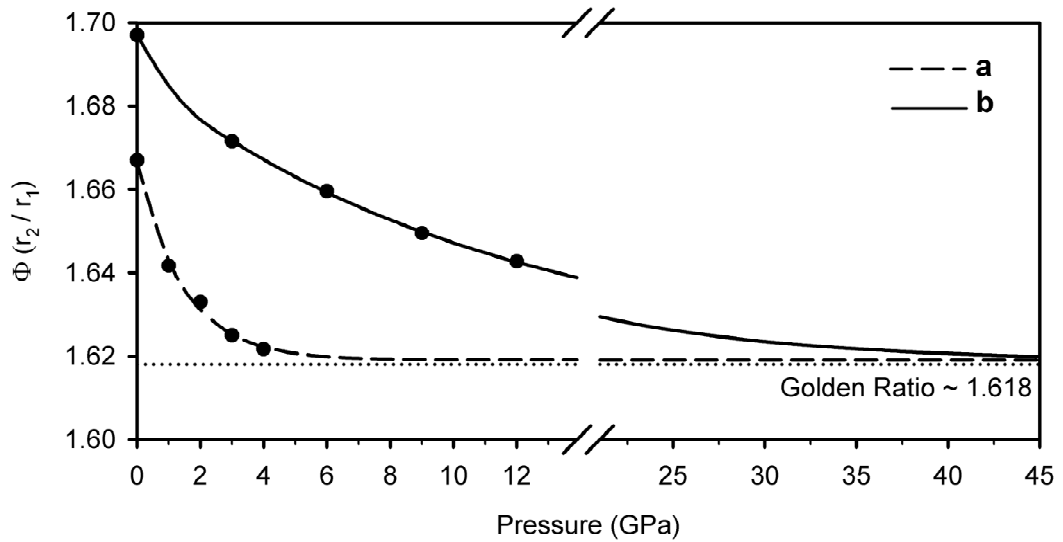


Figure 5.7 Φ versus pressure plots of (a) Pd-Ni and (b) Cu-Ag calculated after studies [137] and [138] respectively.

In summary, the compaction effect induced by elements increasing GFA, would directly be quantified by Φ ratios of the corresponding RDFs, with keeping in mind the conclusions drawn are only qualitative. In a system of metallic glass, when GFA increases, Φ decreases, indicating that a compaction around the onset of MRO occurred. This can be observed in all reference systems with two alloys, given in Table 5.1.

CHAPTER 6

CONCLUSIONS

This study aimed at combining theoretical and experimental studies to contribute to revealing the phenomenon behind the glass forming ability of TM-M metallic glasses by specifically sampling Fe-B system and its relation with structure of the alloy.

In the theoretical part, a detailed structural identification of amorphous TM-M alloys via specifically sampling Fe-B binary is established. The route followed was briefly identifying the small to large structural arguments by analyzing SRO, polyhedra, clusters and cluster orderings revealing MRO. A map of nano-scale phase-separated structure can be formed as:

- Pure Fe contours of ~ 0.72 nm thickness form a continuous network and separate the structure into B containing domains. They are interlocked with surrounding B-centered prisms via triangular facet sharing and tetrahedral stellations.
- Pure Fe-clusters of ~ 0.92 nm diameter perturbing into domains from Fe-contours are observed when Fe content is increased from 80 to 83 at.%. They have no stellations.
- There exist Fe rich regions in domains with mostly bcc symmetries under excessive deformations due to high amount (~ 9 at.%) of dissolved B. The probable formation mechanism is simultaneously progressing incomplete

Mackay and Bain transformations. B atoms are substitutionally participating to this deformed bcc matrix.

- B-centered TPs display no order in large spacings. However, they tend to form domains of high coordinations and low coordinations. Locally, these prismatic units form polytetrahedral aggregates involving pentagonal prisms in addition to icosahedral symmetry structures making up the atomic MRO. The regions of low coordinated B-centered TPs allow the extension of deformed-bcc regions to propagate several atomic coordinations.

After resolving Fe-Fe and Fe-B RDFs and compiling previously gathered topological information into a 2-D projection model, RDF peak positions from short to medium ranges are well estimated. The first and second sub-peaks of the “splitted” peak in Fe-Fe RDF are found to be due to local pentagonal intra-TP linings of Fe atoms and ordering of these TP clusters respectively. Model predicts the positions of these sub-peaks as roughly Φ (golden ratio) and $\sqrt{\Phi + 2}$ times NN interatomic Fe-Fe distance. Splitting in Fe-B RDF is found to be a matter of tetrahedral TP ordering and locations of peaks are defined by the 2-D projection modes.

It is known that, in addition to other consequences, rapid solidification can highly widen solubility regions. Finding whether metallic glass formation is an extremity of this situation or not, requires further investigations. Whether it is a meta-stable macroscopically single phase that can dissolve all the constituent atoms should be further studied. However, with this study, it has been shown that there is also a threshold in atomic scale for infinite solubility, since primary-eutectic like regions (perturbations) are observed.

After successfully producing 3 mm thick Fe-Co-Nb-B-Si and Fe-Co-Nb-B-Si bulk amorphous and bulk nanocrystalline alloys via a completely conventional route, the

contribution of alloying elements to GFA relative to the Fe-B binary and nanocrystallization process are discussed by spatial analysis and the developed 2-D Projection Model. Several conclusions are drawn as;

- Replacing two Fe atoms on a pentagonal lining of a TP unit, Nb atoms result in local compactations at the onset of MRO, merge two TP units into one and build up clusters that would translate much harder upon cooling, as a consequence of which, promote GFA. Si atoms may also cause such compactations when substituted for a single Fe atom, since they have smaller atomic radius relative to Fe atoms
- The ratio of the second peak (first sub-peak of the splitted peak) to the first peak of the total RDF, cited as Φ , is found to be an indication of medium range compaction and resulting increase of GFA in a given metallic glass system. It was found that, Φ is not confined to TM-M alloys and is applicable to a variety of other metallic glasses.
- The RDFs of amorphous precursors possess traces of all coordinations of to-be-precipitated nanocrystal prior to nanocrystallization. After the crystallization process, significant structural gains occur in RDF peaks at spacings corresponding to coordination spheres of precipitated nano-scale crystalline phase.

REFERENCES

- [1] W. Klement, R. H. Willens, P. O. L. Duwez, *Nature* 187 (1960) 869.
- [2] T. R. Anantharaman, Trans Tech Publications (1984).
- [3] R. Pond, R. Maddin, *TMS-AIME* 245 (1969) 2475.
- [4] R. W. Cahn, *Physical Metallurgy*, Elsevier Science Publishers B.V. (1983).
- [5] P. Duwez, S. C. H. Lin, *J. Appl. Phys.* 38 (1967) 4096.
- [6] A. I. Gubanov, *Fizika* 2 (1960) 502.
- [7] S. Zallen, *The physics of amorphous solids*, Wiley, (1983).
- [8] C. H. P. Lupis, *Chemical Thermodynamics of Materials*, Wiley, (1983).
- [9] H. S. Chen, D. Turnbull, *Chem. Phys.* 48 (1968) 2560.
- [10] D. Turnbull, M. H. Cohen, *Chem. Phys.* 34 (1961) 120.
- [11] D. Turnbull, M. H. Cohen, *Chem. Phys.* 52 (1970) 3038.
- [12] J. H. Gibbs, E. A. DiMarzio, *Chem. Phys.* 28 (1958) 373.
- [13] W. Kauzmann, *Chem. Rev.* 43 (1948) 219.
- [14] X. Y. Yan, Y. A. Chang, Y. Yang, F. X. Xie, S. L. Chen, F. Zhang, S. Daniel, M. H. He, *Intermetallics* 9 (2001) 535.
- [15] D. Kim, B. J. Lee, N. J. Kim, *Intermetallics* 12 (2004) 1103.

- [16] J. D. Verhoeven, *Fundamentals of Physical Metallurgy*, Wiley and Sons, (1975).
- [17] D. Turnbull, *Contemp. Phys.* 10 (1969) 473.
- [18] W. Kurz, D. H. Fisher, *Fundamentals of Solidification*, Trans Tech Publications (1992).
- [19] H. A. Davies, J. Aucote, J. B. Hull, *Scripta Met.* 8 (1974) 1179.
- [20] H. A. Davies, *J. Non-cryst. Solids* 17 (1975) 266.
- [21] A. Takeuchi, A. Inoue, *Mater. Sci. Eng. A.* 304-306 (2001) 446.
- [22] A. Inoue, *Mater. Trans. JIM* 36 (1995) 866.
- [23] J. L. Finney, *J. Physique Colloque* 36 (1975) C2 1.
- [24] S. Takayama, *J. Mater. Sci.* 70 (1976) 164.
- [25] T. Egami, Y. Waseda, *J. Non-Cryst. Solids* 64 (1984) 113.
- [26] Z. P. Lu, H. Tan, Y. Li, *Scripta Mater.* 42 (2000) 667.
- [27] Z. P. Lu, Y. Li, S. C. Ng, *J. Non-cryst. Solids* 270 (2000) 103.
- [28] H. S. Chen, *Rep. Prog. Phys.* 43 (1980) 353.
- [29] A. Inoue, T. Nakamura, N. Nishiyama, T. Masumoto, *Mater. Trans. JIM* 33 (1990) 937.
- [30] Z. P. Lu, C. T. Liu, *Intermetallics* 12 (2004) 1035.
- [31] T. Egami, *Mater. Sci. Eng. A.* 226-228 (1997) 261.

- [32] T. Egami, *Intermetallics* 14 (2006) 882.
- [33] D. B. Miracle, O. N. Senkov, *Mater. Sci. Eng. A* 347 (2003) 50.
- [34] T. Egami, *J. Non-cryst. Solids* 205-207 (1996) 575.
- [35] H. J. Lee, T. Cagin, W. L. Johnson, W. A. Goddard, *J. Chem. Phys.* 119 (2003) 9858.
- [36] B. C. Giessen, C. N. J. Wagner In: S. Z. Beer, Editor, *In Liquid Metals – Physics and Chemistry*, Dekker, New York (1972).
- [37] D. E. Polk, B. C. Giessen In: J. J. Gilman and H. J. Leamy, Editors, *In Metallic Glasses*, American Society for Metals, Metals Park, Ohio (1978).
- [38] J. L. Finney, *Nature* 266 (1977) 309.
- [39] P. H. Gaskell, *Nature* 276 (1978) 484.
- [40] P. H. Gaskell, *J. Non-Cryst. Solids* 32 (1979) 207.
- [41] J. M. Dubois, G. Le Caer, *J. Phys. Colloq.* 43 (1982) 67.
- [42] J. M. Dubois, P. H. Gaskell, G. Le Caer, *Proc. R. Soc. A* 402 (1985) 323.
- [43] H. Hermann, N. Mattern, *J. Phys. F* 16 (1986) 131.
- [44] D. B. Miracle, W. S. Sanders, O. N. Senkov, *Phil. Mag. A* 83 (2003) 2409.
- [45] D. B. Miracle, *Nature Mater.* 3 (2004) 697.
- [46] E. Nold, O. Lamparter, H. Olbrich, G. Rainer-Harbach, S. Steeb, *Z. Naturforsch Teil A* 36 (1981) 1032.

- [47] E. J. Hiltunen, J. A. Lehto, L. Takacs, *Phys. Scr.* 34 (1986) 239.
- [48] P. Lamparter, W. Sperl, S. Steeb, J. Bletry, *Z. Naturforsch Teil A* 37 (1982) 1223.
- [49] P. Lamparter, S. Steeb, *Proc. 5th Conf. on Rapidly Quenched Metals*, North-Holland 1985, Wilzburg (1984).
- [50] T. Fukunaga, K. Suzuki, *Sci. Rep. Res. Inst. Tohoku Univ. A* 29 (1981) 153.
- [51] T. A. Weber, F. H. Stillinger, *Phys. Rev. B* 31 (1985) 1954.
- [52] C. Hausleitner, J. Hafner, *Phys. Rev. B* 47 (1993) 5689.
- [53] C. Hausleitner, J. Hafner, C. Becker, *Phys. Rev. B* 48 (1993) 13119.
- [54] H. W. Sheng, W. K. Luo, F. M. Alamgir, J. M. Bai, E. Ma, *Nature* 439 (2006) 419.
- [55] P. Ganesh, M. Widom, *Phys. Rev. B* 77 (2008) 014205.
- [56] T. Ohkubo, H. Kai, Y. Hirotsu, *Mater. Sci. Eng. A* 304-306 (2001) 300.
- [57] A. Hirata, Y. Hirotsu, T. Ohkubo, T. Hanada, V. Z. Bengus, *Phys. Rev. B* 74 (2006) 214206.
- [58] Y. Hirotsu, T. Ohkubo, M. Matsushita, *Microsc. Res. Tech.* 40 (1998) 284.
- [59] A. Hirata, Y. Hirotsu, T. Ohkubo, E. Matsubara, A. Makino, *J. Microsc. – Oxf.* 223 (2006) 191.
- [60] T. Ohkubo, Y. Hirotsu, *Phys. Rev. B* 67 (2003) 094201.
- [61] T. Hamada, F. E. Fujita, *Jpn. J. Appl. Phys.* 25 (1986) 318.

- [62] F. C. Frank, *Proc. R. Soc. A* 215 (1952) 43.
- [63] P. Ganesh, M. Widom, *Phys. Rev. B* 74 (2006) 134205.
- [64] D. W. Qi, S. Wang, *Phys. Rev. B* 44 (1991) 884.
- [65] J. D. Honeycutt, H. C. Andersen, *J. Phys. Chem.* 91 (1987) 4950.
- [66] I. R. McDonald, *Mol. Phys.* 23 (1972) 41
- [67] F. F. Abraham, *Phys. Rev. Lett.* 44 (1980) 463.
- [68] K. J. Smolander, *Phys. Scripta* 31 (1985) 427.
- [69] A. M. Bratkovsky, A. V. Smirnov, *J. Phys. Condens. Matter.* 3 (1991) 5153.
- [70] A. M. Bratkovsky, A. V. Smirnov, *Phys. Rev. B.* 48 (1993) 48.
- [71] N. P. Bailey, J. Schiotz, K. W. Jacobsen, *Phys. Rev. B.* 69 (2004) 69.
- [72] D. K. Belashchenko, G. F. Syrykh, *Inorganic Mater.* 40 (2004) 83.
- [73] L. Qi, H. F. Zhang, Z. Q. Hu, *Intermetallics* 12 (2004) 1191.
- [74] Q. Zhang, W. S. Lai, B. X. Liu, *J. Non-cryst. Solids* 261 (2000) 137.
- [75] Y. Qi, T. Cagin, Y. Kimura, W. A. Goddard, *Phys. Rev. B.* 59 (1999) 3527.
- [76] S. Trebst, E. Gull, M. Troyer, *J. Chem. Phys.* 123 (2005) 204501.
- [77] M. Matsumoto, T. Nishimura, *ACM Trans. Model. Comput. Simul.* 8 (1998) 3.
- [78] J. Hafner, *J. Phys. F: Met. Phys.* 12 (1982) 1205.

- [79] R. Harris, L. J. Lewis, *J. Phys. F: Met. Phys.* 13 (1983) 1359.
- [80] G. S. Cargill, F. Spaepen, *J. Non-Cryst. Solids* 43 (1981) 91.
- [81] M. Tucker, D. Keen, RMC homepage, <http://www.isis.rl.ac.uk/RMC/>, last accessed 13 May 2008.
- [82] A. A. Katsnelson, A. O. Mekhrabov, V. M. Silonov, *Fiz. Metal. Metalloved.* 52 (1981) 661.
- [83] A. O. Mekhrabov, M. Doyama, *Phys. Status Solidi B* 126 (1984) 453.
- [84] A. O. Mekhrabov, Z. M. Babaev, K. A. A., Z. A. Matysina, *Fiz. Metal. Metalloved.* 61 (1986) 1089.
- [85] A. O. Mekhrabov, A. Ressayoglu, T. Ozturk, *Journal of Alloys and Compounds* 205 (1994) 147.
- [86] A. O. Mekhrabov, M. V. Akdeniz, M. M. Arer, *Acta Materialia* 45 (1997) 1077.
- [87] M. V. Akdeniz, A. O. Mekhrabov, *Acta Materialia* 46 (1998) 1185.
- [88] A. O. Mekhrabov, M. V. Akdeniz, *Acta Mater.* 47 (1999) 2067.
- [89] A. O. Mekhrabov, M. V. Akdeniz, *Model. Simul. Mater. Sci. Eng.* (2007) 1.
- [90] J. Hubbard, *Proc. R. Soc. A* 240 (1957) 359.
- [91] A. O. E. Animalu, *Phys. Rev. B* 8 (1973) 3542.
- [92] T. Fujiwara, H. S. Chen, Y. Waseda, *J. Phys. F: Met. Phys.* 6 (1981) 1325.
- [93] G. Rollmann, M. E. Gruner, A. Hucht, R. Meyer, P. Entel, M. L. Tiago, J. R. Chelikowsky, *Physical Review Letters* 99 (2007) 083402.

- [94] M. Torres, G. Pastor, I. Jimenez, J. Fayos, *Phylos. Mag. Lett.* 59 (1989) 181.
- [95] A. Cai, G. Sun, Y. Pan, *Mater. Design* 27 (2006) 479.
- [96] A. Inoue, *Acta Mater.* 48 (2000) 279.
- [97] A. Inoue, J. S. Gook, *Mater. Trans. JIM* 36 (1995) 1180.
- [98] A. Inoue, T. Zhang, A. Takeuchi, *Appl. Phys. Lett.* 71 (1997) 464.
- [99] T. D. Shen, R. B. Schwarz, *Appl. Phys. Lett.* 75 (1999) 49.
- [100] A. Inoue, B. Shen, *Mater. Sci. Eng. A* 375-377 (2004) 302.
- [101] B. Shen, A. Inoue, C. Chang, *Appl. Phys. Lett.* 85 (2004) 4911.
- [102] P. Pawlik, H. A. Davies, M. R. J. Gibbs, *Mater. Sci. Eng. A* 375-377 (2004) 372.
- [103] A. Inoue, R. E. Park, *Mater. Trans. JIM* 37 (1996) 1715.
- [104] K. Pekala, J. Latuch, T. Kulik, J. Antonowicz, P. Jaskiewicz, *Mater. Sci. Eng. A* 375-377 (2004) 377.
- [105] H. Koshiba, A. Inoue, A. Makino, *Nanostructured Mat.* 8 (1997) 997.
- [106] A. Inoue, T. Zhang, H. Koshiba, A. Makino, *J. Appl. Phys.* 83 (1998) 6326.
- [107] C.-Y. Lin, H.-Y. Tien, T.-S. Chin, *Appl. Phys. Lett.* 86 (2005) 162501.
- [108] Y. Yoshizawa, S. Oguma, K. Yamauchi, *J. Appl. Phys.* 64 (1988) 6044.
- [109] Y. Yoshizawa, K. Yamauchi, T. Yamane, H. Sugihara, *J. Appl. Phys.* 64 (1988) 6047.

- [110] U. Köster, J. Meinhardt, *Mater. Sci. Eng. A*. 178 (1994) 271.
- [111] T. H. Noh, W. K. Pi, H. J. Kim, I. K. Kang, *J. Appl. Phys.* 69 (1991) 5921.
- [112] T. H. Noh, M. B. Lee, H. J. Kim, I. K. Kang, *J. Appl. Phys.* 67 (1990) 5568.
- [113] J. Zbroszczyk, K. Narita, J. Olszewski, W. Ciurzynska, W. Lijun, B. Wyslocki, S. Szymura, M. Hasiak, *J. Magn. Mag. Mater.* 160 (1996) 281.
- [114] Y. Yoshizawa, S. Fujii, D. H. Ping, M. Ohnuma, K. Hono, *Acta Mater.* 48 (2003) 863.
- [115] N. Chau, N. Q. Hoa, N. D. The, P. Q. Niem, *J. Magn. Mag. Mater.* 304 (2006) e179.
- [116] K. Suzuki, A. Makino, A. Inoue, T. Masumoto, *J. Appl. Phys.* 70 (1991) 6232.
- [117] T. Sourmail, *Prog. Mater. Sci.* 50 (2005) 816.
- [118] M. A. Willard, M. Q. Huang, D. E. Laughlin, M. E. McHenry, J. O. Cross, V. G. Harris, C. Franchetti, *AIP* 85 (1999) 4421.
- [119] J. Zhang, H. Tan, Y. P. Feng, *Scripta Mater.* 53 (2005) 183.
- [120] A. Inoue, B. Shen, *Mater. Trans. JIM* 43 (2002) 766.
- [121] A. Hirata, Y. Hirotsu, K. Amiya, N. Nishiyama, A. Inoue, *Intermetallics* 16 (2008) 491.
- [122] M. Imafuku, S. Sato, H. Koshiba, E. Matsubara, A. Inoue, *Scripta Mater.* 44 (2001) 2369.
- [123] B. Shen, C. Chang, A. Inoue, *Intermetallics* 15 (2007) 9.

- [124] Y. Yoshizawa, E. Kakimoto, K. Doke, *Mater. Sci. Eng. A* 449-451 (2007) 480.
- [125] A. Inoue, B. Shen, *J. Mater. Res.* 18 (2003) 2799.
- [126] G. Herzer, H. R. Hilzinger, *J. Magn. Mag. Mater.* 62 (1986) 143.
- [127] A. Hirata, Y. Hirotsu, T. Ohkubo, N. Tanaka, T. G. Nieh, *Intermetallics* 14 (2006) 903.
- [128] X. J. Han, H. Teichler, *Phys. Rev. E* 75 (2007) 061501.
- [129] S. Furumi, S. Yokoyama, A. Otomo, S. Mashiko, *Appl. Phys. Lett.* 82 (2003) 16.
- [130] S. Hosokawa, J. F. Berar, N. Boudet, T. Ichitsubo, E. Matsubara, W. C. Pilgrim, N. Nishiyama, *J. Phys.: Conf. Ser.* 98 (2008) 012013.
- [131] N. Mattern, H. Hermann, S. Roth, J. Sakowski, M.-P. Macht, P. Jovari, J. Jiang, *Appl. Phys. Lett.* 82 (2003) 2589.
- [132] K. Yashiro, M. Nishimura, Y. Tomita, *Modelling Simul. Mater. Sci. Eng.* 14 (2006) 597.
- [133] Y. V. Barmin, I. L. Bataronov, A. V. Bondarev, V. V. Posmet'yev, *J. Phys.: Condens. Matter* 20 (2008) 114117.
- [134] X. Hui, R. Gao, G. L. Chen, S. L. Shang, Y. Wang, Z. K. Liu, *Phys. Lett. A* 372 (2008) 3078.
- [135] N. Mattern, A. Schöps, U. Kühn, J. Acker, O. Khvostikova, J. Eckert, *J. Non-cryst. Solids* 354 (2008) 1054.
- [136] T. C. Hufnagel, S. Brennan, *Phys. Rev. B* 67 (2003) 014203.

[137] L. Qi, L. F. Dong, S. L. Zhang, X. B. Chen, R. P. Liu, P. K. Liaw, *Phys. Lett. A* 372 (2008) 708.

[138] L. Qi, L. F. Dong, S. L. Zhang, M. Z. Ma, Q. Jing, G. Li, R. P. Liu, *Comput. Mater. Sci.* In Press, Corrected Proof (2008).

[139] H. Okamoto, *Phase Equilib. Diff.* 25 (2004) 297.

APPENDIX A

PHASE DIAGRAMS

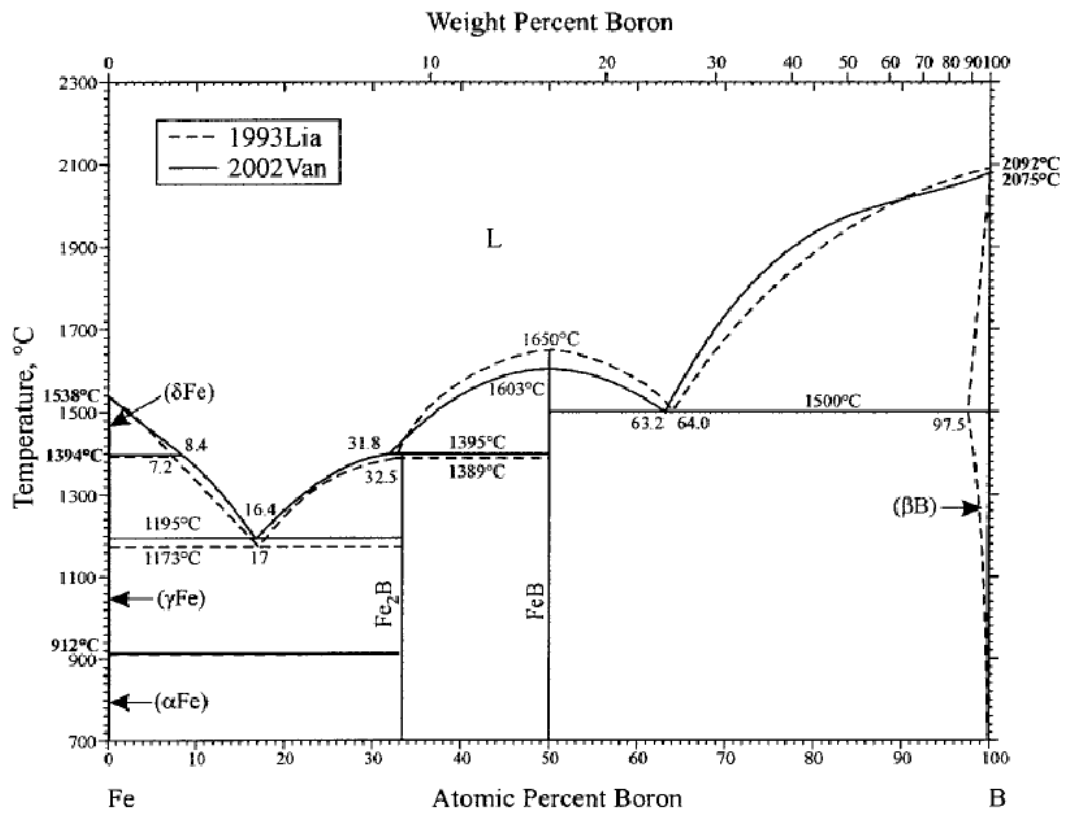


Figure A. 1 Fe-B Binary phase diagram [139].

APPENDIX B

C++ SOURCE CODES

```
#include <iostream>
#include <fstream>
#include <stdlib.h>
#define random(x) (rand() % (x))
#include <math.h>
#include <time.h>
#include <string.h>
#include <dir.h>
#include "MersenneTwister.h"
using namespace std;

////////////////////////////////PRIMARY PARAMETERS////////////////////////////////
int R=125; //ATOMIC RADIUS FOR INITIATION OF BCC (pm)
int X2=17; //AMOUNT OF THE ALLOYING ELEMENT (%)
double Tt=300.0; //INITIAL TEMPERATURE (Kelvin)
double T_FINAL=2000; //FINAL TEMPERATURE
int n=19; //# OF ATOMS ON AN EDGE OF THE SIMULATION CELL
int Thermal_TRY=40000; //# MC-STEPS AT INITIAL TEMPERATURE
int C_H_TRY=10000; //# MC-STEPS AT OTHER TEMPERATURES
int EQM=5000; //# OF MC-STEPS REMAINING TO CALCULATE AVERAGES
double T_DROP=100; //TEMPERATURE INCREMENT
int swt=0; //SET THIS TO 1 TO READ COORDINATES FROM FILE
////////////////////////////////////////////////////////////////

////////////////////////////////
////////THERE IS NO USER ADJUSTABLE PARAMETER AFTER THIS POINT////////
////////////////////////////////

////////////////////////////////GLOBAL VARIABLES////////////////////////////////
int N; int TRY; double SHIFT=0.0025; double SHIFTV; double L, Lbcc3, X2keep;
double T; double VAB[251], VAA[251], VBB[251]; double kb=315774.64;
int NL[12000][800];
////////////////////////////////

////////////////////////////////DISTANCE CALCULATOR////////////////////////////////
double DIST(double x1, double y1, double z1, double x2, double y2, double z2) {
double A; A=((x1-x2)*(x1-x2)+(y1-y2)*(y1-y2)+(z1-z2)*(z1-z2));
A=sqrt(A)*L; return A; }
////////////////////////////////
```

```

////////////////////////////////////READING THE POTENTIALS////////////////////////////////////
void VREAD() {
double ii;
int jj;
ifstream v1,v2,v3;
v1.open("VAB.txt");
for (jj=0;jj<251;jj++)
{ v1 >> ii; VAB[jj]=ii; } v1.close();
v2.open("VAA.txt");
for (jj=0;jj<251;jj++)
{ v2 >> ii; VAA[jj]=ii; } v2.close();
v3.open("VBB.txt");
for (jj=0;jj<251;jj++)
{ v3 >> ii; VBB[jj]=ii; } v3.close();
if
((int)(VAA[1]*100)!=(1*X2)||((int)(VAB[1]*100)!=(1*X2)||((int)(VBB[1]*100)!=(
1*X2))) {cout<<"***WARNING!! POTENTIALS ARE NOT CORRECT FOR THIS COMPOSITION
X2=" << X2 <<"%\n"; system("PAUSE");}
for (jj=0;jj<251;jj++){ VAA[jj]=VAA[jj]*kb; VAB[jj]=VAB[jj]*kb;
VBB[jj]=VBB[jj]*kb; }
VAA[1]=VAA[2]+(VAA[2]-VAA[3])*2; VAB[1]=VAB[2]+(VAB[2]-VAB[3])*2;
VBB[1]=VBB[2]+(VBB[2]-VBB[3])*2;
VAA[0]=VAA[1]+(VAA[2]-VAA[3])*10; VAB[0]=VAB[1]+(VAB[2]-VAB[3])*10;
VBB[0]=VBB[1]+(VBB[2]-VBB[3])*10;
//for (int ko=0;ko<=250;ko++) printf("%lf\n",VAA[ko]); system("PAUSE");
}
////////////////////////////////////

////////////////////////////////////NEIGHBOR LIST CONSTRUCTION////////////////////////////////////
int NLCONST(double arg[][4]) {
int rd15,at15,keeper,nl;
double xrd5,yrd5,zrd5;
float distance;
for (at15=0;at15<N;at15++){ keeper=0;
for (rd15=0;rd15<N;rd15++){ if (at15==rd15) continue;
xrd5=arg[rd15][0]; yrd5=arg[rd15][1];
zrd5=arg[rd15][2];
if ((xrd5-arg[at15][0])>0.5) xrd5=xrd5-1.0; if
((yrd5-arg[at15][1])>0.5) yrd5=yrd5-1.0; if ((zrd5-arg[at15][2])>0.5)
zrd5=zrd5-1.0;
if ((arg[at15][0]-xrd5)>0.5) xrd5=xrd5+1.0;
if ((arg[at15][1]-yrd5)>0.5) yrd5=yrd5+1.0; if ((arg[at15][2]-zrd5)>0.5)
zrd5=zrd5+1.0;
distance=DIST(arg[at15][0],arg[at15][1],arg[at15][2],xrd5,yrd5,zrd5);
if (distance<Rc) {NL[at15][keeper]=rd15;...
keeper++;}
} for (nl=0;nl<800;nl++) printf("%d\n",NL[345][nl]);
return 0;
}
////////////////////////////////////

```

```

//////////INTERNAL ENERGY CALCULATOR FOR ATOMIC SHIFT//////////
double LJ(double arg[][4], int RA){
    double energy,dist;
    double xlj,ylj,zlj;
    int ljl,tata,ups;
    energy=0;
    for (ups=0;ups<800;ups++){
        ljl=NL[RA][ups];
        if (ljl==RA) continue;
        xlj=arg[ljl][0];        ylj=arg[ljl][1];        zlj=arg[ljl][2];
        if ((xlj-arg[RA][0])>0.5) xlj=xlj-1.0;        if ((ylj-arg[RA][1])>0.5)
ylj=ylj-1.0;        if ((zlj-arg[RA][2])>0.5) zlj=zlj-1.0;
        if ((arg[RA][0]-xlj)>0.5) xlj=xlj+1.0;        if ((arg[RA][1]-ylj)>0.5)
ylj=ylj+1.0;        if ((arg[RA][2]-zlj)>0.5) zlj=zlj+1.0;
        dist=DIST(arg[RA][0],arg[RA][1],arg[RA][2],xlj,ylj,zlj)/5.291772;
        tata=(int)(ceil(dist));
        if (tata>200) continue; // extrapolation to 0
        if((arg[RA][3]==0)&&(arg[ljl][3]==0)) {
            energy=energy + VAA[tata]+ (VAA[tata]-VAA[tata-1])*(dist-
(double)(tata)); goto there;
        }
        if(((arg[RA][3]==0)&&(arg[ljl][3]==1))||((arg[RA][3]==1)&&(arg[ljl][3]==0))) {
            energy=energy + VAB[tata]+ (VAB[tata]-VAB[tata-1])*(dist-
(double)(tata)); goto there;
        }
        if((arg[RA][3]==1)&&(arg[ljl][3]==1)) {
            energy=energy + VBB[tata]+ (VBB[tata]-VBB[tata-1])*(dist-
(double)(tata));
        }
        there: if ((NL[RA][ups+1]==0)&&(NL[RA][ups+2]==0)) break;
    }
    return energy; /*the result is energy/kboltzman*/
}
//////////

//////////GLOBAL INTERNAL ENERGY CALCULATOR//////////
double LJ2(double arg[][4]){
    double dist,energy; double xlj,ylj,zlj; int ljj, ljj2,tata,ups; energy=0;
    for (ljj=0;ljj<N;ljj++) {
        for (ups=0;ups<800;ups++) {
            ljj2=NL[ljj][ups];
            xlj=arg[ljj2][0];        ylj=arg[ljj2][1];        zlj=arg[ljj2][2];
            if ((xlj-arg[ljj][0])>0.5) xlj=xlj-1.0;        if ((ylj-
arg[ljj][1])>0.5) ylj=ylj-1.0;        if ((zlj-arg[ljj][2])>0.5) zlj=zlj-1.0;
            if ((arg[ljj][0]-xlj)>0.5) xlj=xlj+1.0;        if ((arg[ljj][1]-
ylj)>0.5) ylj=ylj+1.0;        if ((arg[ljj][2]-zlj)>0.5) zlj=zlj+1.0;
            dist=DIST(arg[ljj][0],arg[ljj][1],arg[ljj][2],xlj,ylj,zlj)/5.291772;
            tata=(int)(ceil(dist));
            if (tata>200) continue; // extrapolation to 0
            if((arg[ljj][3]==0)&&(arg[ljj2][3]==0)) {
                energy=energy + VAA[tata]+ (VAA[tata]-VAA[tata-1])*(dist-
(double)(tata)); goto there;
            }
            if(((arg[ljj][3]==0)&&(arg[ljj2][3]==1))||((arg[ljj][3]==1)&&(arg[ljj2][3]==0))) {
                energy=energy + VAB[tata]+ (VAB[tata]-VAB[tata-1])*(dist-
(double)(tata)); goto there;
            }
            if((arg[ljj][3]==1)&&(arg[ljj2][3]==1)) {
                energy=energy + VBB[tata]+ (VBB[tata]-VBB[tata-1])*(dist-
(double)(tata));
            }
            there: if ((NL[ljj][ups+1]==0)&&(NL[ljj][ups+2]==0)) break;
        }
    } return energy/2.0;
}
//////////

```

```

//////////BOND ANGLE DISTRIBUTION CALCULATOR//////////
//////////THIS IS EMBEDDED IN RDF FUNCTION//////////
printf("\n***BOND ANGLE DISTRIBUTION CALCULATION FOR %d\n",type);
char name5[20]; sprintf(name5,"%dK BAD TYPE %d.txt",(int)temp,type);
ofstream badrec(name5);
int size1=(int)(ceil(CN))+10; int chaser1,at25,at35,bnd1; double
mesax5,angler,angler1;
double Nghbr[size1][2]; int ANGLE[201]; for (at15=0;at15<201;at15++)
ANGLE[at15]=0;
for (int kl=0;kl<500;kl++){
// READ COORDINATES FOR EACH kl
for (i1=0;i1<500;i1++){lavg >> 12; if (i1==kl){L=12; break;}}
char cordname[12]; sprintf(cordname,"%d.txt",kl);
ifstream corder;
corder.open(cordname); int atom12=0;
for (i1=0;i1<N;i1++){
corder>>arg[atom12][0]; corder>>arg[atom12][1];
corder>>arg[atom12][2]; corder>>arg[atom12][3];
atom12++; } corder.close();
for (at15=0;at15<N;at15++){
if (arg[at15][3]==aa1) continue; chaser1=0;
for (at25=0;at25<size1;at25++){ Nghbr[at25][0]=0; Nghbr[at25][1]=0;}
for (rd15=0;rd15<N;rd15++){
if (arg[rd15][3]==bb1) continue;
if (rd15==at15) continue;
xrd5=arg[rd15][0]; yrd5=arg[rd15][1];
zrd5=arg[rd15][2];
if ((xrd5-arg[at15][0])>0.5) xrd5=xrd5-1.0; if ((yrd5-
arg[at15][1])>0.5) yrd5=yrd5-1.0; if ((zrd5-arg[at15][2])>0.5)
zrd5=zrd5-1.0;
if ((arg[at15][0]-xrd5)>0.5) xrd5=xrd5+1.0; if
((arg[at15][1]-yrd5)>0.5) yrd5=yrd5+1.0; if ((arg[at15][2]-zrd5)>0.5)
zrd5=zrd5+1.0;
mesa5=DIST(arg[at15][0],arg[at15][1],arg[at15][2],xrd5,yrd5,zrd5);
if (mesa5<Cord_Up){
Nghbr[chaser1][0]=(double)rd15; Nghbr[chaser1][1]=mesa5; chaser1++;
}
}
for (at25=0; at25<=(chaser1-1);at25++){
for (at35=at25+1;at35<=(chaser1-1);at35++){
xrd5=arg[(int)Nghbr[at35][0]][0];
yrd5=arg[(int)Nghbr[at35][0]][1]; zrd5=arg[(int)Nghbr[at35][0]][2];
if ((xrd5-arg[(int)Nghbr[at25][0]][0])>0.5) xrd5=xrd5-1.0;
if ((yrd5-arg[(int)Nghbr[at25][0]][1])>0.5) yrd5=yrd5-1.0; if ((zrd5-
arg[(int)Nghbr[at25][0]][2])>0.5) zrd5=zrd5-1.0;
if ((arg[(int)Nghbr[at25][0]][0]-xrd5)>0.5) xrd5=xrd5+1.0;
if ((arg[(int)Nghbr[at25][0]][1]-yrd5)>0.5) yrd5=yrd5+1.0; if
((arg[(int)Nghbr[at25][0]][2]-zrd5)>0.5) zrd5=zrd5+1.0;
mesax5=DIST(arg[(int)Nghbr[at25][0]][0],arg[(int)Nghbr[at25][0]][1],arg[(int)Nghbr[at25][0]][2],xrd5,yrd5,zrd5);

angler=(Nghbr[at25][1]*Nghbr[at25][1]+Nghbr[at35][1]*Nghbr[at35][1]-
mesax5*mesax5)/2/Nghbr[at25][1]/Nghbr[at35][1];
bnd1=(int)(floor(angler*100.0)+100.0); //printf("bnd1=%d, cos=%.3f
dist=%.3f %.3f %.3f\n",bnd1,angler,mesax5,Nghbr[at25][1],Nghbr[at35][1]);
system("PAUSE");
ANGLE[bnd1]=ANGLE[bnd1]+1;
} }
} }

```

```

        angler1=0;
        for (at35=0;at35<201;at35++) { angler1=angler1+(double)ANGLE[at35];}
        for (at35=0;at35<201;at35++) {
            badrec << (double)ANGLE[at35]/angler1;
            badrec << "\n"; } badrec.close();}
// type 0 = AA, 1=BB, 2=TOTAL, 3=BA, 4=AB
alpha=(X2keep*(CNkeeper[0]-CNkeeper[3])+(1.0-X2keep)*(0.05-
CNkeeper[4]))/(X2keep*(0.05+CNkeeper[3])+(1.0-
X2keep)*(CNkeeper[0]+CNkeeper[4]));
Z1=CNkeeper[0]+CNkeeper[4];
Z2=0.05+CNkeeper[3];
if (Z1*(1.0-X2keep)>Z2*X2keep) {nmax=Z1*(1.0-X2keep); nmin=Z2*X2keep;} else
{nmin=Z1*(1.0-X2keep); nmax=Z2*X2keep;}
nu21=(CNkeeper[3]*((1.0-X2keep)*Z1+X2keep*Z2)/(1.0-X2keep)/Z1/Z2-1.0)*nmin/nmax;
coordn << "alpha="; coordn << alpha; coordn << "\n"; coordn << "nu21="; coordn
<< nu21;
coordn << "\n"; coordn.close(); lavg.close();
//Deleting Unused files
for (int dlter=0;dlter<500;dlter++){
char al23[12]; sprintf(al23,"%d.txt",dlter);
remove(al23); } return 0; }
////////////////////////////////////

////////////////////////////////////RADIAL DISTRIBUTION FUNCTION CALCULATOR////////////////////////////////////
int RDFC(double temp) {
// type 0 = AA, 1=BB, 2=TOTAL, 3=BA, 4=AB
int delta5,rd15,at15,ww35,hk15,mesa15;
double xrd5,yrd5,zrd5,alpha,nu21,Z1,Z2,nmin,nmax, arg[N][4];
int rdffvar5,aal,bb1,c1,c2,type,il; rdffvar5=(int)(L)+1;
double RDF5[rdffvar5],mesa5; double RDFSUM[rdffvar5]; double Lavg=0.0;
double l2; ifstream lavg;lavg.open("coorddataL.txt");
if (lavg.is_open()){
for (int l1=0;l1<500;l1++){ (lavg >> l2; Lavg=Lavg+l2/500.0);}
printf("Lavg=%f\n",Lavg);}
double CNkeeper[5];char CNTtype[20];
sprintf(CNTtype,"%dK COORDINATIONS.txt",(int)temp);
ofstream coordn (CNTtype) ;
for (type=0; type<=4; type++){ printf("***RDF CALCULATION %d\n",type);
if (type==0) { aal=1; bb1=1; c1=X2; c2=c1; }
if (type==1) { aal=0; bb1=0; c1=N-X2; c2=c1; }
if (type==2) { aal=5; bb1=5; c1=0; c2=c1; }
if (type==3) { aal=0; bb1=1; c1=N-X2; c2=X2; }
if (type==4) { aal=1; bb1=0; c1=X2; c2=N-X2; }
for(delta5=0; delta5<=(int)(L); delta5++){RDF5[delta5]=0; RDFSUM[delta5]=0; }
for (int kl=0;kl<500;kl++){ for (il=0;il<500;il++){ (lavg >> l2;
if(il==kl){L=l2; break;}}
for(delta5=0; delta5<rdffvar5; delta5++){RDF5[delta5]=0; }
for (il=0;il<500;il++){ (lavg >> l2; if(il==kl){L=l2; break;}}
char cordname[12]; sprintf(cordname,"%d.txt",kl);
ifstream corder;
corder.open(cordname); int atom12=0;
for (il=0;il<N;il++){
corder>>arg[atom12][0]; corder>>arg[atom12][1];
corder>>arg[atom12][2]; corder>>arg[atom12][3];
atom12++; } corder.close();
for (at15=0;at15<N;at15++) {
if (arg[at15][3]==aal) continue;
for (rd15=0;rd15<N;rd15++){
if (arg[rd15][3]==bb1) continue;
if (rd15==at15) continue;

```

```

        xrd5=arg[rd15][0];          yrd5=arg[rd15][1];          zrd5=arg[rd15][2];
        if ((xrd5-arg[at15][0])>0.5) xrd5=xrd5-1.0;
        if ((yrd5-arg[at15][1])>0.5) yrd5=yrd5-1.0;
        if ((zrd5-arg[at15][2])>0.5) zrd5=zrd5-1.0;
        if ((arg[at15][0]-xrd5)>0.5) xrd5=xrd5+1.0;
        if ((arg[at15][1]-yrd5)>0.5) yrd5=yrd5+1.0;
        if ((arg[at15][2]-zrd5)>0.5) zrd5=zrd5+1.0;
    mesa5=DIST(arg[at15][0],arg[at15][1],arg[at15][2],xrd5,yrd5,zrd5);
    mesa15=(int)(floor(mesa5)); RDF5[mesa15]=RDF5[mesa15]+1; } }
        for (ww35=1;ww35<=(int)(L/2);ww35++){
RDF5[ww35]=RDF5[ww35]/(N-c1)/(4.0*3.14159265*ww35*ww35)*pow((double)L,3.0)/(N-
c2);}
        for (ww35=1; ww35<=(int)(L/2);ww35++){
RDFSUM[ww35]=RDFSUM[ww35]+RDF5[ww35]/500.0;}
    }
char name2[20]; sprintf(name2,"%dK RDF TYPE %d.txt",(int)temp,type);
//RDF RECORDER
int kx795; ofstream rdf (name2);
if (rdf.is_open())
    { for(kx795=0; kx795<(int)(L/2); kx795++){ rdf << RDFSUM[kx795];
        rdf << "\n"; } rdf.close(); }
    else cout << "Unable to open file";
///////////////////////////////////////////////////////////////////

/////////////////////////////////////////////////////////////////COORDINATION NUMBER CALCULATOR/////////////////////////////////////////////////////////////////
/////////////////////////////////////////////////////////////////THIS CONTINUES FROM RDF FUNCTION/////////////////////////////////////////////////////////////////
printf("***CN CALCULATION %d\n",type);
int Cord_Low, Cord_Peak, Cord_Up;
double Tracer;
for (ww35=0;ww35<300;ww35++) {
if (RDFSUM[ww35]!=0) {
Cord_Low=ww35;
break; } }
printf("Lower Limit of Coordination Integration = %d pm\n",Cord_Low);
Tracer=0; for (ww35=Cord_Low;ww35<400;ww35++) {
if (RDFSUM[ww35]>Tracer) { Tracer=RDFSUM[ww35]; Cord_Peak=ww35; } }
printf("Peak of Coordination Integration = %d pm\n",Cord_Peak);
Cord_Up=Cord_Peak; Tracer=RDFSUM[Cord_Peak];
for (ww35=Cord_Peak+10;ww35<(Cord_Peak+(Cord_Peak-Cord_Low)+100);ww35++) {
if (RDFSUM[ww35]<Tracer) {
Tracer=RDFSUM[ww35]; Cord_Up=ww35; } }
char ask;
printf("Upper Limit of Coordination Integration = %d pm\n",Cord_Up);
printf("Do you want to modify upper limit manually? (Y/N)");
scanf ("%s",&ask);
if ((ask=='y')||(ask=='Y')) {
printf ("\nPlease enter the upper limit in pm: ");
scanf ("%d",&Cord_Up);
printf ("\nNew upper limit is %d pm",Cord_Up); }
double CN=0;
for (ww35=Cord_Low; ww35<=Cord_Up; ww35++) {
CN=CN+RDFSUM[ww35]*(4.0*3.14159265*ww35*ww35)*(N-c2)/pow((double)Lavg,3.0);}
coordn << type; coordn << " "; coordn << CN; coordn << "\n"; CNkeeper[type]=CN;
/////////////////////////////////////////////////////////////////

```

```

////////////////////////////////////COORDINATE RECORDER////////////////////////////////////
int COORD_REC RD (double arg[][4], char *name, int type){
    int kx78;
    ofstream myfile (name);
    if (myfile.is_open())
    {
        if (type==0)    myfile << (N-X2);
        if (type==1)    myfile << X2;
            myfile << "\n";
                myfile << "0";
                    myfile << "\n";
        for(kx78=0; kx78<N; kx78++){

            if (arg[kx78][3]==type){
                myfile << kx78;
                myfile << " ";
                myfile << arg[kx78][0]*L/100.0;
                myfile << " ";
                myfile << arg[kx78][1]*L/100.0;
                myfile << " ";
                myfile << arg[kx78][2]*L/100.0;
                myfile << "\n";
            }

        } myfile.close(); }
        else cout << "Unable to open file";
/*Koordinat kaydinin sonu*/
return 0;
}
////////////////////////////////////

```

```

//////////////////////////////////MAIN LOOP OF SIMULATION//////////////////////////////////
int main(int argc, char *argv[])
{

printf("***MONTE CARLO NPT ENSEMBLE SIMULATOR BY MURATAHAN AYKOL 2006\n");
VREAD();

int ztz;

time_t rawtime;

time (&rawtime);
char *tarih=ctime (&rawtime);
string tarih2;
tarih2=tarih2.insert(0,tarih);
tarih2.erase(13,1);
tarih2.insert(13,"-");
tarih2.erase(16,1);
tarih2.insert(16,"-");
tarih2.erase(24,1);
char tarih3[24];
strcpy(tarih3,tarih2.c_str());
mkdir (tarih3);
chdir (tarih3);

time_t seconds;
time(&seconds);
srand((unsigned int) seconds);

N=n*n*n+(n-1)*(n-1)*(n-1)-(3*n*n-3*n+1);
double AC[N][4];
ofstream Sinfo ("Info.txt");
Sinfo << "N="; Sinfo << N; Sinfo << "\n"; Sinfo << "%SECOND ELEMENT="; Sinfo <<
X2; Sinfo << "\n";
Sinfo << "Thermalization Temp="; Sinfo << Tt; Sinfo << "K\n"; Sinfo <<
"Thermalization Steps="; Sinfo<<Thermal_TRY; Sinfo << "\n";
Sinfo << "Final Temp="; Sinfo << T_FINAL; Sinfo << "K\n"; Sinfo <<
"Heating/Cooling Steps="; Sinfo<<C_H_TRY; Sinfo << "\n";
Sinfo << "Temp Drop="; Sinfo << T_DROP; Sinfo << "K\n";
Sinfo << "Rate="; Sinfo << T_DROP/C_H_TRY; Sinfo << " K/MCs";
Sinfo.close();

/*BCC ATOM POSITIONING*/
int atom_sc=0;
double nsc=(double) (n-1)/2.0;
double xsc, ysc, zsc;
for (xsc=-nsc; xsc<nsc; xsc++) {
for (ysc=-nsc; ysc<nsc; ysc++) {
for (zsc=-nsc; zsc<nsc; zsc++) {
AC[atom_sc][0]=xsc*0.5/nsc; //printf ("OK
xsc=%lf\n",AC[atom_sc][0]);
AC[atom_sc][1]=ysc*0.5/nsc;
AC[atom_sc][2]=zsc*0.5/nsc;
atom_sc++;
}
}
}

for (xsc=-(nsc-0.5);xsc<=(nsc-0.5); xsc++) {
for (ysc=-(nsc-0.5);ysc<=(nsc-0.5); ysc++) {
for (zsc=-(nsc-0.5);zsc<=(nsc-0.5); zsc++) {
AC[atom_sc][0]=xsc*0.5/nsc; //printf ("OK
xsc=%lf\n",AC[atom_sc][0]);
AC[atom_sc][1]=ysc*0.5/nsc;
AC[atom_sc][2]=zsc*0.5/nsc;
atom_sc++;
}
}
}
}

```

```

L=2.309401077*(n-1)*R;

printf("***BCC STRUCTURE WILL BE THERMALIZED AT %.2lfk\n***BOX LENGTH=%.2f,
N=%d\n",Tt,L,N);
for (atom_sc=0;atom_sc<N;atom_sc++) {
AC[atom_sc][3]=0;
}
X2keep=(double)X2/100.0;
X2=(int)N*X2/100;
printf ("***Second Element=%d\n",X2);
for (atom_sc=0;atom_sc<X2;atom_sc++)      {
  Repeatos:
  n=random(N);
  if (AC[n][3]==1) goto Repeatos;
  AC[n][3]=1;
}

  if (swt) {
    printf ("Please copy the previous coordinates in to the current
folder.\nWhat is L(pm)?");
    float Lpx;
    scanf ("%f",&Lpx);
    L=(double)Lpx;
    int crl,cra;
    double ii;
    ifstream coordsread;
    ripit:
    coordsread.open("COORD TYPE 0 300K.xyz");
    if (!coordsread.is_open()) {printf ("Unable to find
coordinates. Copy them to this folder!\n"); system("PAUSE"); goto ripit;}
    for (crl=0;crl<(N-X2)*4+2;crl++)
    {
      coordsread >> ii;
      if (crl<=1) continue;
      if (((crl-2)%4)==0) {cra=(int)ii; AC[cra][3]=0; continue;}
      AC[cra][(crl-2)%4-1]=ii*100/L;
    }
    coordsread.close(); ripit2:
    coordsread.open("COORD TYPE 1 300K.xyz"); if (!coordsread.is_open()) {printf
("Unable to find coordinates. Copy them to this folder!\n"); system("PAUSE");
goto ripit2;}
    for (crl=0;crl<X2*4+2;crl++)
    {
      coordsread >> ii;

      if (crl<=1) continue;
      if (((crl-2)%4)==0) {cra=(int)ii; AC[cra][3]=1; continue;}
      AC[cra][(crl-2)%4-1]=ii*100/L;
    }
    coordsread.close();
    printf("***STRUCTURE IS TERMINATED. PREVIOUS COORDINATES ARE LOADED
L=%.2lf\n",L);
    } system("PAUSE");
//BASE ELEMENT = 0, SECOND ELEMENT = 1
Lbcc3=L*L*L;
SHIFTV=L*L*L*0.0022;
ofstream myfile1 ("Fe.xyz");
ofstream myfile2 ("B.xyz");
COORD_RECRD(AC,"initial coordinates Fe.xyz",0); COORD_RECRD(AC,"initial
coordinates B.xyz",1);
ofstream volume ("volume recorder.txt");
/*ATOM SHIFT*/ int AS1,AS2,V1,LOOP;
double dx,dy,dz,ASR[3],ASE1,ASE2,boltz,ASRAND,DVOL,DL,KL,U1,U2,DU,L3;
double V,H,P,H2; int ACC=0; int ACC2=0; int st;
P=1.0*7.3389*pow(10.0,-9.0);

```



```

int kx78,type; type=0;
if (myfile1.is_open())
( if (type==0) myfile1 << (N-X2);
  if (type==1) myfile1 << X2;
    myfile1 << "\n"; myfile1 << "0"; myfile1 << "\n";
  for(kx78=0; kx78<N; kx78++){
    if (AC[kx78][3]==type){
      myfile1 << kx78; myfile1 << " ";
      myfile1 << AC[kx78][0]*L/100.0;
      myfile1 << " ";
      myfile1 << AC[kx78][1]*L/100.0;
      myfile1 << " ";
      myfile1 << AC[kx78][2]*L/100.0;
      myfile1 << "\n"; } } }
type=1;
if (myfile2.is_open())
( if (type==0) myfile2 << (N-X2);
  if (type==1) myfile2 << X2;
    myfile2 << "\n"; myfile2 << "0"; myfile2 << "\n";
  for(kx78=0; kx78<N; kx78++){
    if (AC[kx78][3]==type){
      myfile2 << kx78; myfile2 << " ";
      myfile2 << AC[kx78][0]*L/100.0;
      myfile2 << " ";
      myfile2 << AC[kx78][1]*L/100.0;
      myfile2 << " ";
      myfile2 << AC[kx78][2]*L/100.0;
      myfile2 << "\n"; } } }
if ((LOOP>(TRY-EQM))&&(LOOP+10)%10==0) {
  char namee22[20]; sprintf(namee22, "%d.txt", st);
  ofstream coorddata(namee22);
  coorddataL << L; coorddataL << "\n";
  for (atom_sc=0; atom_sc<N; atom_sc++) { ;
    coorddata << AC[atom_sc][0]; coorddata << " ";
    coorddata << AC[atom_sc][1]; coorddata << " ";
    coorddata << AC[atom_sc][2]; coorddata << " ";
    coorddata << AC[atom_sc][3]; coorddata << "\n";
    H2=H2+(U1+P*L3)/N*8.314472/1000.0/500.0;
    coorddata.close();
    st++; } }
  coorddataL.close();
  V_CH.close(); RDFC(T);

char Tname[24]; sprintf(Tname, "COORD TYPE 0 %dK.xyz", (int)T);
COORD_RECRC(AC, Tname, 0);
sprintf(Tname, "COORD TYPE 1 %dK.xyz", (int)T); COORD_RECRC(AC, Tname, 1);
/*VOLUME RECORDER*/
int VLim=500; double V_CH_KEEP=0.0;
double vv2, VOLARR[VLim]; double sdev=0.0; int kx787,vv1;
if (volume.is_open()) {
  volume << T; volume << " "; vv1=0; ifstream V_CH1;
  V_CH1.open(volname);
  for (kx787=0;kx787<TRY;kx787++)
  {V_CH1 >> vv2; if(kx787>=(TRY-VLim)) {VOLARR[vv1]=vv2; vv1++;} }
  V_CH1.close();
  for(kx787=0; kx787<VLim; kx787++){
  V_CH_KEEP=V_CH_KEEP+VOLARR[kx787]/(double)VLim;
  for(kx787=0; kx787<VLim; kx787++){
  sdev=sdev+(VOLARR[kx787]-V_CH_KEEP)*(VOLARR[kx787]-V_CH_KEEP)/(double)VLim;
  sdev=pow(sdev,0.5);
  volume << V_CH_KEEP; volume << " "; volume<<sdev; volume << "
"; volume<< H2; volume << "\n"; } else cout << "Unable to open file";
T=T+T_DROP; }
  myfile1.close(); myfile2.close(); volume.close();
  system("PAUSE"); return 0; }
////////////////////////////////////MAIN LOOP ENDS////////////////////////////////////

```

```

//////////BOND LENGTH ANGLE HYPERSURFACE CALCULATOR//////////
#include <cstdlib>
#include <iostream>
#include <fstream>
#include <math.h>
double Lover2=50.4533; int NFe=9682; int NB=1982;
double distance (double x1, double y1, double z1, double x2, double y2, double
z2) { double A,A1,A2,A3;
        if (fabs(x1-x2)>Lover2/2) A1=fabs(x1-x2)-Lover2; else A1=x1-x2;
        if (fabs(y1-y2)>Lover2/2) A2=fabs(y1-y2)-Lover2; else A2=y1-y2;
        if (fabs(z1-z2)>Lover2/2) A3=fabs(z1-z2)-Lover2; else A3=z1-z2;
        A= A1*A1+A2*A2+A3*A3;
        return sqrt(A);}
int main(int argc, char *argv[])
{ double distancer,mindist,maxsize;
  ifstream Data1,Data2; Data1.open("coordFe"); Data2.open("coordB");
  double Fe[NFe][3]; double B[NB][3]; int jj,kk; double
ii,iix,iyy,iiz;
  for (jj=0; jj<NFe; jj++){
    Data1 >> ii; Data1 >> iix ; Fe[jj][0]=iix; Data1 >> iyy ; Fe[jj][1]=iyy;
    Data1 >> iiz ; Fe[jj][2]=iiz; }
  for (jj=0; jj<NB; jj++){
    Data2 >> ii; Data2 >> iix ; B[jj][0]=iix; Data2 >> iyy ; B[jj][1]=iyy;
    Data2 >> iiz ; B[jj][2]=iiz;
  } Data1.close(); Data2.close();
double cosine,a,b,c; int cintt;
int Feremind[NB][15]; for (kk=0; kk<NB; kk++) { for (jj=0; jj<15; jj++)
Feremind[kk][jj]=-1; }
for (kk=0; kk<NB; kk++) { //FINDING NEIGHBORING Fe ATOMS
  cintt=0;
  for (jj=0;jj<NFe;jj++) { if (cintt==15) break;
    if
(distance (B[kk][0],B[kk][1],B[kk][2],Fe[jj][0],Fe[jj][1],Fe[jj][2])<2.69) {
      Feremind[kk][cintt]=jj; cintt++; } } }
int yy,zz,flexer1,flexer2; int DIST[370][200]; printf("AT\n");
for (kk=0; kk<370; kk++) { for (jj=0; jj<200; jj++) DIST[kk][jj]=0; }
for (kk=0; kk<NB; kk++) { printf("%d\n",kk);
for (jj=0; jj<15; jj++) { for (yy=0; yy<15; yy++) { for (zz=0; zz<15; zz++)
if ((Feremind[kk][jj]==-1)|| (Feremind[kk][zz]==-1)|| (Feremind[kk][yy]==-1))
continue;
a=distance (Fe[Feremind[kk][yy]][0],Fe[Feremind[kk][yy]][1],Fe[Feremind[kk][yy]][
2],Fe[Feremind[kk][jj]][0],Fe[Feremind[kk][jj]][1],Fe[Feremind[kk][jj]][2]);
b=distance (Fe[Feremind[kk][jj]][0],Fe[Feremind[kk][jj]][1],Fe[Feremind[kk][jj]][
2],Fe[Feremind[kk][zz]][0],Fe[Feremind[kk][zz]][1],Fe[Feremind[kk][zz]][2]);
c=distance (Fe[Feremind[kk][yy]][0],Fe[Feremind[kk][yy]][1],Fe[Feremind[kk][yy]][
2],Fe[Feremind[kk][zz]][0],Fe[Feremind[kk][zz]][1],Fe[Feremind[kk][zz]][2]);
cosine=(a*a+b*b-c*c)/2.0/a/b; cosine=cosine*100+100;
if (a<1.8) continue; if ((a>3.5)|| (b>3.5)) continue;
flexer1=(int) ((a-1.8)*100); flexer2=(int) cosine;
DIST[flexer1][flexer2]++; //if (DIST[flexer1][flexer2]>1000) {printf("DIST = %d
a= %f b=%f c=%f\n",DIST[flexer1][flexer2],a,b,c); system("PAUSE");}
} } } }
ofstream angler ("AngleSpace.txt"); int pseudo1,pseudo2; int avrg,avr,pdist;
for (kk=0;kk<370;kk++) {pseudo1=kk; avrg=0;
for (jj=0;jj<200;jj++){avrg=avrg+DIST[kk][jj];} if (avrg==0)avr=1;else avr=avrg;
for (jj=0;jj<200;jj++){pseudo2=jj; pdist=DIST[kk][jj];
angler << (double)pseudo1/100.0+1.8 << " " << (double) (pseudo2-100)/100.0
<< " " << ((double)pdist)/(double)avr << endl; } }
angler.close(); return EXIT_SUCCESS;}

```

```

//////////////////////////////////CLUSTER SIZE DISTRIBUTION CALCULATOR//////////////////////////////////

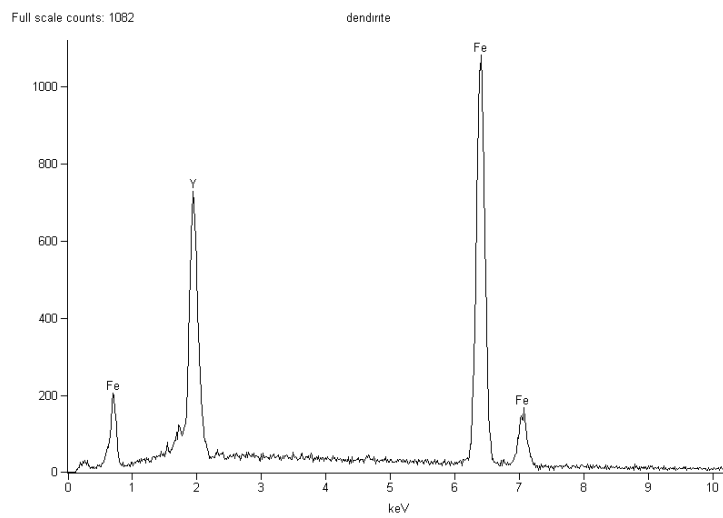
int NFe=9332; int NB=2332; double Lover2=50.4862;
int main(int argc, char *argv[])
{
    double distancer,mindist,maxsize;
    ifstream Data1,Data2;    Data1.open("coordFe");    Data2.open("coordB");
    double Fe[NFe][3]; double B[NB][3]; int jj,kk; int Cluster[NFe][25];
    double ClusterSizeD[NFe]; int ClusterSizeN[NFe]; int CkeeperCluster[NFe];
    double Freq[40];    int Freq2[40];
    for (jj=1; jj < 40; jj++){Freq [jj]=Freq [jj-1]+0.1;    Freq2 [jj]=0;}
    for (jj=0; jj < NFe; jj++){for (kk=0; kk<25; kk++) Cluster[jj][kk]=10000;}
    double ii,iix,iyy,iiz,runner,runnerkeeper; int Nkeeper; int Nmax=0;
    for (jj=0; jj<NFe; jj++){
        Data1 >> ii;    Data1 >> iix ; Fe[jj][0]=iix;    Data1 >> iyy ;
        Fe[jj][1]=iyy;    Data1 >> iiz ; Fe[jj][2]=iiz;    }
    for (jj=0; jj<NB; jj++){
        Data2 >> ii;    Data2 >> iix ; B[jj][0]=iix;    Data2 >> iyy ;
        B[jj][1]=iyy;    Data2 >> iiz ; B[jj][2]=iiz;    }
    Data1.close();    Data2.close();
    mindist=0; int counter=0; maxsize=0; int pp, runkeepLAST,hh,largest;
    for (jj=0; jj<NFe; jj++) {distancer=50000000.0; for (kk=0; kk<NB;kk++) {
        if (distance(Fe[jj][0],Fe[jj][1],Fe[jj][2],B[kk][0],B[kk][1],B[kk][2])<distancer)
            distancer=distance(Fe[jj][0],Fe[jj][1],Fe[jj][2],B[kk][0],B[kk][1],B[kk][2]);}
        if (distancer>4.155) {largest=jj; printf("%f\n",distancer);}
        Nkeeper=0; int counteratom=0;    for (kk=0; kk<NFe; kk++) {if
            distance(Fe[jj][0],Fe[jj][1],Fe[jj][2],Fe[kk][0],Fe[kk][1],Fe[kk][2])<distancer)
            {Cluster[jj][counteratom]=kk; Nkeeper++; counteratom++;}
            ClusterSizeD[jj]=distancer; ClusterSizeN[jj]=counteratom;}
        for (jj=0; jj<NFe; jj++) {    int Ckeeper=jj;
            for (kk=0; kk<NFe; kk++) {    for (hh=0; hh<25; hh++) {
                if (Cluster[kk][hh]==jj) if (ClusterSizeD[kk]>ClusterSizeD[Ckeeper])Ckeeper=kk;
                }    }    CkeeperCluster[jj]=Ckeeper;    }
            for (jj=0; jj<NFe; jj++){ if (CkeeperCluster[jj]==jj) {runnerkeeper=50000000;
                distancer=ClusterSizeD[jj];
                for (pp=0; pp<40; pp++) {
                    if ((Freq[pp]-distancer)*(Freq[pp]-distancer)<runnerkeeper)
            {runnerkeeper=(Freq[pp]-distancer)*(Freq[pp]-distancer); runkeepLAST=pp;}
                }    }    Freq2[runkeepLAST]++;    }    }

            ofstream CoordLarge ("CoordLarge.txt");
            for (pp=0; pp<25; pp++) {
                if (Cluster[largest][pp]==10000) continue;
                if (Fe[Cluster[largest][pp]][0]<0)Fe[Cluster[largest][pp]][0]
                =Fe[Cluster[largest][pp]][0] +Lover2;
                if (Fe[Cluster[largest][pp]][1]<0)Fe[Cluster[largest][pp]][1]
                =Fe[Cluster[largest][pp]][1] +Lover2;
                if (Fe[Cluster[largest][pp]][2]<0)Fe[Cluster[largest][pp]][2]
                =Fe[Cluster[largest][pp]][2] +Lover2;
                CoordLarge << pp << "    " << Fe[Cluster[largest][pp]][0] << "    "
                << Fe[Cluster[largest][pp]][1] << "    " << Fe[Cluster[largest][pp]][2] <<
                endl;    }    printf("%f\n %f\n %d", mindist/counter, maxsize,Nmax);
            return EXIT_SUCCESS;}
    ////////////////////////////////////
}

```

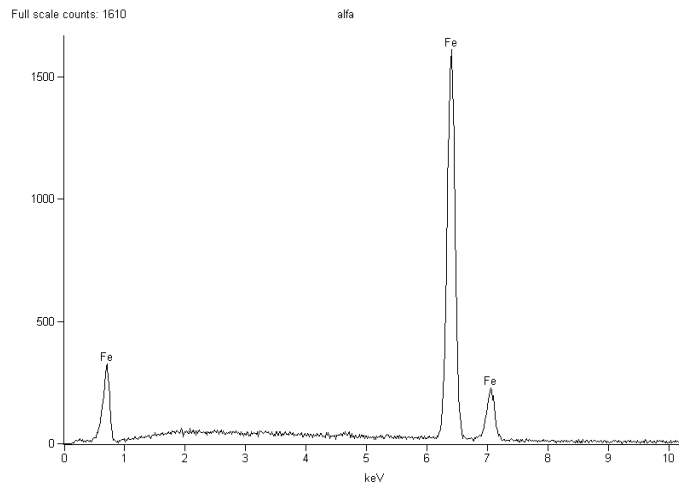
APPENDIX C

EDS ANALYSES



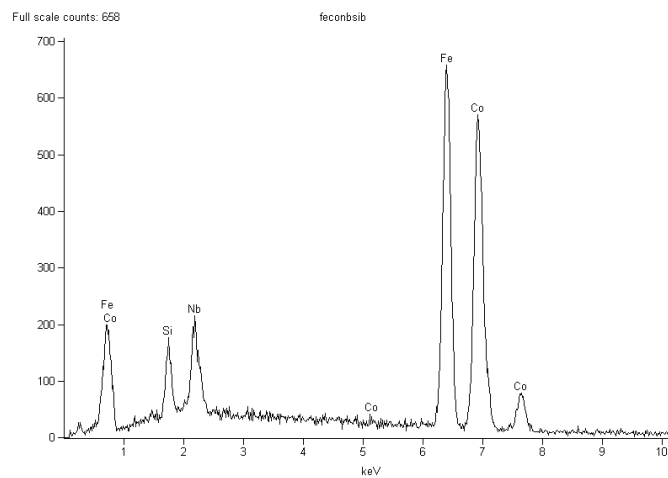
Element	Weight Conc. %	Atom Conc. %
Fe	63.88	73.79
Y	36.12	26.21

Figure C. 1 Composition of dendritic phase in centrifugal cast Fe-Y-B alloy by EDS analysis.



Element	Weight Conc. %	Atom Conc. %
Fe	100.00	100.00

Figure C. 2 Composition of inter-dendritic phase in centrifugal cast Fe-Y-B alloy by EDS analysis.



Element	Weight Conc. %	Atom Conc. %
Si	3.23	6.63
Fe	42.95	44.33
Co	43.72	42.77
Nb	10.10	6.27

Figure C. 3 Composition of amorphous phase in centrifugal cast Fe-Co-Nb-B-Si alloy by EDS analysis.